



VRIJE
UNIVERSITEIT
BRUSSEL



Dissertation for the Degree Master in Physics and Astronomy

MODELING OF NEUTRINO PRODUCTION IN STARBURST-DRIVEN (ULTRA)-LUMINOUS INFRARED GALAXIES

From Great Observatory All-Sky LIRG
Survey objects to IceCube neutrinos

Yarno Merckx

June 4, 2021

Promotor: Prof. Dr. Krijn de Vries
Supervisor: Pablo Correa

Sciences & Bio-Engineering Sciences

Covid-19

This master's thesis came about (in part) during the period in which higher education was subjected to a lockdown and protective measures to prevent the spread of the COVID-19 virus. The process of formatting, data collection, the research method and/or other scientific work the thesis involved could therefore not always be carried out in the usual manner. The reader should bear this context in mind when reading this Master's thesis, and also in the event that some conclusions are taken on board.

Abstract

The discovery of high-energy cosmic neutrinos by the IceCube collaboration in 2013 started the quest to unravel their origin. Multimessenger observations of both neutrinos and gamma rays show that the contribution of gamma-ray bright objects to the observed diffuse astrophysical neutrino flux is largely constrained. This initiated the interest in gamma-ray dim objects obscured by large amounts of dust and gas as candidate sources of astrophysical neutrinos. In this thesis the focus lies on objects within the Great Observatories All-Sky LIRG Survey (GOALS). GOALS objects are among the brightest infrared sources in the Universe, containing a tremendous energy budget combined with extreme amounts of obscuring matter. These two key features make GOALS objects excellent gamma-ray dim neutrino source candidates that can contribute to the diffuse neutrino flux measured by IceCube. A neutrino-production framework for starburst-driven GOALS objects is constructed within this work, with special focus on the electromagnetic observables that can be linked to neutrino production. This open-source framework is generic, such that it can be applied to all GOALS sources given the required electromagnetic observables. In this work, we apply our framework to the GOALS LIRG Arp 299 in order to obtain the first ever prediction of a starburst-driven neutrino flux from this source.

Acknowledgements

First I want to express my gratitude to my promotor Krijn for his countless valuable insights and guidance throughout this work. Ever since our first meeting three years ago Krijn has helped me on numerous occasions, always with great enthusiasm, for which I am truly grateful. Furthermore I also want to thank Nick for his sharp questions and critical attitude during our weekly meeting. Next, a few words of appreciation for the loveliest of supervisors. Pablo, apart from being a great supervisor, you have been an equally great friend. From the moment we met I have looked up to you and I still do. You have helped me to become the scientist that I am today, for which I want to say *grazie mille!*

I also want to thank Dr. George Privon from the GOALS collaboration for his valuable input during our collaborative efforts throughout the year. His expertise on the astrophysical objects and their electromagnetic observables were pivotal for the research done within this thesis.

Last but not least, I want to address my classmates (= friends for life). Aäron, thank you for the numerous times you have guided me through the depths of hell (maths) and for the great talks we had on life in general. Floriano, thank you for dealing with my mood swings ~ 8 hours/day for 5 years long and for your never ending support over the years, *Je t'aime poto!* Max, you have taught me to appreciate the small things in life, such as the possibility that dark matter will be solved during our lifetime. Mitja, without your motivational quotes before every exam, we would have never made it! Emilie, we have been classmates for an amazing eleven years, but now it is time to leave me alone. Nordin, I hate to be cheesy, but thank you for the late night-talks and the lovely mac and cheese you cooked for us back in the day.

Contents

1	Introduction	4
2	Observations of high-energy astrophysical neutrinos	8
2.1	Terrestrial and extraterrestrial neutrinos	8
2.2	The IceCube detector	11
2.3	Observations of the astrophysical neutrino flux	14
2.4	Searches for point-like sources of neutrinos	15
2.5	Compelling evidence for the first cosmic neutrino source: TXS 0506+056	16
3	Great Observatories All-sky LIRG Survey objects as gamma-ray dim neutrino sources	18
3.1	Starburst galaxies	18
3.2	U/LIRGs as promising gamma-ray obscured neutrino sources	21
3.3	Great Observatories All-Sky LIRG Survey (GOALS)	22
3.3.1	Multiwavelength observations	22
3.3.2	ISM density: line emission from tracers and black-body emission	23
3.3.3	U/LIRG morphology	24
3.3.4	GOALS ULIRG Arp 220	26
3.3.5	GOALS LIRG Arp 299	26
3.4	Starburst-driven neutrino-production framework	27
4	The proton injection rate	30
4.1	Endpoints in stellar evolution	30
4.1.1	Thermonuclear supernovae	30
4.1.2	Core-collapse supernovae	31
4.2	Shock formation	32
4.2.1	Basic shock theory	32
4.3	Shock structure and evolution of supernova remnants	35
4.4	First order Fermi acceleration	37
4.5	The proton injection rate Q_p	40
4.5.1	Fixing the normalisation constant	42
4.5.2	The supernova rate in U/LIRGs	43
4.5.3	Maximum attainable momentum	43
4.5.4	Power-law index	44
4.6	Proton injection rate computations	44

CONTENTS

5	Proton momentum distribution function	47
5.1	Proton injection rate vs momentum distribution function	47
5.2	Typical timescales of transport-shaping processes	49
5.2.1	Inelastic pp-interactions	49
5.2.2	Advection: Galactic superwind	50
5.2.3	Diffusion	51
5.3	Calorimetric requirement and timescale comparison	52
5.3.1	Timescales in non-U/LIRG starburst nuclei	53
5.3.2	Timescales in U/LIRG starburst nuclei	54
5.3.3	Equilibrium wind in starburst nuclei	55
5.4	Computations of the proton momentum distribution function	58
6	Neutrino flux from starburst-driven U/LIRGs	60
6.1	Neutrino-production rate	60
6.1.1	Neutrino-production rate computations	62
6.2	Neutrino flux	64
6.3	The power-law index	65
6.4	Neutrino-flux computations	65
6.4.1	Maximum attainable momentum	68
6.4.2	Varying galactic superwind speed, supernova rate, and ISM density	69
6.5	Neutrino-flux computations of Arp 299	71
7	Conclusion and outlook	76
A	Average energy gain in first order Fermi acceleration	81
B	Supernova rate in U/LIRGs: the initial mass function approach	83

Chapter 1

Introduction

The origin of Ultra-High-Energy Cosmic Rays (UHECRs), i.e. protons and other atomic nuclei with energies exceeding 10^{18} eV, is a long-standing unsolved mystery of physics. UHECRs are detected indirectly by large-scale Earth-based observatories, such as the Pierre Auger Observatory [1] and the Telescope Array (TA) [2]. These experiments observe the Extensive Air Showers (EAS) initiated by the interaction between an UHECR and an atmospheric nucleus. Nevertheless, the reconstructed arrival direction of cosmic rays (CRs) will most likely not point back to the original CR source, since CRs are deflected by (inter)galactic magnetic fields. CRs are also expected to interact with ambient matter and radiation at their source. Such an interaction produces neutral and charged pions which subsequently decay to high-energy photons (gamma rays) and neutrinos, respectively. Such hadronic gamma rays and neutrinos are therefore intimately connected. This is shown in Figure 1.1, where also the propagation and detection of these three high-energy messengers (CRs, gamma rays, and neutrinos) is illustrated.

Hadronic gamma rays can be traced back to their source to identify (U)HECR sources as they are not deflected by magnetic fields. However, the Universe is not transparent for high-energy photons since these can interact with dust or background radiation fields such as the Cosmic Microwave Background (CMB) and the Extragalactic Background Light (EBL). Furthermore, gamma rays are also produced in leptonic processes and as such do not provide a unique tracer of cosmic-ray sources. The GeV gamma-ray emission from numerous astrophysical sites in the Universe is observed by the space-based Fermi Large Area Telescope (Fermi-LAT). At energies exceeding 1 TeV, gamma rays are detected indirectly by ground-based observatories, such as the Major Atmospheric Gamma Imaging Cherenkov Telescope (MAGIC) and the High Energy Stereoscopic System (HESS) [3, 4]. Such very-high-energy gamma rays are observed through the electromagnetic (EM) showers they induce in the atmosphere.

Neutrinos are stable, chargeless, and only interact via the weak force which means they can reach Earth practically unattenuated. This makes them the ideal messengers to identify and study the sources of (U)HECRs. However, large detector volumes are required to observe a significant amount of these very weakly interacting particles. An example of such a large-scale neutrino detector is the IceCube Neutrino Observatory at the South Pole (Section 2.2) which is capable of observing neutrinos in the 10 TeV to 10 PeV energy range where a signal of astrophysical neutrinos is discernable from atmospheric background. High-energy cosmic neutrinos were first discovered by the IceCube Collaboration in 2013 above this background [6]. To date, the diffuse astrophysical neutrino flux has been observed via various independent IceCube analyses (Section 2.3).

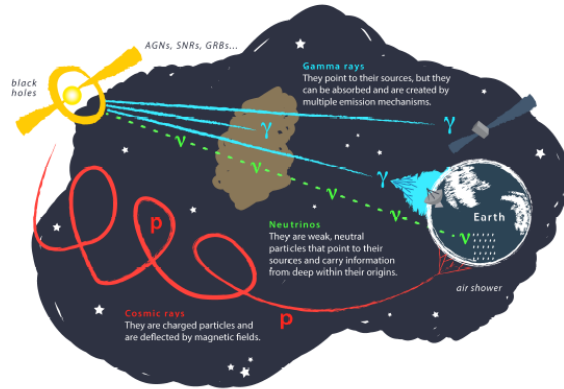


Figure 1.1: Visualization of the propagation of various messengers originating from the same hadronic source. In contrast to CRs, which are deflected by magnetic fields, gamma rays and neutrinos travel in a straight trajectory towards Earth. In addition, gamma rays can interact with matter or radiation on their path to Earth, while neutrinos will reach Earth unattenuated [5].

In multimessenger astronomy experimental data of different cosmic messengers, such as those mentioned above, is combined to search for common sources of these messengers. Figure 1.2 shows the diffuse spectra of gamma rays (detected by Fermi-LAT), high-energy neutrinos (detected by IceCube), and UHECRs (detected by the Telescope Array and the Pierre Auger Observatory). The energy densities of the messengers are comparable and therefore suggest a connection between the particles, such as a common origin.

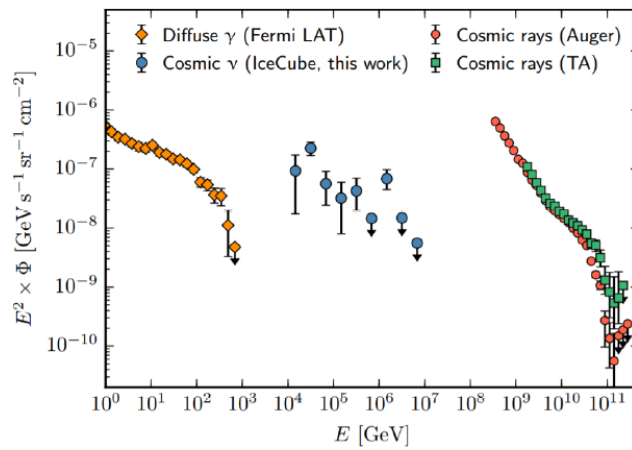


Figure 1.2: Diffuse emission detected by Fermi-LAT (gamma rays), IceCube (neutrinos), and Pierre Auger and TA (UHECRs) [7].

The multimessenger approach resulted in compelling evidence for the Fermi blazar TXS 0506+056, an active galactic nucleus (AGN) with its jet pointing towards Earth, as the first source of high-

energy astrophysical neutrinos, and as such a possible UHECR source (more details in Section 2.5). Nevertheless, Fermi blazars cannot be the sole sources of the diffuse astrophysical neutrino flux as earlier IceCube analyses of these sources largely constrained their contribution [8]. At the time of writing the origin of the IceCube astrophysical neutrino flux remains unknown.

Although the origin of astrophysical neutrinos remains undisclosed, observations are pointing towards heavily obscured gamma-ray sources. Recently an analysis was performed which investigated the relation between the diffuse gamma-ray flux observed by Fermi-LAT and the diffuse high-energy neutrino flux seen by IceCube [9]. To perform this analysis, the blazar contribution to the diffuse gamma-ray flux must be subtracted as their contribution to the observed neutrino flux is limited [8]. This is shown in Figure 1.3 where the black datapoints represent the diffuse neutrino flux (IceCube) while the red datapoints indicate the observed diffuse gamma-ray flux (Fermi-LAT).

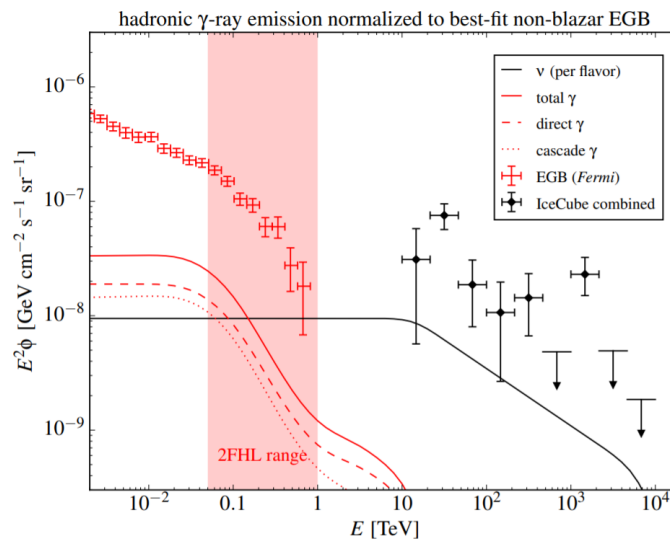


Figure 1.3: Diffuse gamma-ray flux (red data points) and neutrino flux (black data points), observed by Fermi-LAT and IceCube, respectively. The predicted neutrino flux (solid black line) based on the non blazar gamma-ray flux (solid red line) is found to be below the observed IceCube neutrino flux [8].

The full red line indicates the non-blazar gamma-ray flux. This consists of contributions from gamma rays reaching Earth directly (dashed line) and gamma rays produced in interactions of their more energetic counterparts with the CMB and EBL (dotted line). Finally, the black solid line shows the expected neutrino flux based on the non-blazar gamma-ray flux. This computation is done within the picture where accelerated CRs interact within their source and thereby produce charged and neutral pions which subsequently decay to neutrinos and gamma rays, respectively. The well-known pion decay channels allow to theoretically predict a neutrino flux given a gamma-ray flux, although this is far from trivial. From Figure 1.3 it can be seen that the predicted neutrino flux is well below the observed flux of neutrinos. This suggests that not all gamma rays, co-produced with astrophysical neutrinos in cosmic accelerators, reach our detectors. The tension between the diffuse gamma-ray and neutrino observations can be resolved if neutrinos originate from obscured sources containing large amounts of dust and gas. Such gamma-ray dim sources, also known as hidden sources, attenuate gamma rays while leaving neutrinos unaltered.

Several studies have been performed on such obscured neutrino sources. The first of these was an IceCube analysis on dust-obscured active galactic nuclei (AGN), i.e. supermassive black holes actively accreting matter, with flat radio spectra [10, 11]. This received a follow-up by phenomenological work, in which a model for neutrino production in obscured AGN was developed [12]. In this model, gamma rays can be attenuated by the dense clouds of matter surrounding the AGN. Ultra-luminous infrared galaxies (ULIRGs), which are among the most luminous infrared emitters in the Universe with infrared luminosities $L_{IR} > 10^{12}L_{\odot}$, where L_{\odot} is the solar luminosity, likely contain such heavily obscured AGN. It was shown that the population of ULIRGs integrated over cosmic history can fit the diffuse neutrino observations without violating the bounds on the non-blazar diffuse gamma-ray flux. Note that this requires column densities of the order of $10^{25-26} \text{ cm}^{-2}$ for the obscuring material, which are at the upper extreme of what is expected for such objects. However, the authors of this model also suggest that ULIRGs are unlikely to harbor sufficiently energetic AGN that can explain the diffuse neutrino flux. A possible solution to this is that the less luminous but much more numerous luminous infrared galaxies (LIRGs), i.e. galaxies with $L_{IR} > 10^{11}L_{\odot}$, also contribute to the diffuse neutrino observations.

In this work, the focus will lie on studying and modeling neutrino production related to star formation in both LIRGs and ULIRGs. It is noted that this is in contrast to the model mentioned above which focused on AGN related neutrino production in obscured sources. A computational code based on analytic expressions will be developed which will allow to predict the neutrino flux related to extreme star formation in U/LIRGs. This research is done in close collaboration with the Great Observatories All-Sky LIRG Survey (GOALS), providing extensive electromagnetic data for ~ 200 nearby U/LIRGs. Although the production of high-energy particles in starburst regions has been discussed extensively in the literature, this work explores the neutrino production in U/LIRGs modeled through GOALS observables, which is unprecedented.

Overview In Chapter 2 an overview of the different neutrino classifications is given which will allow to characterize the astrophysical neutrinos observed by the IceCube detector and as such also the neutrinos of interest for the framework developed in this work. In addition, the working of the IceCube detector and the current observational status of neutrino astronomy is discussed.

In Chapter 3, U/LIRGs, which are galaxies with an infrared luminosity larger than $10^{11}L_{\odot}$, are identified as candidate high-energy neutrino sources. Specifically the focus lies on U/LIRGs within the Great Observatories All-Sky LIRG Survey (GOALS) sample, which provides electromagnetic data for ~ 200 of the most nearby U/LIRGs. The necessity of the electromagnetic expertise by the GOALS Collaboration to accurately model neutrino production within U/LIRGs is argued. Chapter 3 is finished with an overview of the neutrino-production framework developed in Chapters 4 to 6.

In Chapter 4 and Chapter 5 analytic expressions are derived for the proton injection rate and the corresponding proton momentum distribution function in compact star-forming regions. These are crucial parameters to compute the neutrino production rate in U/LIRGs. Finally the analytic expressions will be translated to a numerical code which we will test through comparison with other model predictions. In Chapter 6 the foundation laid in Chapter 4 and Chapter 5 is combined into a code which will allow to predict the neutrino flux for any compact star-forming region in the GOALS sample, which is the main achievement of this work. This code is available on GitHub and will be maintained during future work [13]. Finally, we use our framework in a case study of the GOALS LIRG Arp 299, where we will make the first prediction of a neutrino flux from this object. A scheme summarizing the relations between the parameters of the developed framework can be consulted in Figure 7.1.

Chapter 2

Observations of high-energy astrophysical neutrinos

Neutrinos originate from a variety of (extra)terrestrial sources and span over a wide range of energies and fluxes. In Section 2.1, an overview is given of these different neutrino classifications. After that, we focus on the high-energy astrophysical neutrino flux measured with IceCube. The IceCube detector is discussed in Section 2.2, and the IceCube neutrino observations are presented in Section 2.3. In Section 2.4 sensitivities for point-like sources, based on 10 years of IceCube data, are presented and will allow to interpret the computed neutrino fluxes in the last chapter of this work. Finally, the first compelling evidence for a source of high-energy astrophysical neutrinos is discussed in Section 2.5.

2.1 Terrestrial and extraterrestrial neutrinos

High-energy neutrinos and hadronic gamma rays are produced when CRs interact with target matter via inelastic collisions, referred to as pp -interactions in the following, or with radiation fields (γ) via photo-hadronic ($p\gamma$) interactions. Since these interactions predominantly produce pions, the non-pion contribution will be neglected in what follows.

1. **CR interaction with matter** Generally the interaction between accelerated hadrons and target matter is described via inelastic hadronuclear interactions. However, the fraction of elements heavier than protons is subdominant in the astrophysical sources of interest, both in the acceleration region and the target interstellar medium (ISM). Hence, the focus will lie on proton-proton (pp) interactions. Such pp -interactions produce pions via,

$$p + p \rightarrow \begin{cases} p + p + \pi^0 & \text{(fraction 2/3)} \\ p + n + \pi^+ & \text{(fraction 1/3)}. \end{cases} \quad (2.1)$$

For a fixed-target collision, this requires a proton beam with threshold energy of $E_{p,thr} = 1.22$ GeV. The process above is correct for single pion production, however the energy available in cosmic accelerators will allow for many more pions, both charged and neutral, to be produced.

2. **Photo-hadronic interactions** At the threshold energy for a photo-hadronic interaction to take place, the interaction is dominated by the Δ^+ -resonance,

$$p + \gamma \rightarrow \Delta^+ \rightarrow \begin{cases} p + \pi^0 & (\text{fraction } 2/3) \\ n + \pi^+ & (\text{fraction } 1/3). \end{cases} \quad (2.2)$$

Applying relativistic kinematics to the reaction $p + \gamma \rightarrow p(n) + \pi$ allows to determine the proton energy threshold $E_{p,thr}$ for this process to happen,

$$E_{p,thr} = \frac{m_p m_\pi (1 + \frac{m_\pi}{2m_p})}{2\epsilon}, \quad (2.3)$$

with m_p the mass of the proton, m_π the mass of the produced pion in the process, and ϵ the energy of the photon in the lab frame. The interaction between the proton and the gamma ray was assumed to be head-on.

The charged pions (π^\pm) produced in both pp - and $p\gamma$ -interactions subsequently decay as

$$\begin{cases} \pi^+ \rightarrow \mu^+ + \nu_\mu \rightarrow e^+ + \nu_e + \bar{\nu}_\mu + \nu_\mu \\ \pi^- \rightarrow \mu^- + \bar{\nu}_\mu \rightarrow e^- + \bar{\nu}_e + \nu_\mu + \bar{\nu}_\mu, \end{cases} \quad (2.4)$$

where the average fraction of energy transferred from proton to neutrino is about 5%, i.e. $E_\nu \approx E_p/20$, for both pp and $p\gamma$ -interactions. Neutral pions (π^0) on the other hand predominantly decay as,

$$\pi^0 \rightarrow \gamma + \gamma. \quad (2.5)$$

The high-energy neutrino and gamma-ray production discussed above can occur at the source, during propagation over cosmological distances, or upon interaction in the atmosphere. Each of these are now discussed in more detail.

Astrophysical neutrinos Hadrons accelerated in astrophysical sources can interact within or close to the region of acceleration, especially in regions enshrouded by dust and gas or strong radiation fields. The two possible mechanisms to produce pions in cosmic accelerators are indicated in Equation 2.1 and Equation 2.2. Based on this, it can be concluded that the neutrino and gamma-ray energy fluxes are intimately connected through the amount of charged and neutral pions produced in pp - and $p\gamma$ -interactions. This justifies the reasoning given when discussing Figure 1.3, where it was mentioned that for a given gamma-ray flux it is possible to predict a related neutrino flux. The cumulative output of all high-energy neutrinos produced by pp - and $p\gamma$ -interactions in and near the cosmic accelerators gives rise to the astrophysical neutrino flux, which is of main interest in this work.

Atmospheric neutrinos A fraction of the CRs will not interact in or near their source and will be able to escape the accelerator. These particles will be deflected by (inter)galactic magnetic fields they encounter and might eventually end up in Earth's atmosphere. If a CR enters the atmosphere it will interact with an atmospheric nucleus and subsequently the atmosphere will act as a calorimeter, i.e. all initial energy is converted into secondary particles. Amongst the secondaries, mostly pions are produced in these interactions. After several interactions, shifting the secondaries to lower energies, the charged pions will decay according to Equation 2.4, resulting in the production of atmospheric muons and atmospheric neutrinos. Both of these form the background in the IceCube detector (Section 2.2) when searching for astrophysical neutrinos.

Cosmogenic neutrinos At the highest energies, the Universe becomes opaque to CRs, since they will be able to interact with the CMB via $p\gamma$ -interactions which is known as the Greisen-Zatsepin-Kuzmin (GZK) effect [14]. As the average energy of a CMB photon is $\epsilon = \langle h\nu \rangle \simeq 7 \times 10^{-4}$ eV, it follows from Equation 2.3 that the threshold energy of the proton must be greater than $\sim 10^{20}$ eV. This also indicates that a suppression is expected in the UHECR energy spectrum above $\sim 10^{20}$ eV. The UHECRs observed at the highest energies do not exceed this bound, suggesting that such a suppression might indeed be present. Neutrinos produced via the GZK effect are called cosmogenic neutrinos and are expected to possess higher energies than astrophysical neutrinos due to the threshold energy of the GZK effect. Dedicated neutrino experiments exist searching for these cosmogenic neutrinos [15, 16], although they have not been observed so far.

Apart from the three origins of neutrinos mentioned above, there are various other sources of low-energy neutrinos in the Universe. The closest extraterrestrial source of low-energy neutrinos is the interior of the Sun. Studying the solar neutrino flux has been pivotal in studies concerning neutrino oscillations [17]. Neutrinos originating from outside our Solar System have been observed as well, e.g. neutrinos from the supernova event SN1987A in the Large Magellanic Cloud [18, 19]. In addition, at the lowest energies, predictions within the context of a Λ -CDM cosmology exist of a residual flux of cosmological neutrinos originating from the Big Bang, which have not yet been observed. This cosmic neutrino background (C ν B) would have been decoupled from the primordial plasma in a similar fashion to the CMB. Lastly, neutrinos can originate from terrestrial sources, such as manmade nuclear reactors and Earth's core (geoneutrinos). Figure 2.1 shows the predicted neutrino flux as function of energy for the different origins discussed in this section.

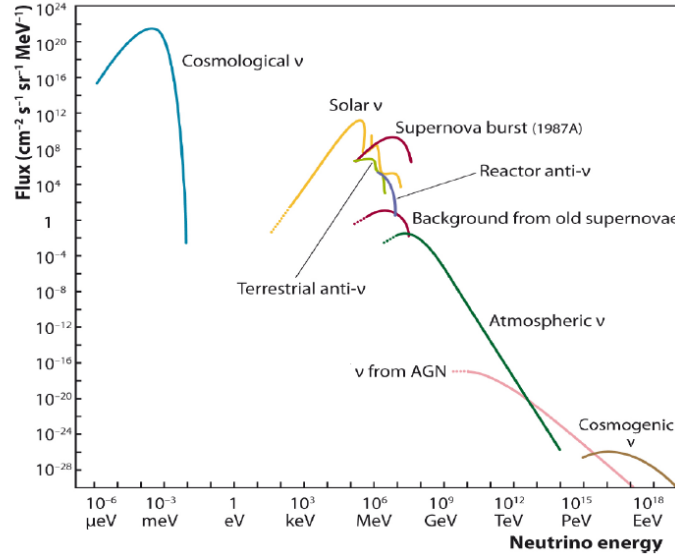


Figure 2.1: Schematic of the neutrino flux as a function of energy shown for the different sources discussed in the text. The low-energy range contains cosmological neutrinos (blue), solar neutrinos (yellow), supernova neutrinos (red), geoneutrinos (light green) and reactor neutrinos (purple). The high-energy range of the spectrum contains atmospheric neutrinos (dark green), neutrinos from AGN as part of the astrophysical neutrinos (pink), and cosmogenic neutrinos (brown) [20].

2.2 The IceCube detector

The chargeless and weakly interacting nature of the neutrino makes it a unique cosmic messenger to identify and study sources of (U)HECRs. However, these same properties make it extremely difficult to detect and analyse astrophysical neutrinos. Large detector volumes are required to observe a significant amount of these very weakly interacting particles. An example of such a large-scale neutrino detector is the IceCube Neutrino Observatory at the South Pole, buried deep within the Antarctic ice sheet. The detector encompasses a cubic kilometre of detector volume consisting of 86 hexagonally spaced vertical strings that reach depths of about 2.5 km deep in the South Pole ice. Each of these strings contains 60 Digital Optical Modules (DOMS), providing a total of 5160 sensors. A schematic of the IceCube observatory is shown in Figure 2.2. When a flux of high-energy neu-

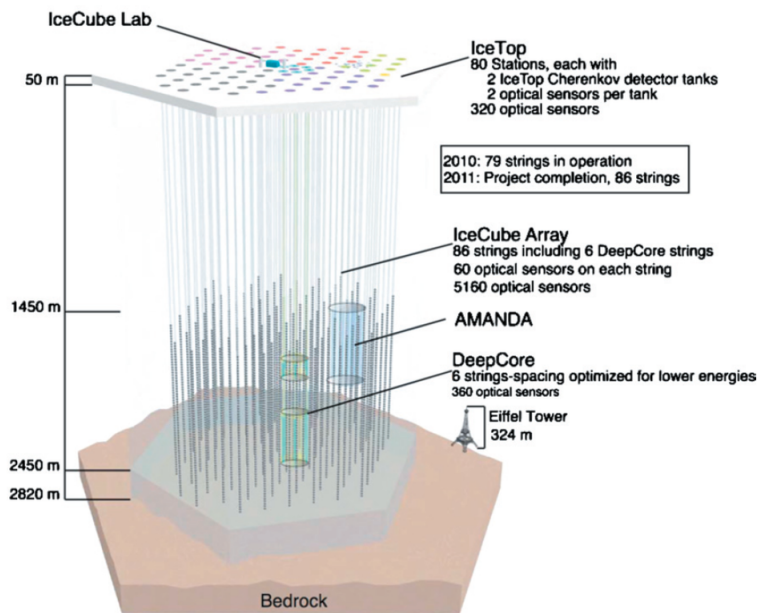


Figure 2.2: A schematic of the 1 km^3 IceCube Neutrino Observatory showing the scale of the 86 string structure w.r.t. to the Eiffel tower. The in-ice DeepCore component of IceCube, where the DOMs have a denser grid configuration, is also indicated as well as the precursor to IceCube, AMANDA-II. On the surface, the 1 km^2 IceTop array used to detect CRs is indicated, together with the IceCube Lab, which is the data acquisition center of IceCube and IceTop [21].

trinos propagates through the ice, some of them might interact with ice nuclei, thereby producing relativistic charged particles. These secondary particles subsequently emit Cherenkov radiation as they propagate at superluminal speeds through the ice. The Cherenkov photons are emitted in optical and UV frequencies, for which the South Pole ice is very transparent and hence also motivates the location of the IceCube Observatory. The DOMs, which are essentially photon multipliers, capture this Cherenkov light and amplify it. This allows to estimate the deposited energy and initial direction of the neutrino with a resolution depending on the nature of the interaction, as explained in more detail below.

A high-energy neutrino can interact weakly with an ice nucleus N via the exchange of a W -boson

$$\nu_\ell + N \xrightarrow{W} \ell + X \quad [\text{CC}], \quad (2.6)$$

which is called a Charged Current (CC) interaction. Part of the neutrino energy is transferred to the lepton $\ell \in \{e, \mu, \tau\}$ produced in the interaction while the rest goes into hadronic debris X . The interaction can also happen via the exchange of a Z -boson,

$$\nu_\ell + N \xrightarrow{Z} \nu_\ell + X \quad [\text{NC}], \quad (2.7)$$

which is called a Neutral Current (NC) interaction. Part of the initial energy is again transferred into hadronic debris X while the surviving neutrino carries away the rest of the energy.

These different types of interactions in combination with a certain neutrino flavor result in three classes of event topology in the detector: Cascades, tracks, and double bangs as shown in Figure 2.3. These different event topologies are discussed in some more detail in the following paragraphs.

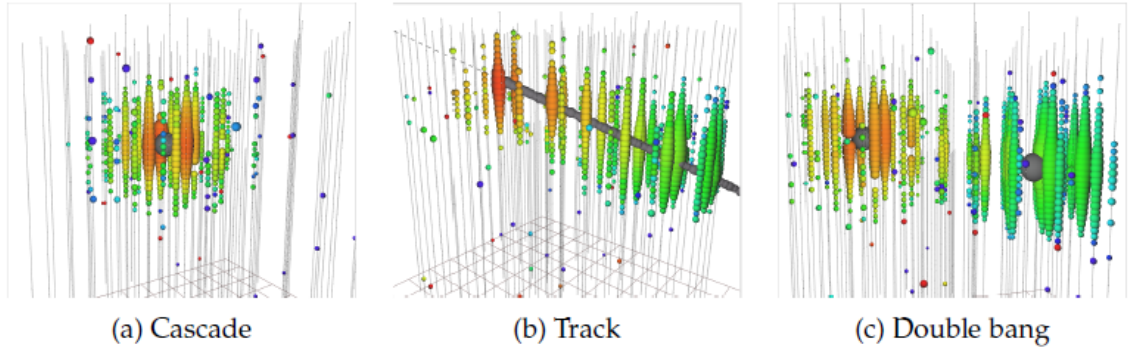


Figure 2.3: Different event topologies in the IceCube detector. (a) The cascade topology as a result of ν_e in a CC interaction or any of the neutrino flavors in a NC interaction. (b) A muon track from ν_μ in a CC interaction. (c) Double-bang signature from ν_τ in a CC interaction. It is noted that these are all simulated events [22].

Cascades A cascade or shower topology is the result of an electron (anti-)neutrino ν_e undergoing a CC interaction with an ice nucleus or any of the neutrino flavors in a NC interaction.

In the CC interaction the produced electron and hadronic debris undergo frequent interactions with the ice and thereby deposit their energy in the detector as shown in Figure 2.3 (a). For the NC interaction on the other hand, only the hadronic debris deposit its energy while the rest is carried away by the surviving neutrino. In both the CC and NC interactions, the pathlength of the secondary particles is short compared to the spacing between DOMs. Consequently a roughly spherical region of the detector lights up, allowing for the complete containment of the event inside the detector. Such an event topology has a good energy resolution but a poor directional resolution of $\sim 10^\circ$ [23].

Tracks Tracks, as shown in Figure 2.3 (b), are produced by a muon neutrino ν_μ undergoing a CC interaction. Due to the larger mass of the produced muon, as opposed to the electron, its energy

is deposited much slower and therefore the muon can escape the detector before being stopped completely. This also means that only a lower limit for the muon energy, and thus also for the original neutrino, can be determined. It is noted that such a track can be observed in the detector even if the CC interaction happened outside the detector.

The track topology, displaying an extended pathlength, allows for an accurate reconstruction of the muon direction (which is approximately equal to original neutrino direction above 1 TeV). It can be concluded that track events have a poor energy resolution as they are not fully contained but allow for a good directional resolution, i.e. $\sim 1^\circ$ [23].

Double Bang The double-bang topology is the most exotic and associated with a tau neutrino ν_τ undergoing a CC interaction. The simulated reconstruction of such an event is shown in Figure 2.3 (c). The first high energy deposition (=bang) is associated with the hadronic debris, which is accompanied by the production of a tau lepton. The tau lepton travels a distance of about 50 m per PeV away from the interaction vertex and subsequently decays. If this decay is to hadrons or an electron there will be a second energy deposition, which is the second bang. However, IceCube can only distinguish between the energy deposition if the tau has a sufficiently long lifetime in the detector frame, otherwise the energy deposition will appear as a single cascade in the detector. For intermediate energies the losses cannot be separated well, but may create two pulses in an optical module waveform (double pulse). Finally, decay lengths larger than 50 m allow to resolve and reconstruct the two energy depositions separately resulting in the double-bang topology [22].

In addition, it is also possible that the decay product is a muon (17% of the decays [24]), rather than hadrons or an electron, which results in an additional outgoing track.

When searching for neutrinos from astrophysical origin there are two important backgrounds that have to be taken into account. Firstly, muons produced in CR air showers could be mistaken in the detector as an event of astrophysical origin. Note that this is only a problem for atmospheric muons from the Southern hemisphere as the interior of the Earth acts as a natural shield for atmospheric muons produced in the Northern hemisphere. Consequently IceCube is more sensitive for sources in the Northern sky. Secondly, there is the background from atmospheric neutrinos produced in air showers. As opposed to the atmospheric muons, neutrinos from the Northern hemisphere now also form a background as they can easily traverse the interior of the Earth before interacting within or near the IceCube detector. The background rates of atmospheric muons and neutrinos seen by IceCube are 3 kHz and 6 mHz (all-sky), respectively.

2.3 Observations of the astrophysical neutrino flux

In 2013 the existence of a diffuse astrophysical neutrino flux was unambiguously proven by the IceCube Collaboration. Twenty-eighth high-energy particle events were presented which constituted the first solid evidence for neutrinos originating from astrophysical sources [6]. Since this discovery, various independent analyses have measured the diffuse neutrino flux [25, 26]. Here, we will highlight two of these, namely the analysis using high-energy starting events (HESE) and the analysis using through-going muon tracks.

HESE analysis The high-energy starting-event (HESE) sample aims to isolate high-energy neutrinos from atmospheric muons. In order to do so, the outer parts of the detector are used as a veto layer, aiming to select only events with a contained interaction vertex. This concept is shown in Figure 2.4 where a muon track passing through the veto layers is excluded (left) while the event with a contained interaction vertex is accepted (right). Note that this technique results in a smaller effective detector volume but in turn achieves a very pure event selection. It was the HESE analysis which was responsible for the initial discovery of the astrophysical neutrino flux in 2013.

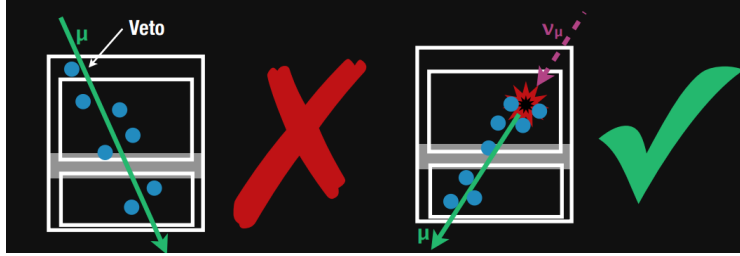


Figure 2.4: Schematic of HESE-analysis veto. Left: A muon track observed in the veto layers is excluded. Right: The interaction vertex lies within the reduced detector volume, and is therefore accepted [27].

The latest HESE analysis uses 7.5 years of IceCube data. Assuming a single power-law model, the best-fit diffuse neutrino flux in the 60 TeV-8 PeV energy range is [25],

$$\frac{d\Phi_{6\nu}}{dE} = (6.37^{+1.46}_{-1.62}) \left(\frac{E_\nu}{100\text{TeV}} \right)^{-2.87^{+0.21}_{-0.19}} \times 10^{-18} [\text{GeV}^{-1} \text{cm}^{-2} \text{s}^{-1} \text{sr}^{-1}]. \quad (2.8)$$

Both the normalization and spectral index are in terms of the flux summed over all neutrino species. The best-fit per-flavor flux of the 7.5 year HESE analysis, which is the result of Equation 2.8 divided by three, is shown in Figure 2.5.

Through-going muon analysis As opposed to the HESE analysis, the through going muon analysis uses the full detector volume without a veto layer. Instead the Earth is used as natural shield for atmospheric muons and therefore this analysis is only sensitive in the Northern hemisphere. The advantage of using the whole detector volume without veto layer is that muon neutrinos can interact well outside the detector and still be detected as muons by IceCube. However, this in turn increases the background of atmospheric muon neutrinos.

The most recent through-going muon analysis at the time of writing is based on 9.5 years of IceCube data. Assuming a single power-law model, the best-fit diffuse muon-neutrino flux in the 40 TeV-3.5 PeV energy range gives [26],

$$\frac{d\Phi_{\nu_{\mu}+\bar{\nu}_{\mu}}}{dE} = (1.44_{-0.24}^{+0.25}) \left(\frac{E}{100\text{TeV}} \right)^{-2.28 \pm_{0.09}^{0.08}} \times 10^{-18} [\text{GeV}^{-1} \text{cm}^{-2} \text{s}^{-1} \text{sr}^{-1}]. \quad (2.9)$$

This best-fit flux for the through-going-muon-analysis based on 9.5 years of data is shown in Figure 2.5 as well.

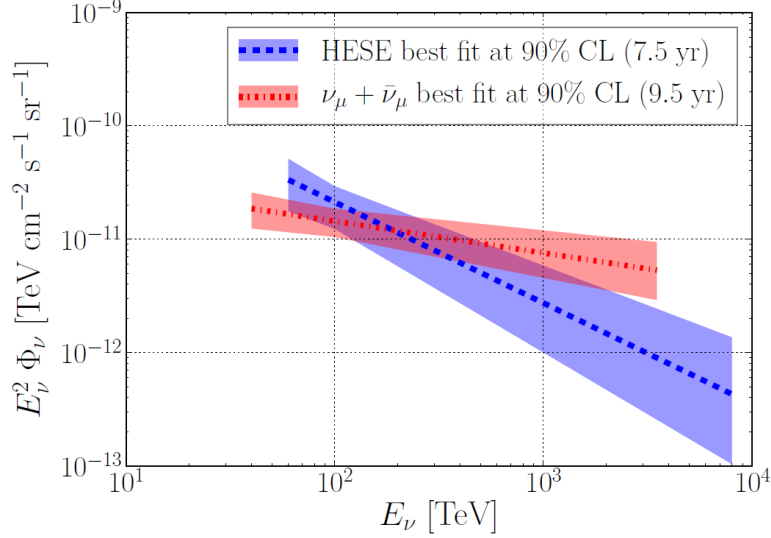


Figure 2.5: Best-fit diffuse neutrino flux from the latest HESE and through-going muon analyses discussed in the text. Credit: Pablo Correa.

2.4 Searches for point-like sources of neutrinos

The IceCube Collaboration has performed several searches in order to identify the origin of the astrophysical neutrino flux. These searches predominantly use track-like events because of their good angular resolution of $\sim 1^\circ$, as was discussed in Section 2.2. One of the more general approaches looks for steady point sources in a time-integrated all-sky search for clustering of neutrino events on a grid of $\sim 0.1^\circ \times \sim 0.1^\circ$ pixels on the sky [28]. The latest results of this analysis use ten years of IceCube data collected between April 6 2008 and July 10 2018 [29]. The most significant point in the Northern hemisphere from scanning the sky in this way is coincident with the Seyfert II galaxy NGC 1068, which has a post-trial significance of 2.9σ .

However, the results are still consistent with the background-only hypothesis. Figure 2.6 shows the point-source sensitivity of IceCube at 90% confidence level as a function of declination¹ (δ), for E^{-2} and E^{-3} neutrino spectra. This sensitivity indicates that if a point source would emit a flux of neutrinos larger than this value, an excess of neutrinos could have been observed in the data. This point-source sensitivity can therefore serve as reference for neutrino production models, as will be done in Section 6.4 and Section 6.5. Moreover, it is also concluded from Figure 2.6 that the

¹Declination is one of the two angles that locate a point on the celestial sphere in the equatorial coordinate system, the other being right ascension. Points north of the celestial equator have positive declinations, while those south have negative declinations.

sensitivity for positive declinations are significantly lower as opposed to the sensitivity for negative declinations. This is a direct consequence of the reduced background of atmospheric neutrinos and muons from the Northern hemisphere (Section 2.3).

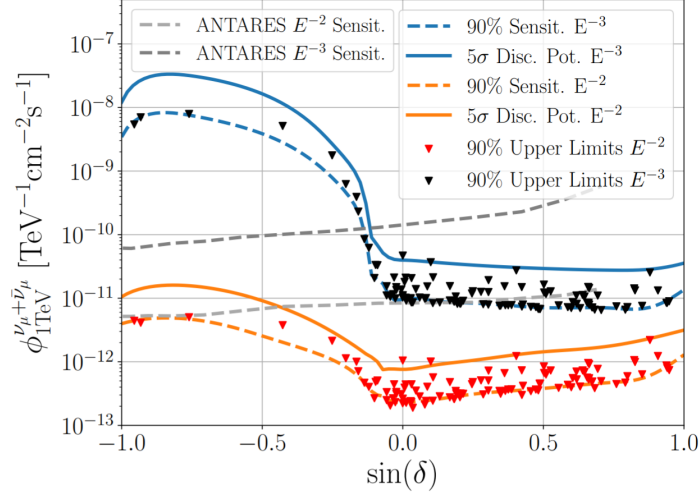


Figure 2.6: 90 % C.L. median sensitivity and 5σ discovery potential as a function of source declination for a neutrino source with an E^{-2} and E^{-3} spectrum. The triangles indicate the 90% upper limits for some specific point sources that were analysed. The dashed grey curves show the 90 % C.L. median sensitivity from 11 years of ANTARES data [28]. ANTARES is a neutrino detector residing 2.5 km under the Mediterranean Sea off the coast of Toulon, France.

2.5 Compelling evidence for the first cosmic neutrino source: TXS 0506+056

On the 22nd of september 2017 a high energy muon-neutrino was detected by IceCube with an estimated energy of 290 TeV, determined from the corresponding track which deposited an energy of 23.7 ± 2.8 TeV in the detector. The probability that this events is of astrophysical origin is estimated to be 56.5 % [30]. An illustration of the observed muon track in the IceCube detector is shown in Figure 2.7 where the temporal evolution is indicated by a colour profile. The size of a coloured sphere is proportional to the amount of light observed at the DOM, with larger spheres corresponding to stronger detected signals.

The event, designated IC170922A, was communicated 43 s after observation via an automated alert to observatories all over the globe providing an initial estimate of energy and direction of origin. Five days later the Fermi-LAT Collaboration reported that the direction of the event is consistent with the previously known gamma-ray blazar TXS 0506+056. Moreover, this blazar happened to be in a state of enhanced gamma-ray activity, i.e. a flaring state. Follow-up studies of the blazar led to the detection of gamma rays with energies up to 400 GeV by the Major Atmospheric Gamma Imaging Cherenkov (MAGIC) Telescope. The observation of TXS 0506+056 in a flaring state is of particular interest for the astrophysical neutrino production where gamma rays and neutrinos fluxes are expected to be intimately connected (Section 2.1).

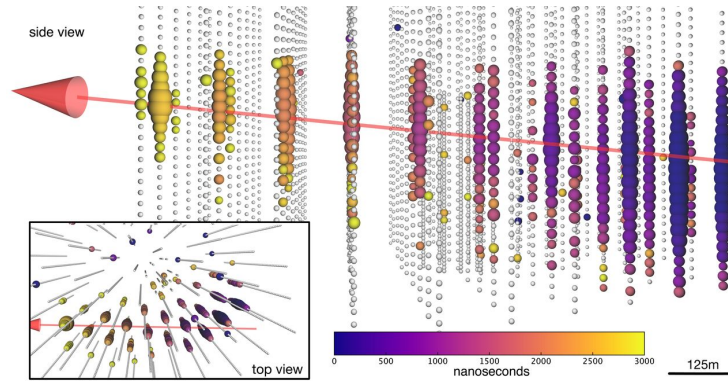


Figure 2.7: The event IC170922A detected by the IceCube Neutrino Observatory at the South Pole. This illustration also shows the 86-string structure, each consisting of 60 DOMS, as discussed in the text. Temporal evolution of the event is indicated by the colour profile where blue and yellow indicate earlier and later times, respectively [31].

This coincident observation was followed by an exclusive archival IceCube analysis on TXS 0506+056. It was concluded that an excess of high-energy neutrinos was observed from the direction of TXS 0506+056 between September 2014 and March 2015. This IceCube analysis is additional independent evidence for the blazar TXS 0506+056 being a source of high-energy neutrinos. However, the blazar was not found to be in a gamma-ray flaring state in the period from September 2014 to March 2015. Due to the relation between gamma rays and high energy-neutrinos expected from a cosmic accelerator, this could imply a substantial absorption of gamma rays at GeV energies.

The coincidence of an IceCube alert with a previously-known flaring blazar, combined with a neutrino excess found in archival data, provides strong evidence but it is not enough to warrant a discovery. Moreover, the IceCube Collaboration has constrained the cumulative contribution of Fermi-2LAC blazars. This analysis sets limits on the possible cumulative contribution of Fermi-2LAC blazars, of which TXS 0506+056 is part, to the diffuse TeV-PeV neutrino flux [8]. Therefore Fermi-blazars cannot be the sole origin of the astrophysical neutrino flux observed by IceCube, which remains unknown at the time of writing.

Although the origin of astrophysical neutrinos remains undisclosed, observations are pointing towards heavily obscured gamma-ray sources, as was discussed in Chapter 1. In this work the focus lies on modeling neutrino production in a sub-type of such hidden sources, i.e. (ultra)-luminous infrared galaxies.

Chapter 3

Great Observatories All-sky LIRG Survey objects as gamma-ray dim neutrino sources

In Section 3.1 different sub-types of galaxies with extreme star-formation rates are discussed. One of these galaxy types are (ultra)-luminous infrared galaxies (U/LIRGs), exhibiting an extreme IR luminosity $L_{IR} > 10^{11} L_{\odot}$, which will be the main focus of this work. In Section 3.2 a quantitative discussion is given on U/LIRGs as gamma-ray obscured high-energy neutrino sources. More specifically, the focus in this work will lie on U/LIRGs in the Great Observatories All-Sky LIRG Survey (GOALS) sample, which provides extensive electromagnetic data for the ~ 200 most nearby U/LIRGs. In Section 3.3 an introduction to GOALS is given, where the focus lies on GOALS observations and data relevant for the construction of the neutrino-production framework in the remainder of this work. Finally, an overview of the main assumptions and relevant quantities to be included in this framework is given in Section 3.4.

3.1 Starburst galaxies

A starburst galaxy is undergoing an exceptionally high rate of star formation compared to the long-term average rate of star formation in that galaxy. Starburst episodes exhibit star-formation rates of 10-100 solar masses (M_{\odot}) per year as opposed to quiescent star formation, such as in the Milky Way, for which $(1.65 \pm 0.15) M_{\odot}/\text{year}$ is found [32]. Rather than being a distinct type of galaxy, a starburst galaxy is a certain phase in the evolution of (merging) galaxies as the molecular gas supplying the burst is exhausted over time. A starburst episode can occur in the galactic nucleus (a nuclear starburst) or throughout the entire galaxy. In this work the focus will be on nuclear starbursts. Even more so, the model developed here is only justified for nuclear starburst regions.

Typically starburst galaxies are classified as Wolf-Rayet galaxies, blue compact galaxies, and (ultra)-luminous infrared galaxies (U/LIRGs). However, not all galaxies showing signs of significant starburst activity belong to one of these sub-types, such as Messier 82 (M82) and NGC 253. M82 and NGC 253 are of particular interest because of their proximity to Earth, expressed in terms of luminosity distance (D_L) in what follows.

M82, located at $D_L \approx 3.8$ Mpc [33], is the closest starburst galaxy which experiences gravita-

tional interactions with its galactic neighbour, M81, causing it to have an extraordinarily high rate of star formation. Tidal interactions and mergers are a common trigger for starburst periods. NGC 253 at $D_L \approx 3.9$ Mpc [34] is a giant, barred spiral galaxy with a central starburst region. It is one of the brightest and dustiest spiral galaxies in the sky. Although there is no obvious companion or trigger for the starburst in NGC 253, kinematic studies suggest that the galaxy may have been involved in a past merger [35]. Both M82 and NGC 253 will play a central role in this work.

Blue Compact Galaxies Blue compact galaxies are dust-free objects with low metallicity and total mass. As a result of being dust-free and containing a large number of young massive stars in the starburst region, blue compact galaxies typically appear blue in optical colours. This can be seen in Figure 3.1, which shows an optical image of galaxy SBS 1415+43 acquired by NASA/ESA Hubble Space Telescope. The fact that individual stars can be identified in optical wavelengths indicates the absence of large amounts of dust in these galaxies. It can be concluded that blue compact galaxies are not of interest as gamma-ray obscured neutrino sources.

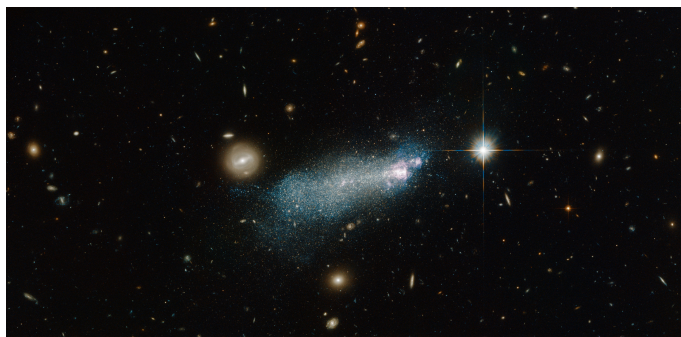


Figure 3.1: Compact dwarf galaxy SBS 1415+437 observed by NASA/ESA Hubble Space Telescope [36].

Wolf-Rayet galaxies Stars with an initial stellar mass exceeding $25 M_{\odot}$ go through an evolutionary phase called the Wolf-Rayet (WR) phase. During this phase the so-called WR star is very hot with a surface temperature well over 25000 K, as opposed to ~ 6000 K for the Sun, which makes them very luminous. Moreover, during the WR phase the star suffers extreme mass losses in the form of strong stellar winds, driven by extreme radiation pressure.

WR galaxies are a rare population of galaxies that host a significant fraction of stars during their WR phase. However, these stars are not only observed in WR galaxies but also in galaxies like the Milky Way and the other starburst galaxy types. While WR stars are rare in the Milky Way, they are expected to be more numerous in starburst galaxies. Figure 3.2 shows a star in the WR phase observed by the Hubble Space Telescope, highlighting the chaotic and energetic outflows during this stage. WR galaxies will not be studied as potential gamma-ray obscured neutrino sources. However, the mechanical energy transfer to the interstellar medium in the form of high-velocity stellar winds from WR stars will be of interest when discussing shock-accelerated particles and galactic-scale outflows (Section 5.2.2).

(Ultra)-Luminous Infrared Galaxies U/LIRGs are characterised by their tremendous amount of infrared (IR) emission, which is larger than the total electromagnetic luminosity of a typical non-interacting galaxy. Per definition, U/LIRGs have an IR luminosity of



Figure 3.2: Hubble Space Telescope image of nebula M1-67 around Wolf-Rayet star WR 124 [37].

$$\text{LIRG: } L_{IR} \equiv L_{[8-1000\mu m]} > 10^{11} L_{\odot}$$

$$\text{ULIRG: } L_{IR} \equiv L_{[8-1000\mu m]} > 10^{12} L_{\odot}.$$

Figure 3.3 shows the Spectral Energy Distribution (SED) of the ULIRG Mrk 273 reflecting the immense IR output as opposed to the other frequencies. The extreme IR luminosity indicates large amounts of dust and gas present combined with an enormous energy budget, two key features for high-energy neutrino production and gamma-ray attenuation, as discussed in next section.

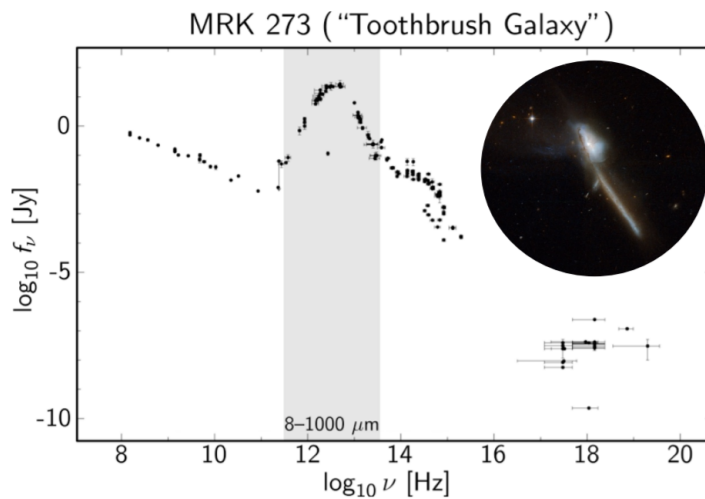


Figure 3.3: Spectral Energy distribution (SED) of the ULIRG Mrk 273, also referred to as the toothbrush galaxy (top right corner). The SED reflects the enormous IR output in the 8-1000 μm range (shaded band) [38].

3.2 U/LIRGs as promising gamma-ray obscured neutrino sources

Studies have shown that the great majority of U/LIRGs exhibit signs of an interaction/merger of galaxies rich in gas (see Section 3.3.3). Such interactions can trigger funnelling of material from kpc-scales to the innermost regions of the galaxy due to the loss of angular momentum in the merger/tidal interaction. Pressure waves generated by large amounts of gas coming together in the central region are expected to trigger intense star formation and form the starburst region. This results in a population of short-lived, hot, massive stars and/or AGN activity. The strong UV radiation field from such a stellar population has sufficient energy to partially ionize the surrounding gas and dust of the giant molecular clouds in which they formed. This results in so-called H II regions. Thermal radio emission is produced in H II regions via free-free¹ emission (Bremsstrahlung), which is directly proportional to the production rate of ionizing photons from the young hot stars. The strong radiation field in starburst regions will also significantly heat the surrounding dust and gas, which subsequently re-radiates the light as thermal emission. Although this mechanism generally explains the enormous IR output in U/LIRGS, the presence of an AGN can significantly contribute to the IR as well. In case of an AGN, it is the accretion disk and/or jet-torus interaction that heats the surrounding matter. Unprocessed X-ray and/or UV photons can provide direct evidence about the nature of the central engine. Nevertheless, the severe attenuation of optical-UV and X-ray frequencies makes direct identification often impossible. Techniques have been developed over the years to identify the presence of a buried AGN and to constrain the relative contribution of a starburst or AGN component [39, 40, 41]. The exact nature of the central engine in U/LIRGs and their relative contribution are a matter of active debate.

Apart from strongly irradiating its surroundings, the massive stellar population in U/LIRGs also transfers enormous amounts of kinetic energy to the ambient medium. Interesting here is the significant amount of stellar mass loss via high-velocity stellar winds, as was already mentioned for the WR stars in Section 3.1. These stellar winds contribute to metal enrichment of the interstellar medium (ISM) and particle acceleration via stellar-wind induced shocks.

Massive stars advance significantly faster through their stellar evolution than low-mass stars, which results in an increased rate of core-collapse supernova explosions (Section 4.1.2) in U/LIRGs as opposed to non-starburst galaxies. The expelled matter of such supernova (SN) explosions enriches the ISM with heavy elements (metals) fused by the progenitor over its lifetime (Section 4.1.2). These injected metals coalesce into dust and can thereby enshroud the central regions even more. Moreover, part of the kinetic energy released in the SN explosion is converted to particle acceleration via the first order Fermi acceleration mechanism (Section 4.4). An important feature of U/LIRGs is that particle acceleration in SN remnants is expected to reach higher energies in the turbulent metal-enriched ISM as opposed to isolated SN events (Section 4.5.3). This is required in order to produce neutrinos within IceCube's sensitive energy range.

Acceleration of electrons in SN leads to non-thermal (synchrotron) radio emission which is also observed in starburst galaxies. Both thermal (Bremsstrahlung) and non-thermal (synchrotron) radio emission are therefore (indirectly) related to supernova activity and star-formation activity.

Hadrons accelerated in the prolific SN remnants, stellar wind collisions, and/or AGN activity will interact abundantly with the large dust and gas densities via inelastic pp -interactions and/or with the strong radiation fields present via $p\gamma$ -interactions in the nuclear regions. Such interactions copiously produce gamma rays and high-energy neutrinos via the decay channels discussed in Section 2.1. While neutrinos can escape unimpeded, the gamma rays could be significantly obscured

¹"Free-free" refers to the fact that the radiation is created by electrons that are not in a bound state and remain free after the emission of the photon.

via $p\gamma$ -interactions with the dust and/or pair production.

Based on the efficient particle acceleration combined with increased dust and metal-rich gas densities in starburst regions of U/LIRGs, it is concluded that U/LIRGs are promising gamma-ray obscured high-energy neutrino source candidates. In this thesis the focus lies on studying and modeling neutrino production via pp -interactions in pure-starburst U/LIRGs. This research is done using electromagnetic data from the Great Observatories All-Sky LIRG Survey (GOALS), providing extensive electromagnetic data for ~ 200 nearby U/LIRGs. In the next section the GOALS sample and relevant observational data of GOALS is introduced which will allow us to justify assumptions and clarify steps in the remainder of this work.

3.3 Great Observatories All-Sky LIRG Survey (GOALS)

At the time GOALS was established, ULIRGs were already well-studied, while LIRGs suffered from a lack of attention. This is partially due to the fact that LIRGs form a morphologically diverse group of galaxies, unlike ULIRGs which are nearly always involved in the final stages of a merger between two galaxies rich in gas (see Section 3.3.3). The primary objective of the GOALS survey is to fully characterize the diversity of properties observed in the nearest U/LIRGs. This is achieved through a multi-wavelength survey combining data from NASA's Spitzer (IR), Hubble Space Telescope (optical), Chandra (X-ray), and GALEX (UV) observatories in a comprehensive imaging and spectroscopic survey containing 180 LIRGs and 21 ULIRGs. The median redshift of the sample is $z = 0.0215$ (~ 95.2 Mpc), with the closest source at $z = 0.0030$ and the most distant source at $z = 0.0918$. GOALS objects were originally selected from the IRAS Revised Bright Galaxy Sample (RGS) as sources with a luminosity threshold of $L_{IR} \geq 10^{11} L_{\odot}$. The RGS on its turn consists out of a complete flux-limited sample of 629 galaxies that have IRAS 60- μm flux densities above 5.24 Jy and Galactic latitude $|b| \geq 5^{\circ}$ [42].

The involvement of GOALS in understanding and accurately modeling neutrino production and gamma-ray attenuation in U/LIRGs is crucial. This is outlined in the next few paragraphs and along the way interesting GOALS sources will be discussed for this work and future works on the topic.

3.3.1 Multiwavelength observations

The LIRG VV 114 in Figure 3.4 is a source in the GOALS catalogue. Panel a) shows an observation of the LIRG in optical wavelengths. This optical observation highlights the obscuring effect of dense dust structures. In panels d) and e) these prominent structures fade away, but an extended structure is still visible. This is the result of observing far-IR wavelengths which track heated dust grains and are significantly less obscured than optical wavelengths. In panel f) the wavelength shown corresponds to non-thermal radio emission which essentially tracks particle acceleration and therefore reveals the activity of central engines, as discussed in Section 3.2. The combination of these panels, observed at different wavelengths, shows the importance of multiwavelength observations to pinch through dust-enshrouded regions hiding the energetically dominant regions in U/LIRGs.

Once the locations of the energetically dominant regions have been identified, constraining the spatial extent and the nature of the emission from these regions is also of particular interest when computing a neutrino flux. Indeed, the prolific SN activity in U/LIRGs leads to efficient particle ac-

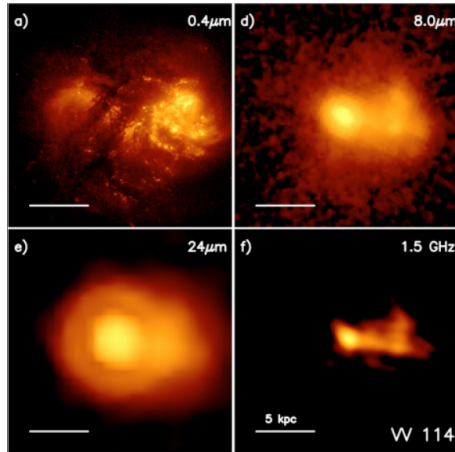


Figure 3.4: The LIRG VV 114, a source in the GOALS catalogue. The combination of these panels shows the importance of multi-wavelength observations to learn more about LIRGs [43].

celeration via first order shock acceleration which subsequently results in neutrino production. The rate at which SN events occur in the energetically dominant regions is therefore a crucial parameter to determine (Section 4.5.1 and Section 4.5.2). The extreme extinction due to the large amounts of gas and dust present in starburst U/LIRGs do not allow for direct SN counting via optical images in the most dust-obscured regions. However, it was already discussed that also non-thermal and thermal radio emission trace SN activity. Radio emission has the advantage to be unaffected by matter (except at the lowest frequencies). In addition, the high angular resolution achieved by interferometric radio imaging allows to resolve individual sources and measure the sizes of the energetically dominant regions. Moreover, near-IR observations have gained interest over the years to trace SN activity, especially with the advancements in adaptive optics. Near-IR wavelengths significantly reduce the extinction as opposed to optical wavelengths, but might suffer more severe attenuation in the most obscured regions as opposed to the unobscured radio waves. Combining high-resolution interferometric radio data with near-IR observations is therefore the optimal way to detect and characterize SN activity in U/LIRGs.

In GOALS, characterizing the energetically dominant regions using observations of the 33 GHz continuum by the Very Large Array [44] is achieved for 22 local U/LIRGs. This dedicated approach allowed to put stringent constraints on the spatial extent of these regions and star formation within. Typical scales for these compact starburst regions, which are of interest in this work, are a few 100 pc. In addition, size estimations of energetically dominant regions for a larger set of GOALS sources using IR observations is available, although with less stringent constraints [45].

3.3.2 ISM density: line emission from tracers and black-body emission

The volume density of the interstellar medium (ISM) in compact starburst regions is of main interest in this work as it determines whether or not this region efficiently produces high-energy neutrinos (Section 5.3). In this section we briefly discuss two of the main techniques used to infer ISM densities.

Line emission The abundant molecular gas in starburst regions, which supplies gas for star formation and serves as a target for inelastic scatterings, mainly consists of molecular hydrogen (H_2). However, cold H_2 is not directly observable via electromagnetic emission as it is a diatomic molecule with identical nuclei which does not possess a permanent dipole moment and therefore no transitions between quantized rotational states. The second most abundant element, helium, suffers from similar problems in cold clouds. Fortunately, the molecular ISM also contains heavier elements, with oxygen and carbon the most abundant elements. Under typical conditions in cold molecular clouds such oxygen and carbon elements fuse into carbon monoxide (CO). CO has a weak permanent dipole moment and a ground rotational transition with a low excitation energy. This allows CO to be excited even in cold molecular clouds. Moreover, CO line emission falls in a fairly transparent atmospheric window which allows for ground-based observations. Therefore CO emission is frequently employed as a tracer of the bulk distribution of H_2 . The total molecular mass is typically estimated from the CO luminosity via an empirical conversion factor [46]. Whether or not to use the same value for the conversion factor in quiescent star-forming galaxies and starburst galaxies is a matter of active debate [47]. It is crucial to constrain this conversion factor as much as possible because it directly affects the total amount of inferred molecular mass and as such the estimates of the amount of target matter and star-formation rate. We also note that CO line emission serves as a tracer for moving gas masses such that it can be used to characterize the kinematics of such clouds. This will be relevant when discussing the galactic-scale outflow in starburst galaxies.

However, CO is typically not the best tracer for dense gas regions such as the nuclear starburst regions of interest in this work. The ground state transitions of HCN and HCO^+ are examples of tracers that are typically used to characterize hot and dense gas in galaxies [48].

Black-body dust emission An alternative approach to probe ISM masses is to observe the optically thin Rayleigh-Jeans continuum emission from heated dust grains. For high-mass star-forming galaxies, as is characteristic for U/LIRGs, this approach is particularly interesting because the dust continuum can be detected by the Atacama Large Millimeter Array (ALMA) in just a few minutes of observation time. This is in contrast with the observations required to estimate the CO luminosity, which require an hour or more [49].

3.3.3 U/LIRG morphology

As already mentioned in Section 3.2, the extreme activity in U/LIRGs is typically a consequence of the tidal interactions between and/or merging of galaxies. In terms of merging systems, there are so-called minor mergers in which one of the galaxies is significantly larger than the other and major mergers where the galaxies are of approximately the same size. The various interaction stages in which U/LIRGs are observed result in a number of different morphologies, especially for LIRGs. In [50] a visual classification system is discussed which accounts for all possible interaction stages in a sample of 65 GOALS U/LIRGs that were observed. The visual classification of [50] is: single galaxy with no sign of interaction (s), minor merger for galaxies with mass difference of $< 4 : 1$ (m), major merger for a separated galaxy pair (M1), major merger for an interacting galaxy pair (M2), major merger for merging galaxies with two nuclei and tidal tails (M3), major merger for merging galaxies with a single nucleus and tidal tails (M4), and a diffuse merger remnant without bright tidal tails (M5). Figure 3.5 shows examples of the visual morphological classification scheme in [50]. In Figure 3.6 the distribution of morphology as function of infrared luminosity is shown for 65 GOALS ULIRGs. It is concluded that all U/LIRGs are typically major mergers while LIRGs range from single galaxies to M4.

3.3. GREAT OBSERVATORIES ALL-SKY LIRG SURVEY (GOALS)

The fact that objects in the GOALS sample range from single galaxies to interacting systems with (nearly) visible separation of the nuclear regions implies a variety of physical environments in the sample. Moreover, the significant separation within an interacting system (e.g M2 and M3 in Figure 3.5) could also indicate significantly different stellar/AGN activity in the system itself. As such, a source-by-source investigation is required to model neutrino production. An example of this is given in Section 6.5.

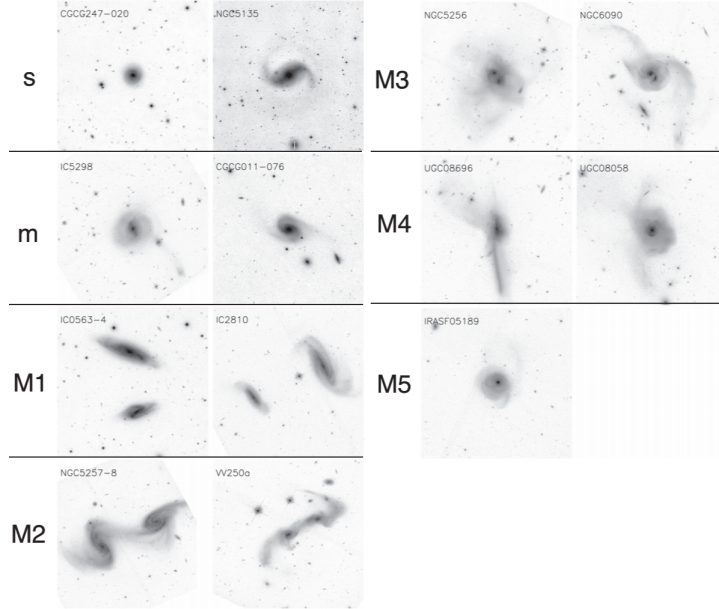


Figure 3.5: Examples of the visual morphological classification scheme [50].

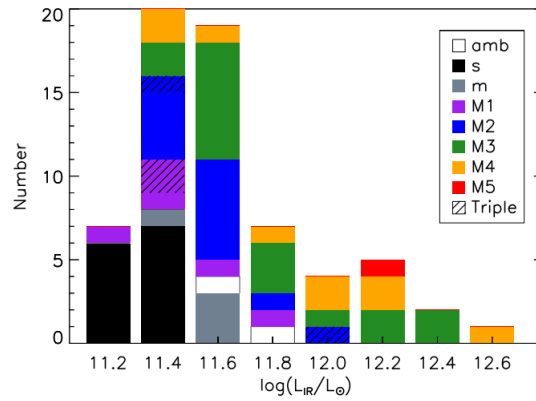


Figure 3.6: Distribution of morphology types discussed in Figure 3.5 as function of infrared luminosity for the selected sample in [50]. Contributions from objects classified as ambiguous (white) and triple systems (hashed) are also included.

3.3.4 GOALS ULIRG Arp 220

Arp 220, a major merger of two disc galaxies classified as M4 in the morphological classification scheme (Figure 3.5), is the closest ULIRG to Earth at $D_L \approx 77$ Mpc [51]. Due to its proximity to Earth it is the best studied ULIRG in the GOALS sample. Correspondingly, most of the parameters required to predict a neutrino flux, identified in Chapters 4 to 6, can be found in the literature. Therefore this object will be of great interest in this work.

Arp 220 has a huge IR output of $\log_{10}(L_{IR}/L_{\odot}) = 12.24$, which is among the most luminous in the GOALS sample. The large IR output indicates a high star-formation rate and as such a high supernova rate, as was discussed in Section 3.2. In [52] a total star-formation rate of approximately $220 M_{\odot} \text{yr}^{-1}$ was calculated based on the far-infrared luminosity and in [53] a total SN rate of $4 \pm 2 \text{yr}^{-1}$ was inferred from radio observations, as opposed to $1.63 \pm 0.46 (100 \text{yr})^{-1}$ for the Milky Way [54]. It is important to note that the total SN rate mentioned here is based on global observations of Arp 220, however, in this work we are interested in the nuclear starburst regions, where the SN rate is not necessarily equal to the total SN rate on more extended scales.

CO and dust continuum observations (Section 3.3.2) with ALMA at a 90 milliarcsecond resolution clearly resolve two highly compact regions (nuclei) separated by a distance of approximately 369 pc. For the western nucleus the major gas and dust emission extends to a radius of ~ 74 pc while the eastern nucleus is more extended with a radial extent of ~ 111 pc [55]. Both nuclei have been estimated to have an integrated hydrogen column density of $N_H \sim 10^{25-26} \text{cm}^{-2}$. This makes Arp 220 particularly interesting as a gamma-ray obscured neutrino source.

3.3.5 GOALS LIRG Arp 299

The literature study done within this work revealed that U/LIRGs are observed over a wide variety of merger states (Section 3.3.3). We found that the nuclear starburst/AGN regions of the galaxies taking part in the merger could have significantly different stellar/AGN activity. This motivated us to search the GOALS sample for an object with a well-resolved nuclear structure to support this claim. This investigation of the GOALS sample drew our attention to the LIRG Arp 299, which is now discussed in more detail, and will be used as an example for our neutrino model in the remainder of this work.

Arp 299 (also known as IC 694 and NGC 3690) is one of the most powerful merging galaxy systems in the local Universe with $\log(L_{IR}/L_{\odot}) = 11.88$ and located at $D_L = 44.8$ Mpc [56], consisting of two galaxies that are in an intermediate merger stage. This LIRG has been classified as M3 in the morphological classification scheme (Figure 3.5) because of the appearance of two highly overlapping disks (known as C+C') with clear tidal features. Observations of the mid-IR and radio continuum emission (which track star-forming activity) of ARP 299 revealed the regions A, B, C and C' as dominant emitters of these wavelengths. These regions are indicated in Figure 3.7.

Near-IR studies, with higher spatial resolution, were able to resolve two components in region B, B1 and B2. Region B1 is coincident with the mid-IR and radio continuum emission peaks. The projected nuclear separation between A and B is ~ 4.5 kpc and C+C' shows a highly overlapping disk structure [57]. The brightest component at mid-IR and radio wavelengths, and therefore expected to have the largest star-forming activity, is the nuclear region of the eastern galaxy Arp 299-A. The SN activity was revealed by a ~ 2.5 year monitoring campaign at 5.0 GHz which allowed to estimate the lower limit $\mathcal{R}_{SN} \gtrsim 0.8 \text{yr}^{-1}$ in the central 150 pc [56]. Moreover, a starburst-driven outflow was detected by the Low-Frequency Array (LOFAR) [59] which is of interest as it prevents CRs from producing secondary particles by advecting them (Section 5.2.2).

AGN activity has been detected in both Arp 299-A and on the opposite side of the galaxy in the

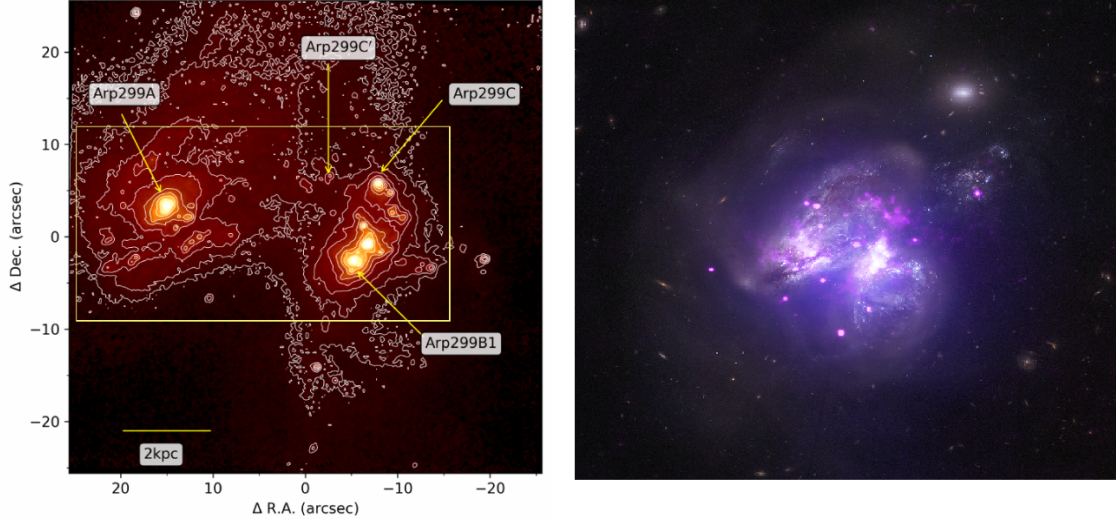


Figure 3.7: Arp 299. Left: Near-IR image at $\lambda \approx 1.6 \mu\text{m}$ which mostly traces the stellar emission (Hubble Space Telescope/NICMOS) [57]. The strongest IR-emitting regions in the system are indicated. Right: Composite image with X-ray data from Chandra (pink), higher-energy X-ray data from NuSTAR (purple), and optical data from the Hubble Space Telescope (white and faint brown) [58].

Arp 299-B1 nucleus. However, the former has been estimated to be much less luminous than the latter. Moreover, hard X-ray observations revealed that the B1 nucleus has an AGN surrounded by Compton-thick columns of matter [57], i.e. with column densities $N_H > 10^{24} \text{ cm}^{-2}$. Therefore it can be concluded that the nuclear activity in region A and B1 are indeed significantly different.

Just as for ARP 220, the starburst-driven neutrino flux expected from the LIRG ARP 299 will be modeled (Section 6.5) using the neutrino-production framework constructed in this work. First of all this is motivated by the well-resolved and observed nuclear regions in the merging system. Moreover, as Arp 299 is located relatively close to Earth, it is interesting to compare the predicted neutrino flux to the point-source sensitivity of IceCube (Section 2.6).

Although the focus will lie on neutrino production in the A nucleus (Section 6.5), future studies might be interested to look into the B1 nucleus as a gamma-ray obscured neutrino source. A tidal disruption event (TDE), when a star is torn apart by a black hole and the stellar debris falls back to the black hole resulting in a characteristic flare, has been found to coincide with the B1 nucleus of Arp 299. This is particularly interesting since a recent study traced an energetic IceCube neutrino back to a TDE of a different galaxy [60].

3.4 Starburst-driven neutrino-production framework

So far U/LIRGs have been identified as interesting gamma-ray obscured high-energy neutrino source candidates. It also has been argued that the expertise of GOALS on the electromagnetic data and state-of-the-art astronomy is crucial to accurately model neutrino production in these sources. This discussion, based on an extensive literature study, is novel as this is the first time GOALS objects are investigated as obscured high-energy neutrino sources. In the rest of this thesis a framework for neutrino production in starburst-driven GOALS U/LIRGs is constructed. Ana-

lytic expressions for the relevant neutrino-production parameters will be derived and maximally expressed in terms of GOALS observables, i.e. electromagnetic observables which have been extensively studied and observed by GOALS. An overview of this framework is given below, as well as the main assumptions used in the construction of this model.

As a result of the the young, hot, and massive stellar population in U/LIRGs, an increased amount of SN events and high-velocity stellar-wind activity is expected. Both serve as injection of accelerated particles into the enhanced ISM densities of the starburst regions. After injection, part of the accelerated hadrons will participate in pp -interactions which then results in high-energy neutrino production via pion decay (Section 2.1). Neutrino production due to $p\gamma$ -interactions between a cosmic ray (CR) and a photon (γ) provided by the stellar radiation field in the starburst region is not considered in this model. This is justified for starburst regions with high ISM densities where the pp -interaction timescales are significantly smaller as opposed to the typical timescales of $p\gamma$ -interactions. Furthermore, neutrino production due to AGN activity, i.e. $p\gamma$ -interactions in the jet and/or pp -interactions via jet-cloud/torus interactions, falls outside the scope of this work. Nevertheless, a fraction of the GOALS objects undoubtedly contains one or more luminous AGN which might have a significant contribution to the neutrino production, e.g. the B1 region in Arp 299.

The injection of accelerated particles competes with processes removing these particles from the neutrino-production regions. The processes responsible for this are spatial diffusion due to magnetic field structures and advection via galactic-scale outflows driven by starburst activity. In addition to this, the particle's propagation is also affected by momentum losses which for protons mainly happens via Coulomb interactions, ionization, and inelastic pp -interactions. However, for the CR energies of interest in this work, the inelastic pp -interaction is the only relevant process. Taking the aforementioned into account, it is possible to derive the proton momentum distribution f_p (Chapter 5) in the starburst region if the proton injection rate Q_p (Chapter 4) due to starburst activity is known. Both are related via the simplified transport equation as

$$\frac{f_p(p)}{\tau_{life}} = Q_p(p), \quad (3.1)$$

where p is the momentum of the proton and $\tau_{life}^{-1} \equiv \tau_{gwind}^{-1} + \tau_{diff}^{-1} + \tau_{loss}^{-1}$ is the total lifetime in the compact starburst region with τ_{gwind} the timescale at which particles are advected by galactic-scale outflows, τ_{diff} the timescale over which particles diffuse from the starburst region, and τ_{loss} the timescale for catastrophic energy losses such as pion production. The units of the injection rate $Q_p(p)$ in this work are $[(\text{GeV}/c)^{-3} \text{ cm}^{-3} \text{ s}^{-1}]$ such that $f_p(p)$ has units $[(\text{GeV}/c)^{-3} \text{ cm}^{-3}]$. The derivation of the simplified transport equation, analytic expressions for the timescales, and the relevance of these processes in different regions are discussed in more detail in Chapter 5.

The function $f_p(p)$ represents the energy budget available for pion production and is therefore directly related to the pion production $q_\pi(E)$ with units $[\text{GeV}^{-1} \text{ cm}^{-3} \text{ s}^{-1}]$. Once $q_\pi(E)$ is known, the neutrino production rate $q_{\nu+\bar{\nu}}(E) \equiv q_\nu(E)$ can be determined via the appropriate analytic expressions for the pion-to-neutrino decay channels. Finally the neutrino production rate $q_\nu(E)$ allows to predict the total neutrino flux expected at Earth as

$$F_\nu(E) = \frac{q_\nu(E)V_{SBR}}{4\pi D_L^2}, \quad (3.2)$$

with units $[\text{GeV}^{-1} \text{ cm}^{-2} \text{ s}^{-1}]$ or the single-flavor neutrino flux by dividing Equation 3.2 by a factor three (see Section 6.2). D_L is the luminosity distance and V_{SBR} the volume of the compact starburst

region in the studied U/LIRG. The exact relation between the momentum distribution function, the neutrino production rate, and eventually the neutrino flux for single sources is discussed in detail in Chapter 6. The neutrino-production framework constructed within this work will be applied to Arp 299 in Section 6.5 in order to obtain novel results on its expected neutrino flux. However, the framework is general and as such can be applied to all sources within the GOALS sample once data is acquired for the relevant electromagnetic observables. As such this work presents the foundation for future studies on the cumulative contribution of the GOALS sample to the observed IceCube neutrino flux.

Chapter 4

The proton injection rate

The proton injection rate (Q_p) which will be used for further computations in this work has been discussed in the literature, e.g. [61, 62, 63]. However, instead of simply quoting Q_p , first the evolutionary endpoints of stars and the related impact on the surrounding medium is discussed in Section 4.1. Subsequently the basics of shock theory are discussed in Section 4.2 in order to describe the shock structure in supernova remnants in Section 4.3 and to derive the first order Fermi acceleration mechanism in Section 4.4. The derived differential energy distribution dN/dE related to first order Fermi acceleration will allow to naturally introduce the injection rate $Q_p(p)$ in Section 4.5. Finally in Section 4.6 the output of the code developed within this thesis which allows to compute the proton injection rate, based on the analytic expressions derived in this chapter, is presented and discussed.

4.1 Endpoints in stellar evolution

Most of its life, a star converts hydrogen into helium which results in an outward pressure countering the inward gravitational pressure. Once all hydrogen is converted into helium, the outward pressure stops and subsequently the stellar core starts contracting under the now unbalanced gravitational force. The core contraction results in increasingly higher temperatures until helium fusion is initiated. This stops the contraction and the balance holds until nearly all helium is converted into carbon. What happens afterwards depends on the initial mass of the star. The different fates are now discussed in order of increasing initial stellar mass. This section is mainly based on [64].

4.1.1 Thermonuclear supernovae

A low-mass star of $\lesssim 8M_\odot$ has insufficient mass to generate the core temperatures required to start fusion of carbon. Therefore the core contracts without ignition of carbon which forces the electrons in the core into the smallest possible space they can occupy. According to the Pauli exclusion principle only one fermion can occupy a certain quantum state. In the core the density has become so large that electrons fill up all available quantum states. The pressure related to this state is called the electron degeneracy pressure, which eventually stops gravity from compressing the core further. Upon settling in this equilibrium the star sheds its outer layers and forms a planetary nebula. The core left behind is known as a white dwarf.

A white dwarf in a binary system can accumulate mass from a companion which increases the central density and at a certain stage thermonuclear ignition of carbon may occur. This is all happening under degenerate conditions without the thermostatic effect of a classical equation of state. For a classical equation of state an increase in temperature is related to an increase in pressure which subsequently results in an expansion of the star. This expansion lowers the temperature and finally the nuclear-interaction rate as well. However, the white-dwarf structure existing under degenerate conditions is insensitive to the temperature increase. Therefore a positive-feedback loop is initiated that increases the nuclear-interaction rates more and more. This eventually ends up in a thermonuclear runaway reaction blowing up the whole star. Such an event is typically referred to as a thermonuclear SN. It is believed that such an event leaves no stellar remnant.

4.1.2 Core-collapse supernovae

For high mass stars of $\gtrsim 8M_{\odot}$, the cycle of core contraction and shell burning will continue through neon, oxygen, and silicon with each phase shorter than the previous one. Finally, elements in the iron group are reached with an atomic mass number around $A = 56$. From this point onwards, it is impossible to gain energy from fusion since such elements have the highest binding energy per nucleon and must therefore absorb energy to fuse into heavier elements. In this case the iron core will contract without any subsequent fusion, no matter how massive the star. The contraction of the iron core causes the temperature to increase significantly, allowing for high-energy photons to be produced. Interaction between such gamma rays and atomic nuclei causes them to split and form lighter elements. In this splitting a neutron, proton, or alpha particle is emitted in the process. As the iron core is still contracting while this so-called photodisintegration takes place, the protons will fuse with ambient electrons to form even more neutrons. This electron-proton fusion releases vast quantities of neutrinos which carry away substantial amounts of energy from the central region, again causing the core to cool and contract even further. Such neutrinos have been observed from the SN event *SN 1987A* in the Large Magellanic Cloud. It is noted that these are not the astrophysical neutrinos of interest in this thesis, as discussed in Section 2.1.

The contraction of the core is finally halted once the density exceeds the nuclear density, i.e. the density at which neutrons and protons are packed together inside atomic nuclei. It is extremely difficult to compress matter beyond this point of nuclear density as the strong nuclear force becomes repulsive. Therefore, since the innermost parts of the collapsing core exceed this density, the core contraction slows down and ultimately halts. This creates an outgoing shock wave, discussed in detail in Section 4.2, which reverses the infalling motion of the material in the star, i.e. the stellar envelope, and accelerates it outwards. This shock wave is rather quickly stalled by the inward ram pressure of the infalling matter. A fraction of the numerous produced neutrinos in the core at that point are hypothesised to get trapped behind the shock wave where they will interact and deposit energy. Such interactions increase the pressure and temperature behind the shock wave, thereby giving it extra momentum to keep on travelling outwards [65]. The passage of the shock wave compresses and heats the material (Section 4.2) in the star to such a degree that a whole new wave of nucleosynthesis occurs. These reactions produce elements beyond iron, which the star was not able to produce over its lifetime. Moreover, heating by the shock wave ignites exothermal thermonuclear reactions resulting in a detonation wave that, in addition to the neutrino energy deposition, also adds momentum to the existing shock wave making its way to the surface. Once the shock wave reaches the surface, the whole stellar envelope has been set in motion and the star is blowing apart. The stellar layers, with amplified magnetic fields and significantly enhanced heavy-element concentrations due to the progenitor fusion and shock propagation, are launched into the surrounding interstellar medium (ISM) with speeds of $\sim 10^4$ km/s. These are speeds much larger

than expected for the speed of sound in the ambient ISM medium. Typically if an object moves at a speed larger than the speed of sound in that medium, a so-called shock front will be formed (Section 4.2). It is noted that the ISM into which the SN ejecta (= ejected stellar layers) propagate is not necessarily a gas of uniform density but can as well be the stellar mass ejected by the pre-supernova star (= progenitor) during late stages of stellar evolution.

Such highly energetic SN events, which outshine entire galaxies with a typical energy of $E_{SN} = 10^{51}$ erg, are known as core-collapse SN events. Part of this energy output is converted to particle energy via first order Fermi acceleration along the shock front driven by the supersonic ejecta. This acceleration mechanism, under the appropriate environmental circumstances, is hypothesised to be able to accelerate CRs to energies as large as ~ 100 PeV [61]. Before studying first order Fermi acceleration, the shock theory basics are derived and discussed in Section 4.2.

A star's main-sequence lifetime (t) is proportional to its mass (M) divided by its luminosity (L), i.e. $t \propto M/L$, and a star's luminosity is proportional to its mass following a power-law relation given by $L \propto M^{3.5}$ and therefore $t \propto M^{-2.5}$. From this it is clear that in an U/LIRG the enhancement of supernova activity is not due to the low-mass stars discussed in Section 4.1.1, but dominated by the high-mass star explosions discussed in this section.

Hypernovae The most massive stars are believed to end their life in extreme forms of core-collapse SN explosions, i.e. hypernovae. In this case a massive star exceeding $\sim 30 M_{\odot}$ collapses instantaneously to a rotating black hole emitting twin energetic jets perpendicular to an accretion disk formed from the recently ejected stellar material. Such events have an energy output which is an order of magnitude larger than most SN, i.e. $E_{HN} = 10^{52}$ erg. Hypernovae are likely related to long gamma-ray bursts, which on their turn form an interesting class of neutrino source candidates. The study of gamma-ray bursts as neutrino sources lies beyond the scope of this work. However, the hypernovae will be revisited in this work in Section 4.5.3 when discussing the maximum momentum reached in SN-related acceleration processes.

4.2 Shock formation

Shock fronts are abundantly present in various astrophysical environments, such as starburst regions of U/LIRGs due to the increased core-collapse supernova activity. Some structures of astrophysical shocks are shown in Figure 4.1 which can be identified by the bow structure with a thin slice of bright colour. Shocks are of particular interest in this work as they allow for efficient particle acceleration which in turn can lead to high-energy neutrino production. The basics of shock theory relevant for further discussions are discussed in what follows. This section and Section 4.3 are mainly based on [64] and [66].

4.2.1 Basic shock theory

A first step towards describing shock formation is discussing the concept of sound waves. Such a wave is a type of energy propagation in a medium by means of adiabatic compression and decompression, i.e. an acoustic wave. Essentially a sound wave is the propagation of a pressure perturbation and the speed at which it travels is called the speed of sound (c_s).

The speed of sound in a medium sets the time scale over which different parts of that medium can communicate. In a region of size L the gas will respond to sudden changes on a time scale L/c_s . When an object moves through a medium with a speed exceeding c_s , i.e. the object is supersonic, the gas being hit by the object will not be able to communicate to other parts of the medium

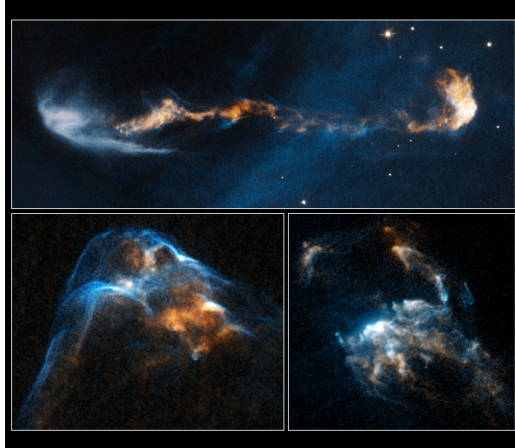


Figure 4.1: Examples of shocks in astrophysical environments. These are NASA/ESA Hubble Space Telescope images [67].

that the object is approaching. This means that there must be a discontinuity between the swept up gas co-moving with the object and the gas that has yet to be affected by this motion. Such a discontinuity is called a shock wave/front.

Studying a one-dimensional shock, which for now can be imagined as driven by a piston in a long gas-filled tube, allows to highlight properties of shock fronts which will be directly relevant for the study of shocks induced by SN ejecta. The setup for the derivations that will follow is shown in Figure 4.2 where the light shade corresponds to the unshocked region, referred to as upstream, while the dark shade refers to the downstream shocked gas. This is shown for the reference frame of the shock (Figure 4.2 right) and the lab frame (Figure 4.2 left). Even without knowing anything about the transition region between the unperturbed upstream gas and the shocked downstream gas, it is still possible to derive how the field variables must transit between the two regions. This is done by imposing mass, momentum, and energy conservation when passing the shock front in the reference frame of the shock. This results in three equations known as the Rankine–Hugoniot jump conditions.

1. *Conservation of mass:* ρv is the mass flux passing through the discontinuity, which must be conserved going from the upstream to the downstream. It is noted that the assumption is made that the front is infinitesimally thin such that there is no mass accumulation. This results in

$$\rho_1 v_1 = \rho_2 v_2 \equiv J. \quad (4.1)$$

2. *Conservation of momentum:* Pressure is a force per unit area, i.e. a momentum flux. On the one hand there is the kinetic pressure due to the random motions of the particles P . On the other hand there is additional momentum in the bulk motion of the gas on each side of the shock, which has momentum density flux ρv and therefore momentum flux ρv^2 . This flux is better known as the ram pressure. The main difference between ram pressure and kinetic pressure is that the former is (highly) directional while the latter is isotropic. Therefore conservation of momentum is expressed as

4.2. SHOCK FORMATION

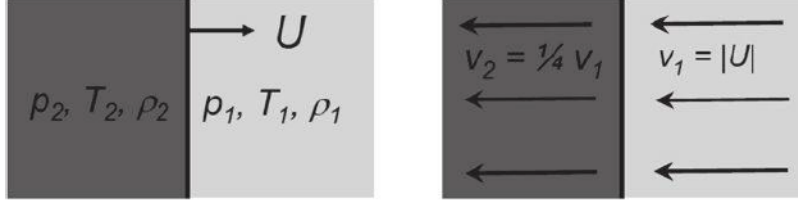


Figure 4.2: Representation of a shock approximated as a plane wave. The light shade corresponds to the upstream gas with field variables P_1, ρ_1 , and T_1 while the dark grey shade represents the downstream gas with P_2, ρ_2 , and T_2 . The downstream gas is often referred to as the 'shocked gas'. (Left) Shock propagating through the interstellar medium at speed U . (Right) In the reference frame of the shock, the interstellar medium approaches the shock and the shocked medium moves away from it [66].

$$\rho_1 v_1^2 + P_1 = \rho_2 v_2^2 + P_2 \equiv I. \quad (4.2)$$

3. *Conservation of energy:* Gas on either side of the shock has kinetic energy density $\rho v^2/2$ and thermal energy density $\rho \epsilon$ with $\epsilon(P, \rho, T)$ the thermal energy per unit mass. Summing these, and multiplying with v , yields the energy flux $v(\rho v^2/2 + \rho \epsilon)$. In addition, when passing the shock boundary, some of the energy flux will go into work due to compression of the gas. The energy flux in this component is Pv . Summing the contributions and imposing energy conservation then results in

$$\rho_1 v_1 \left(\frac{v_1^2}{2} + \epsilon_1 \right) + P_1 v_1 = \rho_2 v_2 \left(\frac{v_2^2}{2} + \epsilon_2 \right) + P_2 v_2, \quad (4.3)$$

and dividing this by Equation 4.2 together with the assumption that the flow along the shock is adiabatic, i.e. $\epsilon = \frac{3P}{2\rho}$, it follows that

$$\frac{v_1^2}{2} + \frac{5P_1}{2\rho_1} = \frac{v_2^2}{2} + \frac{5P_2}{2\rho_2}. \quad (4.4)$$

In order to derive the results of interest, Equation 4.2 is divided by Equation 4.1 $\times v$ and the speed of sound for an adiabatic flow $c_{s,adb}^2 = \frac{5P}{3\rho}$ is used such that,

$$\frac{I}{Jv} = \frac{P}{\rho v^2} + 1 = \frac{3}{5\mathcal{M}^2} + 1, \quad (4.5)$$

with $\mathcal{M}^2 = v^2/c_s^2$ the so-called Mach number. Using this result in Equation 4.4 allows to write it as a quadratic equation in v which happens to have a positive discriminant. The two roots correspond to the velocities v_1 and v_2 and summing them results in

$$1 + \frac{v_2}{v_1} = \frac{5}{4} \left[\frac{3}{5\mathcal{M}_1^2} + 1 \right]. \quad (4.6)$$

The result is expressed in terms of the upstream Mach number \mathcal{M}_1 . The reader is reminded that the derivation here is done in the reference frame of the shock. In the lab frame it is the shock which is moving with Mach number \mathcal{M}_1 .

In this work strong shocks are of particular interest and are defined as $\mathcal{M}_1 \gg 1$. Shock fronts driven by the ejecta for SN, propagating at ~ 10000 km/s can therefore be regarded as strong shocks. Now assuming a strong shock in Equation 4.6 then results in

$$1 + \frac{v_2}{v_1} = \frac{5}{4} \quad (4.7)$$

$$\iff v_2 = \frac{v_1}{4} \quad (4.8)$$

$$\stackrel{\text{Eq 4.1}}{\iff} \rho_2 = 4\rho_1. \quad (4.9)$$

From this it can be concluded that by going from the upstream to the downstream region, the velocity has dropped while the density has been increased. Moreover, no matter how strong a shock is, it can compress a mono-atomic gas only by a factor four.

Substituting Equation 4.2 in Equation 4.5 and applying the strong shock results in

$$I = \rho_1 v_1^2 \left[\frac{3}{5\mathcal{M}_1^2} + 1 \right] \approx \rho_1 v_1^2, \quad (4.10)$$

which is the expression for ram pressure as discussed earlier. For strong shocks, the thermal pressure is negligible with respect to the ram pressure in the upstream region such that $P_1 \ll \rho_1 v_1^2$. Applying this to Equation 4.2 gives

$$P_2 = P_1 + \rho_1 v_1^2 - \rho_2 v_2^2 \approx \rho_1 v_1^2 - \rho_2 v_2^2 = \rho_1 v_1 (v_1 - v_2) \stackrel{\text{Eq 4.8}}{\iff} P_2 \approx \frac{3}{4} \rho_1 v_1^2. \quad (4.11)$$

This result reflects that when passing the shock from upstream to downstream 75% of the ram pressure is being converted into random thermal motion. In other words, passing the shock therefore significantly heats the upstream gas. This result will be of particular interest when discussing the galactic-scale outflows typically observed in starburst galaxies (Section 5.2.2).

In Section 4.1 it was mentioned that the shock wave propagating through the stellar envelope compresses and heats the material on its way. This can now be understood from Equation 4.9 and Equation 4.11. Moreover it was mentioned that this same shock sets the stellar envelope in motion as it passes through. This is shown in Equation 4.8, from which it can be concluded that in the lab frame the shocked front follows the shock wave with a velocity 3/4 times that of the shock itself.

4.3 Shock structure and evolution of supernova remnants

Once the stellar envelope is ejected by the SN explosion, the ejecta will propagate spherically outwards at a supersonic speed through the surrounding ISM. Every small region of this spherical shock front can be viewed as a one-dimensional shock, with the ejecta playing the role of the constant-velocity piston considered so far. The shock wave driven by the SN ejecta is also referred to as the forward shock wave or the blast wave. The main source of particle acceleration in a SN remnant is due to this particular shock. Shortly after the SN explosion, the SN remnant is in the *free expansion phase*. The ejecta swipe up the surrounding ambient ISM gas at a constant supersonic velocity, thereby compressing and heating it. The boundary between this swept-up shocked ISM gas and the ejected stellar mass driving the shock is called the contact discontinuity, i.e. a surface between two different materials with similar pressure and velocity but different density. No particle transport is taking place along this contact discontinuity. The swept-up shocked gas pushes

back on the SN ejecta and eventually results in another shock wave, the so-called reverse shock, which propagates towards the progenitor. This shock heats the ejected stellar gas to high temperatures which results in significant X-ray emission. At the time the reverse shock has propagated through all of the ejecta, approximately the same amount of ambient matter has been swept up by the forward shock. By definition this also the end of the free-expansion phase. Figure 4.3 shows a self-made graphical representation of the various shocks and (un)shocked gas in the SN remnant.

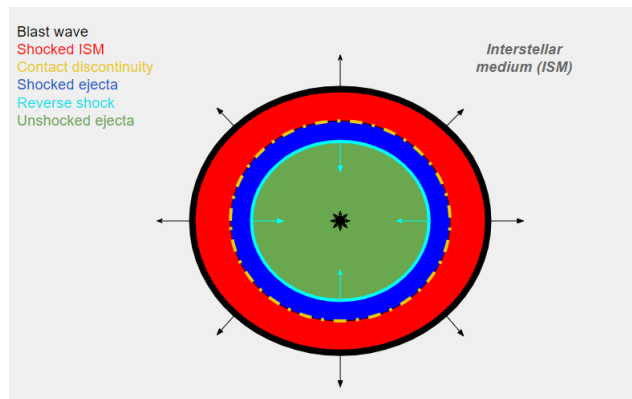


Figure 4.3: The shock structure in a SN remnant. Working inwards, first the SN blast wave (black) expanding into the unperturbed ISM is encountered. Once this ISM gas passes the shock it will be compressed and heated, indicated by the red band. The SN ejecta, acting as a piston driving the blast wave, are separated from the shocked ISM gas by the contact discontinuity indicated by the yellow dash-dotted line. No particle transport takes place along the contact discontinuity. The inwards propagating reverse shock indicated in cyan will heat, compress, and slow the SN ejecta as it propagates through. The shocked and unshocked ejecta are indicated by the blue and green band, respectively.

After the passage of the reverse shock the interior of the SN remnant is so hot that practically all atoms are ionized and there is no recombination. The energy losses by radiation are thus very small, which results in a pressure-driven expansion phase that can be regarded as adiabatic. From this point on the ejecta do not serve as a working piston anymore and the blast wave stops expanding at a constant velocity. This is the start of the so-called *Sedov-Taylor phase*. A related quantity to the Sedov-Taylor phase is the Sedov-Taylor radius. This radius is defined as the distance between the neutron star at the center of the remnant and the location of the blast wave at the onset of the Sedov-Taylor phase. For further discussion it must be noted that at the start of the Sedov-Taylor phase the hadrons accelerated along the blast wave reach their maximum energy (Section 4.5.3).

Due to the adiabatic cooling of the SN remnant, a critical temperature $\sim 10^6$ K will be reached where ionized atoms start capturing free electrons. At this point radiative cooling starts to become significant which also marks the end of the adiabatic expansion. Moreover, as a result of the radiative cooling, the pressure in the post-shock regions decreases which slows down the expansion. When this happens the SN remnant is entering the *snow-plough phase* since more and more interstellar gas is accumulated. This goes on until the swept-up mass is much larger than the initial ejected stellar material. Finally the shell breaks up into individual clumps.

4.4 First order Fermi acceleration

In this section the principle of first order Fermi acceleration is derived, which is the last step required to introduce the proton injection rate. This section is mainly based on [64], [66], and [68].

Imagine a relativistic charged particle with energy E_1 in the reference frame of the upstream plasma, i.e. a gas of ions, as in Figure 4.4 (a). This particle will drift along the direction of the magnetic field while circling perpendicular to it in a helical trajectory characterized by the so-called Larmor radius. On top of this ordered magnetic field in the plasma, the regions in and near shocks are thought to have randomly oriented magnetic-field fluctuations. It can be shown that in a plasma with infinite conductivity (as is an appropriate approximation for plasmas) any movement of the plasma will be followed by the magnetic field, as if it were frozen into it [66]. The magnetic-field fluctuations are therefore stationary in the rest frame of the plasma. Upon interaction between the charged particle and the fluctuation, the particle will be deflected into a new trajectory until a different fluctuation is encountered. Due to the abundant scattering on the magnetic field fluctuations, the particle's velocity vector is randomized. Finally, as a result of the random walk on the magnetic instabilities, the particle will cross the shock front to the downstream region. The particle in the downstream plasma will again scatter on the magnetic instabilities there, randomising the velocity vector and eventually recrossing the shock back to the upstream region. It is noted that not all particles will re-cross the shock but for now the focus is on those who do. It can be shown, as in done in Appendix A, that the average energy gain after one cycle, meaning crossing the front back and forth, is

$$\left\langle \frac{\Delta E}{E} \right\rangle_{cycle} = \frac{4}{3} \frac{V_p}{c} = \frac{V}{c} \quad (\text{one cycle}). \quad (4.12)$$

The name first order Fermi acceleration refers to the fact that the increase in energy goes as $\Delta E/E \propto V/c$, in contrast to second order Fermi acceleration, where $\Delta E/E \propto (V/c)^2$ [66].

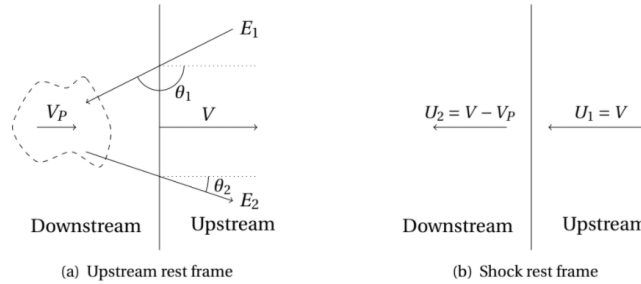


Figure 4.4: Interaction of a particle with the shock, seen from the upstream rest frame (a) and velocities of the upstream and downstream region in the shock rest frame (b). Here U_1 (U_2) is the velocity of the upstream (downstream) plasma in the shock rest frame. Moreover, V_p and V are respectively the velocity of the downstream plasma and the velocity of the shock in the frame where the upstream plasma is at rest [68]

As was mentioned above, not all particles crossing to the downstream region will make their way back to the upstream. If this happens the particle leaves the acceleration region and will not gain energy anymore. The probability of a particle leaving the acceleration region is the ratio of the flux of particles being swept away downstream R_{out} to the flux of particles that initially

passed the shock to the downstream R_{in} . The flux of particles crossing the shock from upstream to downstream is found by projecting the isotropic accelerated particle flux onto the plane of the shock front and then integrating for all particles going towards the shock, resulting in $R_{in} = c\rho/4$, with ρ the density of cosmic-ray particles undergoing acceleration. A fraction of this flux, moving from upstream to downstream, will be swept away due to convection. This corresponds to the flux of particles that leave the system R_{out} . The rate of convection downstream is given by $U_2\rho$, with $U_2 = V/4$ (Equation 4.8). Therefore, the fraction of particles that is lost is $\frac{\rho V}{4} / \frac{\rho c}{4} = V/c$. As such the probability that a particle leaves the system after each cycle is,

$$P_{esc} = \frac{R_{out}}{R_{in}} = 1 - P_{stay} \iff P_{stay} = 1 - \frac{V}{c}. \quad (4.13)$$

Now that the fractional energy gain per round trip and probability for a particle to stay in the acceleration region is determined, it is possible to derive the differential energy distribution dN/dE related to first order Fermi acceleration.

First a particle with initial energy E_0 is considered and δ is chosen as the fractional energy gain after one interaction, which is defined for crossing the shock back and forth. Then after k interactions the particle will have an energy of $E = E_0\delta^k$. The probability that the particle stays in the acceleration region after one round is denoted as P_{stay} . Therefore, starting with N_0 particles, there will be $N = N_0P_{stay}^k$ left after k interactions. The number of collisions can now be eliminated by first applying the natural logarithm to $E_0\delta^k$ and $N_0P_{stay}^k$. Then solving each of these equations for k and equating them results in

$$\frac{\ln(N/N_0)}{\ln(E/E_0)} = \frac{\ln(P_{stay})}{\ln(\delta)} \iff \frac{N}{N_0} = \left(\frac{E}{E_0}\right)^{\ln(P_{stay})/\ln(\delta)}. \quad (4.14)$$

The differential energy spectrum as a result of the first order Fermi acceleration is therefore

$$\frac{dN(E)}{dE} = \text{constant} \times E^{-1 + [\ln(P_{stay})/\ln(\delta)]}. \quad (4.15)$$

The only thing left to determine is then $\ln(P_{stay})/\ln(\delta)$. Based on Equation 4.12 and Equation 4.13 it follows that

$$\ln(\delta) = \ln\left(1 + \frac{V}{c}\right) \simeq \frac{V}{c} \quad \text{and} \quad \ln(P_{stay}) = \ln\left(1 - \frac{V}{c}\right) \simeq -\frac{V}{c}, \quad (4.16)$$

where in both cases a Taylor expansion was performed to achieve the final result, which is justified because the shock is non-relativistic. Combining these in a fraction then results in

$$\frac{\ln(P_{stay})}{\ln(\delta)} \simeq -1. \quad (4.17)$$

Plugging this into Equation 4.15 finally gives the differential particle energy distribution

$$\frac{dN(E)}{dE} \propto E^{-2}. \quad (4.18)$$

It can be concluded that first order Fermi acceleration naturally produces a power-law spectrum with index 2. To see why this is a very interesting result, a small intermezzo is added describing the cosmic-ray flux observed on Earth.

Intermezzo on the observed CR spectrum The observed CR spectrum spans many orders of magnitude in energy and flux, from 1 particle per m^2 per second at 10^9 eV to 1 particle per km^2 per century at 10^{20} eV. The observed spectrum follows a near-perfect power law $dN/dE \propto E^{-\alpha}$ across the entire energy range, as shown in Figure 4.5, with small breaks where the spectral index changes slightly. The spectrum up to $\sim 10^{15}$ eV - 10^{16} eV is described by $\alpha \simeq 2.7$ after which the first break happens, referred to as *the knee*, and the spectrum steepens. From the knee up to 4×10^{17} eV, referred to as *the second knee*, the spectral index is $\alpha \simeq 3$. After the second knee the spectrum steepens again to $\alpha \simeq 3.2$ up to the so-called *ankle* at $10^{18.5}$ eV. From the ankle up to the maximal observed energy around $10^{20.5}$ eV, the spectral index is $\alpha \simeq 2.6$. The knee, second knee, and ankle structures are shown in Figure 4.5.

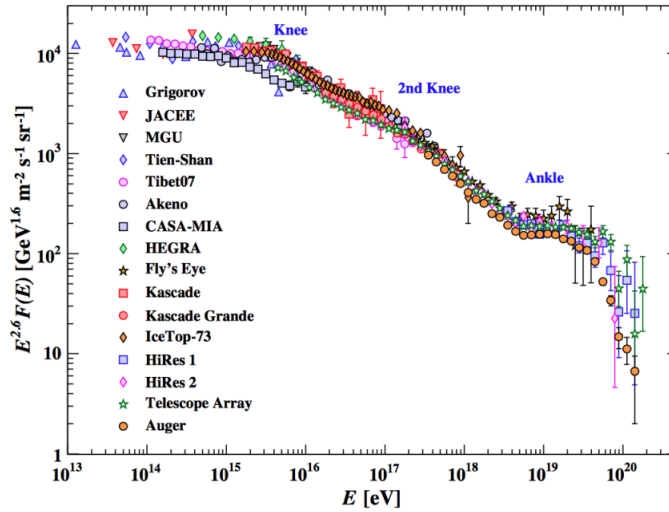


Figure 4.5: Observed CR energy spectrum obtained with data from several observatories. The lower end of the energy spectrum (10^{16} - 10^{17} eV) is believed to originate from sources within the Milky Way. All energies exceeding the ankle (3×10^{18} eV) are most likely of extragalactic nature. The transition region is a matter of active debate [24].

The changes in steepness of the spectrum are still a matter of active research but it is suggested that different acceleration mechanisms give rise to the different observed spectral indices. CRs with energies up to the knee are generally accepted to be of galactic nature and more specifically from galactic SN remnants. This claim seems to contradict the result from Equation 4.18, as the observed spectrum on Earth is steeper by an amount of ~ 0.7 . So-called leaky box models are able to attribute this extra factor to diffusion effects of cosmic rays propagating in the Milky Way [69]. Essentially the idea is that particles with higher energies have a larger probability to escape the galactic magnetic field and will therefore reach Earth less frequently.

The transition region between the second knee and the ankle is still under debate and is at the time of writing the most inconclusive. All CRs with energies exceeding the ankle cannot be contained anymore by the magnetic field of the Milky Way and hence their sources are most likely of extragalactic origin. Gamma-ray bursts, young pulsars, and active galactic nuclei are for example proposed as possible extragalactic hadronic accelerators.

Having introduced all the concepts and terminology so far, the construction of the neutrino production framework can start. A first step in doing this is the discussion of the proton injection rate in Section 4.5. As mentioned previously, the concept of the proton injection rate can be found in the literature, e.g. [61, 62, 63]. The novel aspect in this work is the discussion of the proton injection rate in context of GOALS U/LIRGs, where relevant the connection will be made with Chapter 3 to highlight the electromagnetic observables important to the framework. Moreover, explicit computations will be done to determine the proton injection rate which will be compared to existing predictions.

4.5 The proton injection rate Q_p

The main result of the previous section is that the presence of strong shocks in astrophysical plasmas can lead to efficient particle acceleration via first order Fermi acceleration. This acceleration mechanism gives rise to a power-law differential energy distribution of accelerated particles which is in good agreement with observations on Earth. As the focus of this work lies on starburst-driven U/LIRGs, where shocks are abundantly present, it is therefore justified to adopt a power law expression for the proton injection rate $Q_p(p)$. In addition an exponential cutoff for this injection is considered at the maximum achievable momentum p_{max} during acceleration. The injection rate of particles in a specific starburst region can therefore be expressed as

$$Q_p(p) = \frac{1}{V_{SBR}(R_{SBR})} \sum_i \mathcal{N}_i(p) = \frac{1}{V_{SBR}(R_{SBR})} \sum_i N_{C,i} \left[\frac{p}{m_p c} \right]^{-\alpha_i} e^{\frac{-p}{p_{max,i}}}. \quad (4.19)$$

The factor α_i is the power-law exponent which depends on the physics of the considered shock system, $N_{C,i}$ is the proportionality constant fixed by electromagnetic data (Section 4.5.1), m_p the mass of the proton, and V_{SBR} the volume of the considered starburst region which directly depends on the radius of the energetic region R_{SBR} . $Q_p(p)$ is given as a sum over distinct types of shock environments in the considered starburst region.

Supernova injection rate In this work the focus is on particle acceleration along the forward shock in SN remnants (Section 4.3), i.e. $i = SN$ in Equation 4.19. The cumulative contribution of all SN activity in the starburst region to the proton injection rate is expressed as

$$Q_{p,SN}(p) = \frac{\mathcal{N}_{SN}(p)}{V_{SBR}} = \frac{N_{C,SN}}{V_{SBR}} \left[\frac{p}{m_p c} \right]^{-\alpha_{SN}} e^{\frac{-p}{p_{max,SN}}}. \quad (4.20)$$

The volume of the starburst region in this work is considered to be spherical. However, it is noted that for some galaxies a cylindrical volume might be more appropriate.

Stellar-wind injection rate In Section 3.1 we discussed that high-mass stars suffer large mass losses via high-velocity stellar winds, especially during the Wolf-Rayet phase. Upon interaction between these supersonic ejecta and the surrounding medium, shock waves are expected to be formed which also lead to first order Fermi acceleration. Therefore one could add the expression,

$$Q_{p,SW} = \frac{\mathcal{N}_{SW}(p)}{V_{SBR}} = \frac{N_{C,SW}}{V_{SBR}} \left[\frac{p}{m_p c} \right]^{-\alpha_{SW}} e^{\frac{-p}{p_{max,SW}}}, \quad (4.21)$$

to the sum in Equation 4.19. $Q_{p,SW}$ is interpreted as the total proton injection rate due to stellar-wind accelerated particles. The kinetic energy of stellar-wind ejecta is much lower as opposed to SN ejecta but these stellar winds occur more frequently. Nevertheless, it is found that the contribution of particle acceleration due to stellar winds is in general sub-dominant as opposed to particle acceleration in SN remnants. For the Milky Way it is estimated that that the relative contribution of stellar-wind accelerated particles to SN accelerated particles is only 1/4 [70]. In [62] it was concluded that for Arp 220 this relative contribution is between 0.43 and 0.87, depending on the initial mass function of the galaxy, while for NGC 253 and M82 ~ 0.30 was found. This increased relative contribution for Arp 220 is directly related to the extreme star-formation properties of ULIRGs. No explicit calculations containing $Q_{p,SW}$ will be done in what follows since fixing the normalisation constant $N_{C,SW}$ is more involved as opposed to fixing $N_{C,SN}$ (Section 4.5.1). Nevertheless, the fact that the GOALS sample consists of U/LIRGs, which have extreme star-formation rates and therefore abundant stellar winds, could motivate future studies to take this contribution into account.

In principle, any other shock system leading to first order Fermi acceleration, apart from SN and stellar-wind related activity, could be added to the sum in Equation 4.19. One interesting candidate could be the contribution of shocks forming upon interaction between ejected material from young, rapidly spinning neutron stars, i.e. pulsars, and the ejecta of the progenitor [71].

The expression in Equation 4.19 is valid for a particular starburst region in the considered U/LIRG. However, the discussion in Section 3.3.3 showed that there is a wide variety of LIRG morphologies, including minor/major merging galaxies. Such interacting systems can have a significant separation between the different nuclear regions and as such distinct stellar and/or AGN activity, e.g. Arp 299 (Section 3.3.5). In that case it is more appropriate to consider the regions separately if the available data is at hand. Therefore an injection rate for the whole galaxy $Q_{galaxy}(p)$ is defined in this work as,

$$Q_{galaxy}(p) = \sum_k \frac{1}{V_{SBR}^k} \sum_i N_{C,i}^k \left[\frac{p}{m_p c} \right]^{-\alpha_i^k} e^{\frac{-p}{p_{max,i}^k}}, \quad (4.22)$$

with the sum over the distinct energetically dominant regions which are identified as relevant neutrino production regions. The volume parameter V_{SBR} now has an index, as the different energetically dominant regions likely have different spatial dimensions. Nevertheless, this approach requires interferometric radio and IR observations with significant resolution in order to resolve nuclear regions within that galaxy. This becomes more challenging with increasing source distance to Earth.

In order to clarify the notation in Equation 4.22, Arp 299 (Section 3.3.5) is used as example. If one would like to determine the injection rate of accelerated protons due to the collective SN activity in the nuclear regions of Arp 299 (Figure 3.7), this would be

$$Q_{Galaxy,SN}(p) = \frac{1}{V_{SBR}^A} N_{C,SN}^A \left[\frac{p}{m_p c} \right]^{-\alpha_{SN}^A} e^{\frac{-p}{p_{max,SN}^A}} + \frac{1}{V_{SBR}^B} N_{C,SN}^B \left[\frac{p}{m_p c} \right]^{-\alpha_{SN}^B} e^{\frac{-p}{p_{max,SN}^B}}. \quad (4.23)$$

For the sake of simplicity, in the rest of this work the neutrino-production framework will be expressed for one particular starburst region.

4.5.1 Fixing the normalisation constant

The normalisation constant of the injection rate $N_{C,i}$ is fixed with respect to electromagnetic data acquired by surveys monitoring U/LIRGs, such as GOALS. The exact expression of $N_{C,SN}$ is a crucial part of the code that will be developed in Section 4.6 which allows to compute the proton injection rate, which is on its turn required to compute the starburst-driven neutrino flux in Chapter 6. Therefore the fixing procedure of the normalisation constant is now explicitly derived.

Multiplying the SN rate with the characteristic energy output of a SN event, $E_{SN} = 10^{51}$ erg, allows to calculate the amount of energy ejected per unit time by all the SN explosions in the studied starburst region. Part of this energy output is converted to particle energy via shock acceleration. For a single SN event this energy conversion is described by the efficiency factor ξ_{CR} , typically chosen to be $\sim 10\%$ [72]. Taking ξ_{CR} into account then allows to determine the collective energy injection in terms of SN-accelerated particles per unit time in the compact starburst region as,

$$\mathcal{L}_{CR} = \xi_{CR} \mathcal{L}_{SN} = \xi_{CR} \mathcal{R}_{SN} E_{SN} \quad [\text{GeV yr}^{-1}]. \quad (4.24)$$

Given the spherical shock geometry in SN remnants (Figure 4.3), the interpretation of $\mathcal{N}_p(p)$ as a density of states in momentum space per unit time $[(\text{GeV}/c)^{-3} \text{s}^{-1}]$, and $\mathcal{T}(p)$ as the particle kinetic energy allows to write,

$$d\mathcal{L}_{CR} = 4\pi p^2 \mathcal{N}_{SN}(p) \mathcal{T}(p) dp, \quad (4.25)$$

which essentially reflects the amount of kinetic energy in the range E and $E + dE$. Integrating this over the whole momentum range then equals the total kinetic energy in SN-accelerated particles per unit time, which is exactly what is determined via electromagnetic observations in Equation 4.24. Equating the expression in Equation 4.24 to Equation 4.25 integrated over the whole momentum range allows to find an expression for $N_{C,SN}$,

$$\begin{aligned} \xi_{CR} \mathcal{R}_{SN} E_{SN} &= \int_0^\infty 4\pi p^2 \mathcal{N}_{SN}(p) \mathcal{T}(p) dp \\ &= \int_0^\infty 4\pi p^2 N_{C,SN} \left(\frac{p}{m_p c} \right)^{-\alpha_{SN}} e^{\frac{-p}{p_{max,SN}}} \mathcal{T}(p) dp \\ &= \int_0^\infty 4\pi p^2 N_{C,SN} \left(\frac{p}{m_p c} \right)^{-\alpha_{SN}} e^{\frac{-p}{p_{max,SN}}} \left(\sqrt{p^2 c^2 + m^2 c^4} - mc^2 \right) dp \\ &= \mathcal{L}_{CR}, \end{aligned} \quad (4.26)$$

such that

$$N_{C,SN} = \frac{\xi_{CR} \mathcal{R}_{SN} E_{SN}}{\int_0^\infty 4\pi p^2 \left(\frac{p}{m_p c} \right)^{-\alpha_{SN}} e^{\frac{-p}{p_{max,SN}}} \cdot \left(\sqrt{p^2 c^2 + m^2 c^4} - mc^2 \right) dp}. \quad (4.27)$$

It can be concluded that in order to fix $N_{C,SN}$ one must first determine the **SN rate** (\mathcal{R}_{SN}) in the nuclear starburst U/LIRG under investigation (Section 4.5.2), the **maximal attainable energy** p_{max} during acceleration (Section 4.5.3), and the corresponding **spectral power-law index** α_{SN} (Section 4.5.4).

4.5.2 The supernova rate in U/LIRGs

In Section 3.3 it was already discussed that direct observations of nuclear regions of U/LIRGs via a combination of high-resolution interferometric radio and IR observations is required to determine the SN rate. In this work only SN rate values obtained from such observations will be used to compute neutrino fluxes. Nevertheless, only a few of the GOALS sources have such dedicated observational data. Future studies computing the cumulative contribution of the whole GOALS sample to the diffuse astrophysical neutrino flux, using the model developed in this work, need a SN rate for every single GOALS source. In that case it is still possible to estimate the SN rate via the initial mass function, i.e. the function describing the mass distribution for a population of stars at formation time, and the star-formation rate in the region of interest. How to estimate the SN rate from these two quantities is discussed in detail in Appendix B. Although a lot of uncertainties are related to this approach, it is for many of the sources in the GOALS sample the only option. Nonetheless, this initial mass function approach is not used for further calculations in this work.

4.5.3 Maximum attainable momentum

One of the required parameters to determine the proton injection rate is p_{max} (Equation 4.19). The maximum attainable momentum reached in acceleration processes depends on the type of cosmic accelerator and the astrophysical environment studied. In this section p_{max} is discussed for SN accelerated protons in starburst U/LIRGs.

As already mentioned in Section 4.4 (Figure 4.5), galactic SN are generally believed to be the dominant source of CR energies up to the knee, i.e. ~ 3 PeV. However, in order to explain the highest PeV neutrino energies (E_ν) observed by IceCube, starburst U/LIRG regions should be able to accelerate protons to $E_p \sim 50$ -100 PeV, given that on average $E_\nu \simeq E_p/20$ in inelastic pp -interactions (Section 2.1).

The p_{max} for SN acceleration is reached around the time that the ejecta start to decelerate, i.e. the start of the Sedov-Taylor phase (Section 4.3). In [61] it is argued that by invoking a particular diffusion model for the starburst region the maximum attainable energy for SN acceleration is

$$E_{max} \approx 30 \left(\frac{R_S}{3 \text{ pc}} \right) \left(\frac{V_{sh}}{10^4 \text{ km/s}} \right) \left(\frac{B}{1 \text{ mG}} \right) \text{ PeV}, \quad (4.28)$$

with R_S the Sedov-Taylor radius, V_{sh} the typical shock speed during the free-expansion phase, and B the magnetic field in the starburst region. The average magnetic field for compact starburst regions is $\gtrsim 100 \mu\text{G}$ and is expected to be even higher for regions such as the nuclei of Arp 220 (Section 3.3.4), where the magnetic field might reach a few mG [73]. In the latter case a maximum CR energy in the 50-100 PeV energy range could be reached [61]. This is interesting for two reasons. First, since the GOALS sample consists of U/LIRGs, at least a subset of the sources is expected to have similar conditions to the nuclei of Arp 220, and therefore comparable magnetic field strengths. Secondly, even if the magnetic fields are not strong enough to push p_{max} to the highest energies of interest, there is still an overall enhancement expected for p_{max} in starburst regions since the average magnetic field is larger than for non-starburst galaxies. In [61] it is concluded that although plausible, it is by no means trivial to reach the 50-100 PeV energy range if one only considers SN particle acceleration.

From Equation 4.28 it is also concluded that the the maximum energy depends on the speed of the ejecta which is in on its turn related to the kinetic energy of the ejecta. Therefore it is interesting to consider a special type of core-collapse SN, i.e. hypernovae (Section 4.1.2). Hypernovae have ejecta with kinetic energies that are an order of magnitude larger ($E_{HN} = 10^{52}$ erg) than normal SN ejecta ($E_{SN} = 10^{51}$ erg). However, hypernovae are expected to be rare in the local Universe while being more numerous at higher redshifts [74]. Since the GOALS sample is located within the local Universe it is not immediately clear if the sample would significantly benefit from a hypernovae contribution. In this work such a possible contribution is not taken into account but it might be an interesting addition for future studies focusing on neutrino production in starburst-driven U/LIRGs at high redshifts. In that case one should first come up with a systematic way to estimate the hypernova rate (\mathcal{R}_{HN}) in a given starburst region. Once this is achieved, it would be possible to determine the hypernova contribution to the proton injection rate Q_p in the same way as was derived in Section 4.5.1 by changing $\mathcal{R}_{SN} \rightarrow \mathcal{R}_{HN}$ and $E_{SN} \rightarrow E_{HN}$ when working through the normalization process.

In conclusion, considering only SN particle acceleration in the GOALS sample it is challenging to explain the highest neutrino energies of the astrophysical IceCube flux. Nevertheless, the average p_{max} in the starburst regions of interest are most likely still higher as opposed to non-starburst galaxies, e.g. the Milky Way, where the maximum energy of SN accelerated CRs is expected to be ~ 3 PeV. Therefore it could be that the GOALS sample only significantly/dominantly contributes to the diffuse IceCube flux up to a given energy while other source classes account for the highest neutrino energies. This is discussed in a more quantitative way in Section 6.4 when discussing the neutrino flux computations for different p_{max} values (Figure 6.6).

4.5.4 Power-law index

The power-law index α_{SN} is the only parameter which has not been discussed in more detail. It is instructive to first derive the proton momentum distribution function and the neutrino-production rate. Therefore a more detailed discussion of the power-law index is postponed to Section 6.3. However it is noted here that the values for the power-law index α_{SN} in this work are $\alpha_{SN} \sim 4$ as opposed to the observed neutrino flux which has a spectral index ~ 2 (Figure 2.5). This is due to the fact that the proton injection rate Q_p and the neutrino flux F_ν are related by a factor p^2 , as will be shown in Section 6.3.

4.6 Proton injection rate computations

In this section the proton injection rate due to SN activity $Q_{p,SN}$ (Equation 4.20) is computed for the GOALS ULIRG Arp 220 and for the non-U/LIRG starburst galaxies M82 and NGC 253 (Section 3.1). The computations done within this work will be compared to results from [61] and [62].

As previously derived in this chapter, the parameters required to fix the proton injection rate are,

$$Q_{p,SN} = Q_{p,SN}(\alpha_{SN}, \mathcal{R}_{SN}, p_{max}, R_{SBR}). \quad (4.29)$$

The corresponding values for M82, NGC 253, and Arp 220 are shown in Table 4.1. These values are taken from [61] and were obtained by fitting spectral models to multiwavelength observations. It is noted that the ~ 100 pc scales for R_{SBR} are within expectations, as was discussed in Section 3.3.1.

The SN rate (\mathcal{R}_{SN}) is required to fix the normalisation constant $N_{C,SN}$ via Equation 4.27. A numerical code based on the analytic expression in Equation 4.27 was developed within this work

which allows to fix the normalisation constant $N_{C,SN}$ upon input of the parameters \mathcal{R}_{SN} , α_{SN} , and p_{max} . The output of this code, given the values in Table 4.1 as input, is given as well in the last column of Table 4.1. The fact that the normalisation constant of Arp 220 is two orders of magnitude larger than the other two non-U/LIRG starburst galaxies is a direct result of the much larger SN activity in Arp 220.

Once the normalisation constant is known, the proton injection rate can be determined via Equation 4.20. In order to compute the proton injection rate in a systematic manner, the self-written numerical code for the normalisation constant was extended to incorporate the analytic expression in Equation 4.20. As such, the proton injection rate can be computed as function of momentum for any nuclear starburst region in the GOALS sample for which the values of the parameters in Equation 4.29 are known. This code is referred to as the Q_p -code from now on.

The proton injection rates computed with the Q_p -code for the nuclear starburst region of M82, NGC 253, and Arp 220, based on the values in Table 4.1, are shown in Figure 4.6 together with the results of [62]. It can be concluded that the output of the self-written code reproduces the results of [62]. The fact that the proton injection rate in Arp 220 is larger than the proton injection rate in M82 and NGC 253 is a direct result of the larger $N_{C,SN}$ value of Arp 220, as was discussed above.

One should also take into account that the power-law index of Arp 220 is softer than the power-law index of M82 and NGC 253, as indicated in Table 4.1, and therefore results in relatively less neutrinos at higher energies. In order to illustrate the effect of α_{SN} , the proton injection rate for Arp 220 is also shown in Figure 4.6 for a slightly harder value, i.e. $\alpha_{SN} = 4.30$ (dashed line). Nevertheless, all computations in this work for Arp 220 will be done using $\alpha_{SN} = 4.45$.

In Table 4.1 there is only one value quoted for each of the parameters of Arp 220, even though a double-nucleus structure is observed (Section 3.3.4). The reason for this is that in [61], from which the values in Table 4.1 were obtained (except for $N_{C,SN}$), a simplified geometry is adopted for Arp 220 which embeds both nuclei. The values corresponding to this simplified geometry are a reasonable average between the highly compact nuclear regions and their surrounding environment. It is noted that although not ideal such a simplified geometry is acceptable for ULIRGs which are all advanced mergers with a small separation between the nuclei (see Section 3.3.3). The nuclei of Arp 220 will be discussed separately if the available data is at hand.

	\mathcal{R}_{SN} [yr ⁻¹]	R_{SBR} [pc]	α_{SN}	p_{max} [PeV/c]	$N_{C,SN}$ [(GeV/c) ⁻³ s ⁻¹]
Arp 220	2.25	250	4.45	100	1.77×10^{44}
NGC 253	0.027	150	4.30	100	1.60×10^{42}
M82	0.050	220	4.25	100	2.55×10^{42}

Table 4.1: The SN rate \mathcal{R}_{SN} , radius of the starburst region R_{SBR} , the SN power-law index α_{SN} , and the maximum attainable momentum p_{max} for Arp 220, NGC 253, and M82 obtained from [61]. The last column contains the values of the normalisation constant $N_{C,SN}$ acquired from a self-written code based on Equation 4.27.

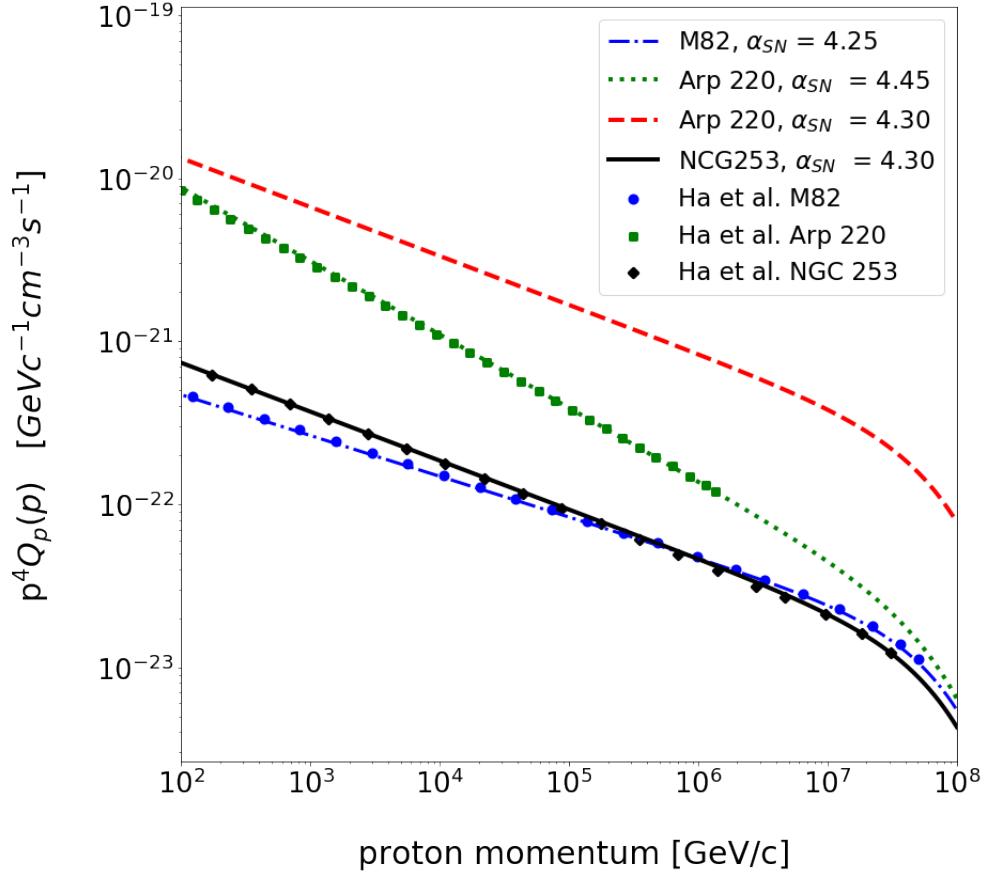


Figure 4.6: Scaled proton injection rate as function of momentum for NGC 253 with $\alpha_{SN} = 4.30$ (full), M82 with $\alpha_{SN} = 4.25$ (dash-dot), Arp 220 with $\alpha_{SN} = 4.45$ (dotted), and Arp 220 with $\alpha_{SN} = 4.30$ (dashed). The results for Q_p by [62] are also shown.

Chapter 5

Proton momentum distribution function

With a proton injection rate $Q_p(p)$ (Chapter 4) in hand it is possible to determine the steady-state proton momentum distribution function f_p via $f_p = \tau_{life} Q_p$ which in addition requires the total lifetime τ_{life} of the proton in the studied starburst region. This simplified relation between f_p and Q_p is typically quoted in the literature without derivation. In Section 5.1 we derive this equality from basic principles in the context of (non-)U/LIRG starburst nuclei. In Section 5.2 the relevant processes affecting τ_{life} in compact starburst regions are identified. In addition, analytic expressions for the corresponding timescales are presented and the electromagnetically observable parameters are highlighted by making the link with Chapter 3. In Section 5.3 these timescales are studied for different parameter ranges which will allow to quantify the efficiency of secondary particle production in (non-)U/LIRG starburst nuclei. Finally in Section 5.4 the output of a self-written code for the steady-state proton momentum distribution function f_p , based on the analytic expressions derived in this chapter, is presented and interpreted. The modeling efforts in this chapter will allow to compute neutrino fluxes of several sources in Chapter 6.

5.1 Proton injection rate vs momentum distribution function

Due to the numerous injection of CRs in the compact starburst regions there is a difference in CR concentration between these inner regions and the rest of the galaxy. Assuming that there are no other processes at play, the injected particles will interact with the magnetic-field structures in the starburst regions leading to a random walk which finally results in diffusion of the CR concentration. Eventually this random walk will transport the CRs out of the starburst region where the ISM density is typically considerably lower. As a result, the CR energy conversion to secondary particles will be less efficient as opposed to the inner starburst regions. This indicates that efficient diffusion might have a significant effect on the CR population. Therefore a first step in finding an expression for the momentum distribution function f_p in the starburst region is to derive the diffusion equation. In fact, the diffusion equation follows directly from the continuity equation which states that the change in density in any part of the system is due to the inflow and outflow of material into and out of that part of the system. This is expressed as

$$\frac{\partial f_p}{\partial t} + \nabla \cdot \mathbf{J} = Q_p, \quad (5.1)$$

with \mathbf{J} the flux of the diffusing substance, which in this case consists of accelerated protons, and Q_p is the source term (discussed in detail in Chapter 4). Fick's first law, which relates the diffusive flux to the gradient of the concentration via the diffusion coefficient D as,

$$\mathbf{J} = -D\nabla f_p, \quad (5.2)$$

is then substituted in the continuity equation. This results in,

$$\frac{\partial f_p}{\partial t} = D\nabla^2 f_p + Q_p, \quad (5.3)$$

which is known as the diffusion equation.

Other processes affecting the transport and energy distribution of CRs, apart from diffusion, can be added to the diffusion equation, e.g. catastrophic interactions, spallation gains and losses, and radioactive decay. In this work the focus lies on nuclear starburst regions containing accelerated protons that are able to produce neutrinos, via inelastic pp -interactions, with energies at the level of IceCube observations (Section 2.3). Therefore the processes of interest are inelastic pp -interactions but also advection of accelerated protons via a galactic-scale outflow, which is driven by the extreme star formation and supernova activity (Section 5.2.2). By taking the average timescales of these processes into account in the diffusion equation it follows that,

$$\begin{aligned} \frac{\partial f_p(\mathbf{r}, p, t)}{\partial t} &= Q_p(\mathbf{r}, p, t) - \frac{f_p(\mathbf{r}, p, t)}{\tau_{gwind}} - \frac{f_p(\mathbf{r}, p, t)}{\tau_{diff}} - \frac{f_p(\mathbf{r}, p, t)}{\tau_{loss}} + D\nabla^2 f_p(\mathbf{r}, p, t) \\ \iff \frac{\partial f_p(\mathbf{r}, p, t)}{\partial t} &= Q_p(\mathbf{r}, p, t) - \frac{f_p(\mathbf{r}, p, t)}{\tau_{life}} + D\nabla^2 f_p(\mathbf{r}, p, t), \end{aligned} \quad (5.4)$$

where $\tau_{life}^{-1} = \tau_{gwind}^{-1} + \tau_{diff}^{-1} + \tau_{loss}^{-1}$ (Section 3.4). Both diffusion and advection by the galactic superwind irrevocably transport CRs away from the neutrino production regions. In order to treat inelastic pp -interactions on the same footing, transfer of CRs between different energies is neglected. This means that once a proton loses its energy to a pp -collision, it is assumed to be removed from the CR population entirely. Due to the fact that $dN/dE \propto E^{-2}$ for the shock-accelerated protons in the nuclear starburst region, as was derived in Section 4.4 (Equation 4.18), this is a reasonable assumption.

One could also wonder about the relevance of continuous momentum losses. The particular processes responsible for these losses depend on the particle type. For protons these are ionization and Coulomb interactions while for electrons Bremsstrahlung and synchrotron emission should be taken into account as well. However, at the proton energies of interest these processes are negligible and therefore the corresponding term was already omitted.

Starburst U/LIRGs do not show signs of temporal variability during the lifetime of current observations and thus a steady-state distribution is assumed ($\partial f_p/\partial t = 0, f(\mathbf{r}, p, t) \rightarrow f(\mathbf{r}, p)$). Furthermore, spatial dependence is considered to be irrelevant, which is a reasonable assumption if the SN remnants are assumed to be distributed homogeneously within the starburst region ($D\nabla^2 f_p(\mathbf{r}, p) = 0, f_p(\mathbf{r}, p) \rightarrow f_p(p)$). Taking into account the steady state and homogeneity in Equation 5.4, the transport equation simplifies to the desired relation

$$\begin{aligned} \frac{f_p(p)}{\tau_{life}} &= Q_p(p) \\ \iff f_p(p) &= \left(\sum_j \tau_j(p)^{-1} \right)^{-1} \frac{1}{V_{SBR}} \sum_i N_{C,i} \left[\frac{p}{m_p c} \right]^{-\alpha_i} e^{\frac{-p}{p_{max,i}}}. \end{aligned} \quad (5.5)$$

It is noted that the total lifetime is not a linear sum of the different contributing processes but rather,

$$\left(\sum_j \tau_j(p)^{-1} \right)^{-1} = \frac{\tau_{gwind} \cdot \tau_{loss}(p) \cdot \tau_{diff}(p)}{\tau_{gwind} \cdot \tau_{loss}(p) + \tau_{loss}(p) \cdot \tau_{diff}(p) + \tau_{diff}(p) \cdot \tau_{gwind}}. \quad (5.6)$$

Here it was assumed that the relevant processes are diffusion, inelastic pp -scattering, and advection. Taking the sum of the inverse time scales ensures that the process with the shortest timescale will be dominant.

Advection and diffusion are both processes removing accelerated protons without conversion to secondary particles as opposed to inelastic pp -interactions and therefore it is also useful to define the escape time τ_{esc}

$$\tau_{esc} \equiv \left(\tau_{gwind}^{-1} + \tau_{diff}^{-1} \right)^{-1}. \quad (5.7)$$

5.2 Typical timescales of transport-shaping processes

From the derivation in the previous section it is concluded that the proton momentum distribution function is determined by the interplay between the proton injection rate (Chapter 4) and the processes shaping the transport of the protons in the starburst region. The relevant processes affecting the CR population in a starburst region were identified to be inelastic pp -interactions, advection by a galactic-scale outflow, and spatial diffusion. Analytic expressions for the typical timescales over which these processes occur are discussed in the following.

5.2.1 Inelastic pp -interactions

The timescale for energy loss via inelastic pp -scattering can be expressed as [75],

$$\tau_{loss} \approx \frac{1}{n_{ism} \cdot \sigma_{pp}(E) \cdot c \cdot \eta}. \quad (5.8)$$

The inelasticity factor η , which is dimensionless, can be seen as a measure of how inelastic a process is and takes values between zero and one. In this work this value is $\eta = 0.50$ [75]. The factor $\sigma_{pp}(E)$ is the cross section of inelastic pp -interactions. The energy-dependent expression for $\sigma_{pp}(E)$ is obtained from [76],

$$\sigma_{pp} = \begin{cases} \sigma_{pp}^{\text{HE}} & = 34.3 + 1.88 \ln L + 0.25L^2 \text{ mb} & E_{\text{lab},p} > 3E_{\text{thr}} \\ \sigma_{pp}^{\text{LE}} & = \sigma_{pp}^{\text{HE}} \left(1 - \left(\frac{E_{\text{thr}}}{E_{\text{lab},p}} \right)^4 \right)^2 & E_{\text{lab},p} < 3E_{\text{thr}}, \end{cases} \quad (5.9)$$

with $L = \ln(E_{\text{lab},p}/1 \text{ TeV})$ and $E_{\text{thr}} = m_p + 2m_\pi + m_\pi^2/2m_p = 1.22 \cdot 10^{-3} \text{ TeV}$ the threshold for π_0 production. The expression for the high-energy range ($E_{\text{lab},p} > 3E_{\text{thr}}$) is obtained from the publicly available SIBYLL code¹. The processes of interest in this work occur at much higher energies than $3E_{\text{thr}}$ and therefore σ_{pp}^{HE} is an appropriate expression for the inelastic pp -scattering cross section. Nevertheless, for the sake of completeness the cross section for the low-energy range ($E_{\text{lab},p} <$

¹SIBYLL is a Monte Carlo model designed for efficient simulation of hadronic multiparticle production up to the highest energies as needed for interpreting cosmic-ray measurements [77].

$3E_{thr}$) is given as well. This expression gives a good description of the cross section around the threshold as can be seen in Figure 5.1.

Finally, n_{ism} [cm^{-3}] is the considered volume ISM density in the starburst region. How the ISM densities are inferred based on electromagnetic data was discussed in Section 3.3.2.

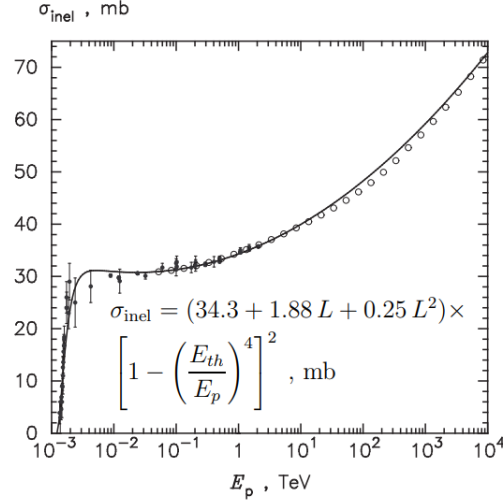


Figure 5.1: Inelastic pp -collision cross section $\sigma_{pp}(E)$ in Equation 5.9 as a function of the incident proton energy in the laboratory frame. The black points with error bars are data [24] while the open points correspond to the cross-sections which are used in the SIBYLL code [76].

5.2.2 Advection: Galactic superwind

The high-velocity stellar winds from the heavy-mass stellar population and the increased SN activity in compact starburst regions of U/LIRGs both lead to injection of kinetic energy into the ISM. The supersonic stellar winds can interact with the surrounding ISM, with other stellar winds, and with SN remnants. Moreover, two or even more SN remnants are also expected to overlap in compact starburst regions. All these interactions produce strong shocks that heat and compress the ISM (Section 4.2). The collective contribution of all this shock heating and pressurizing is expected to result in a cavity of very hot gas with temperature $T \sim 10^8$ K and pressure $P/k_b \sim 10^7$ K cm^{-3} where k_b is the Boltzmann constant. The hot bubble expands above and below the galactic disk due to the pressure imbalance between its central regions and the host galaxy ISM. When the scale height of the disk is reached, the outflow escapes out into the galactic halo. This outflow is typically referred to as the galactic superwind. At the edges of the galaxy the wind remains confined due to the stronger ISM pressure [78]. These outflows are multi-phase, galactic-scale, bipolar-outflows that have been observed in a wide range of starburst galaxies [79]. For example, a galactic-scale molecular outflow has been observed in the LIRG NGC 4418, from the western nucleus of Arp 220 (Section 3.3.4), and from nuclear region A in the LIRG Arp 299 (Section 3.3.5). Also in non-U/LIRGs these outflows are well-observed, e.g. for M82 for which the wind is shown in red in Figure 5.2.

These galactic superwinds play an important role in galaxy formation and evolution. In particular, it quenches star formation by removing gas from the central regions of the galaxy. The outflow

constitutes a self-regulatory mechanism that prevents the stellar mass of the galaxy from growing too much. In this work the outflow is of interest because it advects CRs from the inner starburst regions which could prevent efficient production of secondary particles.

The typical time scale at which accelerated particles are advected away τ_{gwind} can be approximated as the ratio of the radius of the starburst region R_{SBR} divided by the speed of the galactic superwind v_{gwind} ,

$$\tau_{wind} \approx \frac{R_{SBR}}{v_{gwind}}. \quad (5.10)$$

Measurements of v_{gwind} are often based on detection of spectral lines associated to the warm and cold phases of the ISM embedded in the expanding wind. Typical velocities for these warm and cold phases are of the order of 10^2 km s^{-1} . On the other hand, theoretical models and X-ray observations of the wind show that the hot phase of the superwind has a much higher velocity of the order of 10^3 km s^{-1} [78, 79]. In Section 5.3.3 the effect of both the cold and hot phases of the galactic superwind on advection of CRs in (non-)U/LIRGs is explored.

The radius of the starburst region R_{SBR} that is considered is typically determined via interferometric data and IR observations which track the star-forming activity, as was discussed in Section 3.3.1.



Figure 5.2: M82 with its galactic superwind indicated in red [80].

5.2.3 Diffusion

A detailed analysis of diffusion physics in starburst regions goes beyond the scope of this work and therefore only the main concepts are discussed in this section. However it will be argued that diffusion effects are most likely minimal or even negligible in nuclear starburst regions of U/LIRGs.

A fundamental feature of diffusion is that there is no timescale or distance scale due to the random nature of the process. However, there is relation between root-mean-square distance (MSD) [81] and time t . The MSD is defined as,

$$\text{MSD} \equiv \langle |\mathbf{r}(t) - \mathbf{r}_0|^2 \rangle, \quad (5.11)$$

with $\mathbf{r}(t)$ the position of the CR at time t in the starburst region and \mathbf{r}_0 the location at injection time. The relation between MSD and time t is then expressed as,

$$\text{MSD} \propto Dt, \quad (5.12)$$

with D the diffusion coefficient. MSD can therefore be seen as a measure of the deviation between the position of the CR at a time t and the location at injection time. This is the most common measure of the spatial extent for a random motion. Considering that the particle should (approximately) travel the radius of the starburst region after injection, the diffusion time scale is thus approximated as

$$\tau_{diff} \approx \frac{R_{SBR}^2}{D(p)}, \quad (5.13)$$

where $D(p)$ is the momentum-dependent diffusion coefficient, which also depends on the considered model.

Different diffusion models for starburst regions have been studied in the literature. In [61] it is argued that the prolific supernova and star-forming activity in starburst regions is likely to produce a high level of turbulence, which is expected to be reflected in a small diffusion coefficient. Moreover, this is most likely even more prominent in U/LIRGs which typically exhibit higher supernova and star-formation rates (e.g. Table 4.1) as opposed to the other types of starburst galaxies, as discussed in Section 5.3.2. The diffusion coefficient for such a high-turbulence model goes as $D(p) \propto p^{\frac{1}{3}}$ and therefore $\tau_{diff} \propto p^{-\frac{1}{3}}$ [61]. In addition [61] also considers a diffusion scenario which mimics the diffusion coefficient of the Milky Way. Such a scenario leads to faster diffusion than expected for a high-turbulence environment. In that case the transport of CRs is dominated by diffusion over the whole energy range of interest. However, due to the extreme starburst activity in U/LIRGs as opposed to the Milky Way, such a Galactic diffusion coefficient is most likely not a correct description for starburst regions.

The procedure for fixing the normalisation constant of the diffusion coefficient lies beyond the scope of this work but can for example be found in [61] and [62]. Nevertheless, as will be discussed in Section 5.3, the timescales for diffusion effects in U/LIRGs are expected to be subdominant.

5.3 Calorimetric requirement and timescale comparison

Compact starburst regions are of particular interest as high-energy neutrino source candidates if all of the initial injected CR energy is converted to secondary particles, i.e. the starburst acts as a calorimeter. To achieve this, the inelastic pp -interaction timescales in the considered region must be much smaller than the escape time τ_{esc} [61],

$$\tau_{loss} \ll \tau_{esc} = \left(\tau_{wind}^{-1} + \tau_{diff}^{-1} \right)^{-1} \quad [\text{calorimeter requirement}]. \quad (5.14)$$

In what follows the relevance of the different processes shaping cosmic-ray transport and the efficiency of secondary particle production in nuclear regions of (non-)U/LIRGs will be discussed in more detail. In Section 5.3.1 and Section 5.3.2 the focus will lie on the relevance of diffusion effects in non-U/LIRG and U/LIRG starburst nuclei, respectively. In Section 5.3.3 the effect of advection via the galactic-scale outflow will be discussed for both non-U/LIRG and U/LIRG starburst nuclei following an argument developed within this work.

5.3.1 Timescales in non-U/LIRG starburst nuclei

Figure 5.3 shows τ_{loss} (blue dashed), τ_{gwind} (solid red), and τ_{diff} (green dash-dot) for a starburst region with $R_{SBR} = 200$ pc, $v_{gwind} = 500$ km/s, and $n_{ism} = 125$ cm $^{-3}$. These are reference values given in [61] which aim to mimic conditions in starburst galaxies such as M82 rather than in U/LIRGs. The diffusion timescale shown as function of momentum in Figure 5.3 is for a diffusion coefficient with $D(p) \propto p^{\frac{1}{3}}$ and therefore $\tau_{diff} \propto p^{-\frac{1}{3}}$ (Equation 5.13), i.e. the high-turbulence scenario discussed in Section 5.2.3. It was already mentioned that the normalisation process for the diffusion coefficient lies beyond the scope of this work. Nonetheless, in order to visualize the diffusion timescale for further discussions, a fit of the form $\tau_{diff} \propto p^{-\frac{1}{3}}$ was done to the results presented in [61]. The grey highlighted area in Figure 5.3 corresponds to proton energies required to produce neutrinos via pp -interactions which are consistent with the astrophysical IceCube neutrino flux². The behaviours of advection, diffusion, and inelastic scattering are of main interest in this momentum range. Lastly it is noted that the momentum range in Figures 5.3 intentionally starts from 100 GeV/c since at lower energies ionization and Coulomb-interaction effects become significant, especially below the pion-production threshold. Nevertheless, this momentum range is not of interest here and is therefore omitted in this work (see Section 5.1).

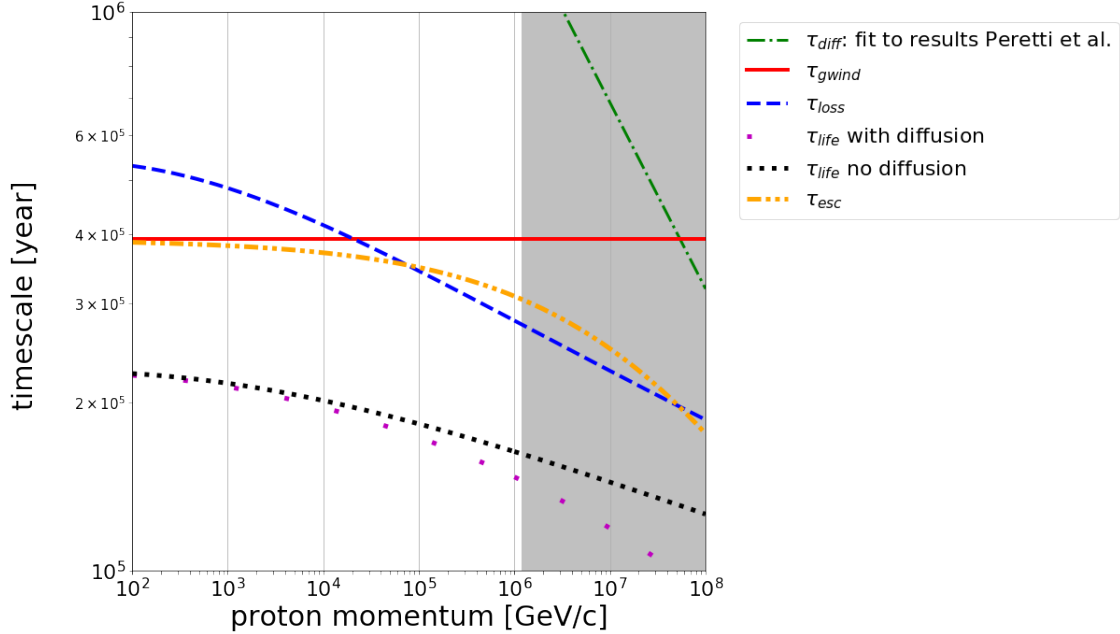


Figure 5.3: Timescales for advection via the galactic superwind (full red line), diffusion (green dash dot), and inelastic pp -interactions (blue dashed) for $R_{SBR} = 200$ pc, $v_{gwind} = 500$ km/s and $n_{ism} = 125$ cm $^{-3}$. The diffusion timescale is based on the high-turbulence ISM discussed in the text. The total lifetime is also shown where the loosely dotted magenta points take into account diffusion while the densely dotted black points do not. The orange double-dot-dashed line is the escape timescale τ_{esc} as defined in Equation 5.7. The highlighted area corresponds to proton energies required to produce neutrino energies via pp -interactions consistent with the observed diffuse astrophysical neutrino flux.

²The lower value of this energy range of interest was obtained from $E_p = 20 \cdot 60$ TeV based on the fact that the through-going muon analysis starts from 60 TeV (Figure 2.5) and $E_\nu \simeq E_p/20$ (Section 2.1) for pp -interactions.

Given the timescales of all the processes in Figure 5.3, it can be concluded that for the highest energies diffusion effects become comparable to advection and inelastic scattering timescales. However, by comparing the total lifetime of the proton in the starburst region with diffusion effects included (loosely dotted magenta points) and the total lifetime of the proton in the starburst region with diffusion effect omitted (densely dotted black points), it is concluded that diffusion only has a minor effect on the total lifetime τ_{life} .

For the proton momenta of interest, it can be concluded that the escape timescale τ_{esc} (orange double-dot-dashed line, Equation 5.7) is comparable to τ_{loss} and therefore the calorimeter requirement (Equation 5.14) is not satisfied for the given starburst-specific parameters. However, it is still possible that protons lose an appreciable fraction of their energy in the starburst region since advection is not dominant.

It is noted that the reference value adopted for the ISM density is most likely an underestimation rather than an overestimation for M82-like galaxies. However, this does not change the conclusion that the contribution of diffusion effects is subdominant. If anything, diffusion effects will be even less relevant because for larger ISM densities the inelastic pp -interaction timescale is even smaller. In addition larger ISM densities would also imply better calorimeter conditions.

5.3.2 Timescales in U/LIRG starburst nuclei

In this work the focus lies on compact starburst regions in U/LIRGs. Nuclear starburst regions of ULIRGs have ISM densities of $\langle n_{ism} \rangle \gtrsim 10^3\text{-}10^4 \text{ cm}^{-3}$ [74]. For LIRGs similar conditions are found, e.g. Arp 299-A for which $n_{ism} = 1\text{-}5 \times 10^3 \text{ cm}^{-3}$ is inferred [82]. These ISM densities are in contrast with the n_{ism} values of the order of 10^2 cm^{-3} for non-U/LIRGs starburst nuclei, as discussed in previous section. Moreover, U/LIRGs have similar values for R_{SBR} and v_{gwind} as the non-U/LIRG nuclear regions. As a direct result of these extreme densities and given that $\tau_{loss} \propto n_{ism}^{-1}$ (Equation 5.8), it is expected that diffusion effects are even less prominent in U/LIRGs. In addition, the larger star-formation rate and supernova activity in U/LIRGs results in a more turbulent medium and therefore larger diffusion timescales (Section 5.2.3). In conclusion, compact starburst regions in U/LIRGs are basically extreme forms of the non-U/LIRG variants and diffusion effects are irrelevant. This is now quantified by taking the nuclear regions of Arp 220 as an example. Here the western nucleus of Arp 220 will also be discussed separately because the required data is available.

Figure 5.4 shows τ_{gwind} and τ_{loss} for the western nucleus in the ULIRG Arp 220 and for the simplified geometry which embeds its double-nucleus structure (see Section 3.3.4 and Section 4.6). The density and galactic superwind speed for the simplified geometry were taken from [61] and were obtained by fitting spectral models to multiwavelength observations. These values are part of the same fitting results already mentioned in Section 4.6. The wind speed of the western nucleus was estimated from direct observations of line emission (HCO & CO) and direct observations of the dust continuum (Section 3.3.2) with the Atacama Large Millimeter Array (ALMA). Based on these observations the galactic-scale outflow was estimated to move at $\sim 840 \text{ km s}^{-1}$ [83]. The density of the western nucleus was inferred by ALMA observations as well [55]. The eastern nucleus of Arp 220 is not discussed in more detail because the appropriate values for v_{gwind} and n_{ism} were not found in the literature.

Figure 5.4 shows that for the simplified geometry τ_{loss} is more than an order of magnitude below τ_{gwind} . This becomes even more significant for the case where we consider the western nucleus separately. This allows us to conclude that the calorimetric requirement (Equation 5.14) is satisfied for both scenarios. Therefore efficient neutrino production is expected to occur in these regions. Even if the diffusion effects would occur at timescales comparable to the advection timescales, as

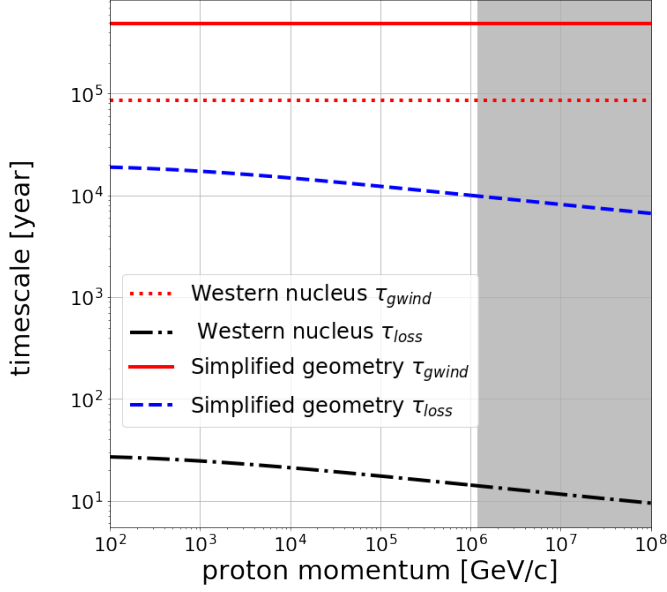


Figure 5.4: Timescales for advection via the galactic superwind and inelastic pp -interactions for the simplified geometry of Arp 220 which embeds its double-nucleus structure and for the western nucleus of Arp 220. For the simplified geometry $R_{SBR} = 250 \text{ pc}$, $v_{gwind} = 500 \text{ km/s}$, and $n_{ism} = 3500 \text{ cm}^{-3}$ are taken from [61] and were obtained by fitting spectral models to multiwavelength observations. For the western nucleus $R_{SBR} = 74 \text{ pc}$, $v_{gwind} = 840 \text{ km/s}$ [83], and $n_{ism} = 2.4 \times 10^6 \text{ cm}^{-3}$ [55] were obtained from direct observations with ALMA.

was observed for the non-U/LIRG nuclei (Section 5.3.1), it would only have a negligible effect.

5.3.3 Equilibrium wind in starburst nuclei

In this section the effect of the galactic superwind on advection of CRs is investigated in both non-U/LIRG and U/LIRG starburst nuclei. In order to do this a novel quantity is introduced, the equilibrium wind.

By imposing $\tau_{loss} = \tau_{gwind}$ the galactic superwind speed v_{gwind} can be solved in terms of the ISM density n_{ism} as,

$$\begin{aligned} \tau_{gwind} = \tau_{loss} &\iff \frac{R_{SBR}}{v_{eq,gwind}} = \frac{1}{\eta \cdot \sigma_{pp}(E) \cdot n_{ism} \cdot c} \\ &\iff v_{eq,gwind}(E) = n_{ism} \cdot R_{SBR} \cdot c \cdot \eta \cdot \sigma_{pp}(E). \end{aligned} \quad (5.15)$$

The parameter $v_{eq,gwind}$, which will be referred to as the equilibrium wind, is the galactic superwind speed required to achieve equal timescales over which inelastic pp -scatterings and advection occur in the nuclear starburst region, i.e. $\tau_{loss} = \tau_{gwind}$. Since $\tau_{loss} \sim \sigma_{pp}^{-1}(E)$ (Equation 5.8) it follows that the equilibrium wind depends on the proton energy as opposed to the galactic superwind which is independent of the proton energy. This is clarified by Figure 5.3 from which it is concluded that at $\sim 2 \times 10^4 \text{ GeV/c}$ the equality $\tau_{gwind} = \tau_{loss}$ is satisfied, while for larger momenta this equality can only be achieved if the speed of the galactic superwind is larger and therefore

would lead to a smaller τ_{gwind} value. In that case the intersection between the solid red line and dashed blue line would occur at larger energies. Given this interpretation of the equilibrium wind it is now possible to proceed with the argument which aims to quantify the relevance of advection effects to the transport of cosmic rays in starburst nuclei.

Although the equilibrium wind (Equation 5.15) is energy dependent, the cross section $\sigma_{pp}(E)$ barely increases in the proton energy range of interest and will therefore be fixed to $\sigma_{pp}(E = 10^7 \text{ GeV})$ for this argument. Doing this allows to construct Figure 5.5 which shows the equilibrium wind speed $v_{eq,wind}$ (Equation 5.15) for typical radii R_{SBR} of compact starburst regions and the ISM volume densities n_{ism} within these radii. To be clear, Figure 5.5 shows the average galactic superwind speed v_{gwind} required to achieve $\tau_{gwind} = \tau_{loss}$ in a nuclear starburst region with a certain R_{SBR} and n_{ism} value. In addition, M82, NGC 253, Arp 299-A, and Arp 220 are indicated at their R_{SBR} and n_{ism} values together with the corresponding $v_{eq,gwind}$ value (Equation 5.15). As mentioned above, the ISM density in Arp 299-A has been estimated to be in the range of $1\text{-}5 \times 10^3 \text{ cm}^{-3}$. Here an average value of 2500 cm^{-3} was chosen.

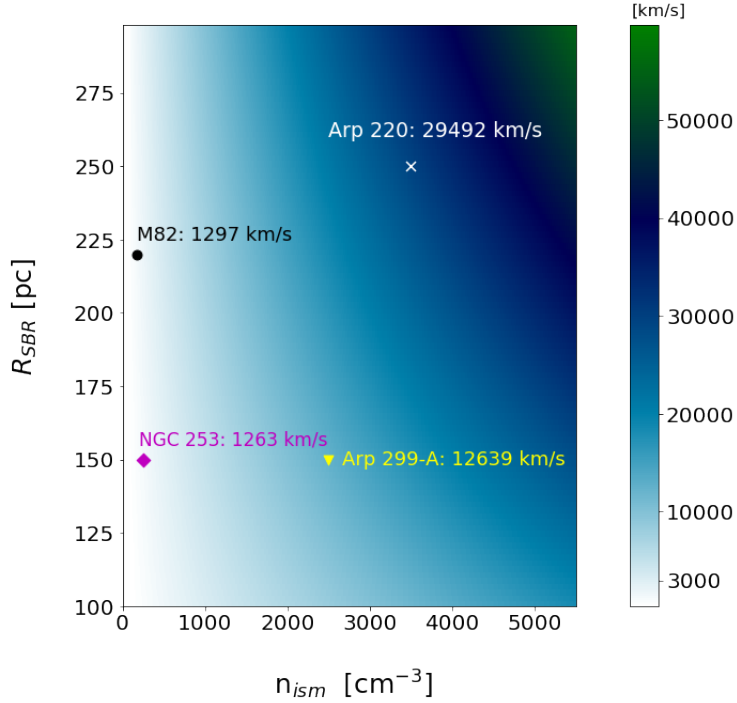


Figure 5.5: The average galactic superwind speed required to achieve $\tau_{loss} = \tau_{gwind}$ in compact starburst regions with a certain radius R_{SBR} and ISM density n_{ism} . M82, NGC 253, Arp 299-A, and Arp 220 are indicated at their corresponding R_{SBR} and n_{ism} values.

In order to interpret Figure 5.5 it is recalled that the observed and simulated galactic superwind speeds v_{gwind} (not the equilibrium wind $v_{eq,gwind}$ in Equation 5.15) are found to be of the order of $\sim 100 \text{ km/s}$ for the cold phases and a few 1000 km/s for the hot phases (Section 5.2.2). Moreover, it was noted previously that the nuclear regions of U/LIRGs are expected to have $\langle n_{ism} \rangle \gtrsim 10^3\text{-}10^4 \text{ cm}^{-3}$. In the plot examples of both a LIRG (Arp 299-A) and an ULIRG (Arp 220) are given. We find that the required wind to arrive at a comparable timescale for advection and inelastic scatterings,

5.3. CALORIMETRIC REQUIREMENT AND TIMESCALE COMPARISON

given typical U/LIRG conditions, is way above the observed and simulated galactic superwind velocities v_{gwind} of these objects. Based on this argument it is concluded that advection effects will typically have a minor or even negligible effect on the transport of protons in the nuclear regions of U/LIRGs.

For the non-U/LIRG starburst galaxies M82 and NGC 253 with relatively lower ISM densities the situation is different. On the one hand the equilibrium wind speed for these objects indicated in Figure 5.5 is larger than the observed and simulated wind speeds for the cold phases of the galactic superwind, although the difference is less prominent than for U/LIRGs. On the other hand, the observed and simulated wind speeds for the hot phases in the galactic superwind are of the order of the indicated equilibrium wind speed. This allows to conclude that opting for the wrong phase (cold or hot) to characterize advection of CRs via the galactic superwind could have a significant effect for the modeling of neutrino production in non-U/LIRG starburst galaxies. This is in contrast with U/LIRG starburst nuclei where the speed ranges for both the hot and cold phases are well below the equilibrium wind speed of these objects. This is also illustrated in Figure 5.6 and Figure 5.7 where the equilibrium wind is shown as function of proton momentum for the non-U/LIRG and U/LIRG starburst nuclei, respectively. The cold and hot phases of the galactic superwind v_{gwind} are also indicated. From these figures it is also clear that in the energy range of interest the energy dependence barely increases as was claimed above.

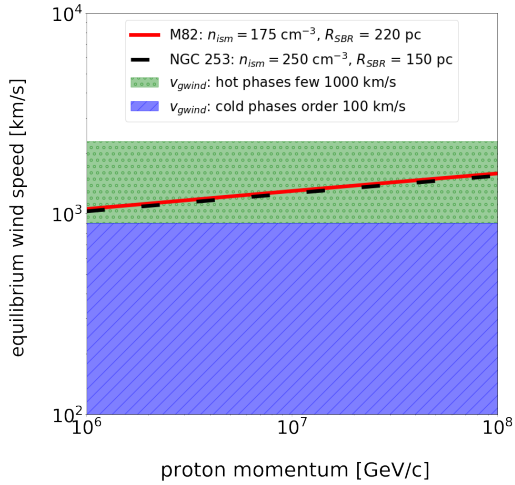


Figure 5.6: The equilibrium wind speed $v_{eq,gwind}$ as function of proton momentum for M82 and NGC 253 (non-U/LIRG). The proton momentum range corresponds to momenta required to produce neutrino energies via pp -interactions consistent with the observed diffuse astrophysical neutrino flux. The green highlighted area corresponds to speeds for the hot phases in the galactic-scale outflow v_{gwind} while the blue area corresponds to speeds for the cold phases in the galactic superwind. The values for n_{ism} and R_{SBR} for M82 and NGC 253 were taken from [61].

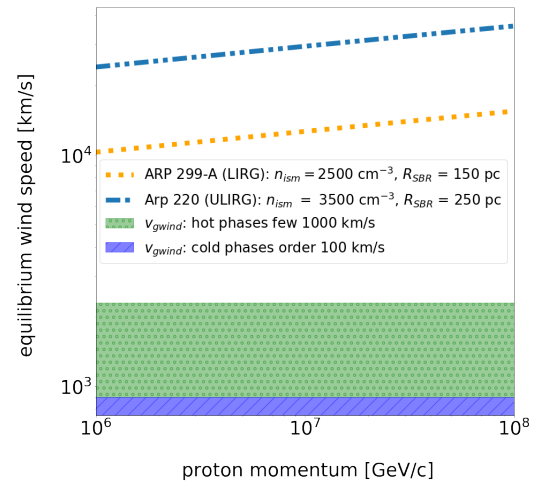


Figure 5.7: Same as Figure 5.6 for the U/LIRG scenario. The values for n_{ism} and R_{SBR} for Arp 220 were taken from [61] and for Arp 299-A from [59, 82].

5.4 Computations of the proton momentum distribution function

It has been shown in Section 4.6 that the proton momentum distribution function $f_p(p)$ for a nuclear starburst region, which is in a steady state with homogeneously distributed accelerators, is equal to the product of the proton injection rate Q_p and the total lifetime τ_{life} in that region. Considering only particle acceleration due to SN activity and focusing on one particular starburst region in the galaxy, the analytic expression is then in full

$$\begin{aligned}
 f_p(p) &= \tau_{life} \cdot Q(p) = \tau_{life} \cdot \frac{N_{C,SN}}{V_{SBR}} \left(\frac{p}{m_p c} \right)^{-\alpha_{SN}} e^{\frac{-p}{p_{max,SN}}} \\
 &= \underbrace{\left[\left(\frac{1}{n_{ism} \sigma_{pp} c \eta} \right)^{-1} + \left(\frac{R_{SBR}}{v_{gwind}} \right)^{-1} \right]^{-1}}_{\tau_{life}} \cdot \left(\frac{1}{\left(\frac{4\pi}{3} \right) R_{SBR}^3} \left(\frac{p}{m_p c} \right)^{-\alpha_{SN}} e^{\frac{-p}{p_{max,SN}}} \right) \\
 &\times \underbrace{\frac{\xi_{CR} E_{SN} \mathcal{R}_{SN}}{\int_0^\infty 4\pi p^2 \left(\frac{p}{m_p c} \right)^{-\alpha_{SN}} e^{\frac{-p}{p_{max,SN}}} \cdot \left(\sqrt{p^2 c^2 + m^2 c^4} - mc^2 \right) dp}}_{N_{C,SN} \text{ (Section 4.5.1)}},
 \end{aligned} \tag{5.16}$$

where the starburst volume V_{SBR} is assumed to be a sphere. Moreover, diffusion effects are not taken into account. This is a reasonable assumption for both non-U/LIRG and U/LIRG starburst nuclei in the proton energy range of interest as was argued in Section 5.3. The starburst-specific parameters which are inferred from electromagnetic observations are R_{SBR} , n_{ism} , v_{gwind} , α_{SN} , and \mathcal{R}_{SN} (see Chapter 3). The maximum attainable momentum p_{max} is not expected to vary significantly in the source population and is typically left as free parameter. This parameter was discussed in Section 4.5.3. The power-law index α_{SN} is a special case which will be discussed in more detail in Section 6.3. The rest of the parameters are predetermined or constants. In conclusion, the parameters required to fix the proton momentum distribution function are,

$$f_p = f_p(R_{SBR}, n_{ism}, \mathcal{R}_{SN}, \alpha_{SN}, p_{max}, v_{gwind}). \tag{5.17}$$

In Section 4.6 we used the Q_p -code developed in this work to compute the proton injection rates of M82, NGC 253, and Arp 220. This code was extended to incorporate the analytic expression of Equation 5.16 in order to determine the proton momentum distribution function $f_p(p)$ which is referred to as the f_p -code from now on. As such, the proton momentum distribution function can be computed for any nuclear starburst region upon input of the parameters given in Equation 5.17. The only parameters which are starburst specific, in addition to those required for the proton injection rate (Table 4.1), are the ISM density n_{ism} and the speed of the galactic superwind v_{gwind} . The corresponding values for M82, NGC 253, and Arp 220 are shown in Table 5.1 and were obtained from [61]. The output of the f_p -code for the three galaxies, upon input of the values in Table 4.1 and Table 5.1, is shown in Figure 5.8.

The steady-state proton momentum distribution function $f_p(p)$ can be seen as a snapshot of the accelerated protons present in the nuclear starburst region. As a result of the significantly larger ISM density in Arp 220, protons are converted to neutrinos at a higher rate as opposed to the other two galaxies. This, in combination with the fact that Arp 220 has a softer injection spectral index α_{SN} (Table 4.1), results in $f_p(p)$ values for Arp 220 which are below the $f_p(p)$ values for M82 and NGC 253 in the ≥ 1 TeV/c momentum range.

	v_{gwind} [km/s]	n_{ism} [cm ⁻³]
M82	600	175
NGC 253	300	250
Arp 220	500	3500

Table 5.1: v_{gwind} and n_{ism} values to determine $f_p(p)$ in Figure 5.8. These values are taken from [61] and were obtained by fitting spectral models to multiwavelength observations.

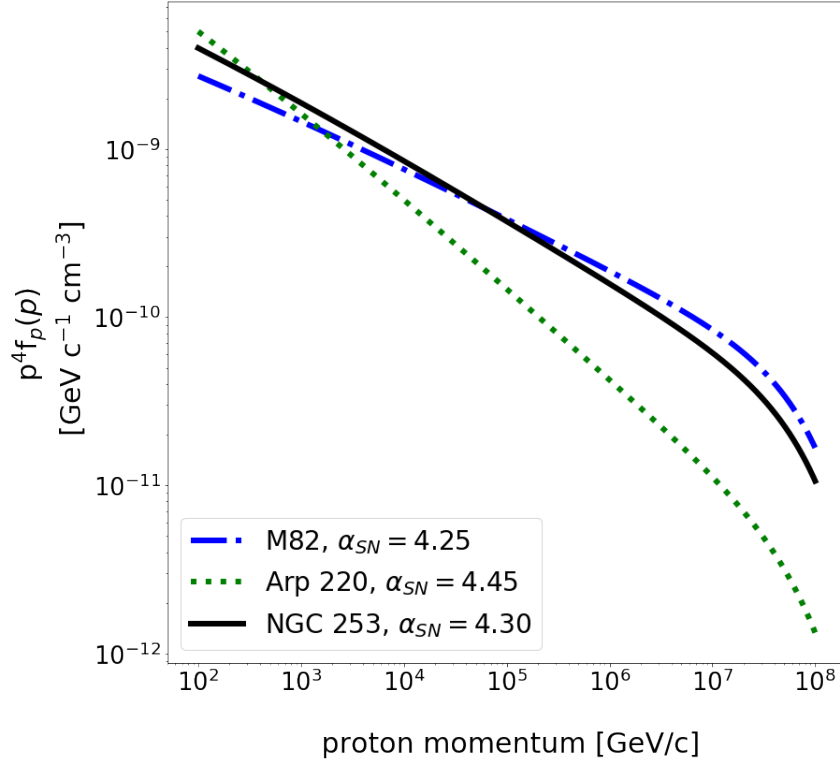


Figure 5.8: Proton momentum distribution $f_p(p)$ as function of momentum for Arp 220, NGC 253, and M82 computed with the f_p -code. The parameters required to compute f_p are given in Table 4.1 and Table 5.1.

Chapter 6

Neutrino flux from starburst-driven U/LIRGs

In this chapter we will work towards the prediction of a neutrino flux from starburst-driven GOALS U/LIRGs. So far an expression for the proton momentum distribution function f_p (Chapter 5) has been derived, which is determined by the interplay between injection of relativistic protons (Q_p) and the dominant processes shaping the transport of these protons (τ_{life}) in the considered starburst region. In Section 2.1 it was argued that astrophysical neutrinos are predominantly produced via the decay of charged pions. The relation between the proton momentum distribution $f_p(p)$, the pion production rate $q_\pi(E)$, and the neutrino production rate $q_\nu(E)$ at the source is discussed in Section 6.1. For these relations the results of [76] are used. However, its application to GOALS objects based on GOALS parameter input and subsequent interpretation is novel. Subsequently, this neutrino production rate will allow to derive an expression for the total neutrino flux at Earth. To find an expression for the single-flavor neutrino flux the effects of neutrino oscillation must be taken into account, which we will briefly describe in section 6.2.

The discussion in Section 6.1 will also allow to address a possible way to infer the power-law index α_{SN} in Section 6.3, which is the only required parameter for the neutrino-flux modeling which has not been discussed so far. Finally, the numerical code based on analytic expressions developed in this work is finalized in Section 6.4 in order to compute the (single-flavor) neutrino flux related to any nuclear region in the GOALS sample upon input of 7 starburst-specific parameters.

6.1 Neutrino-production rate

In order to estimate the production rate of neutrinos $q_\nu(E)$ in compact starburst regions of U/LIRGs, the expressions of [76] are used in which parameterizations are given for energy spectra of π -mesons, gamma rays, electrons, and neutrinos produced in inelastic pp -interactions. Before using these expressions to arrive at a neutrino flux, they are first examined in some more detail. The neutrino production rate in [76] is given by

$$q_{\nu+\bar{\nu}}(E) \equiv q_\nu(E_\nu) = 2 \int_0^1 \left[\mathcal{F}_{\nu_\mu^{(1)}}(x) + \mathcal{F}_{\nu_\mu^{(2)}}(x) + \mathcal{F}_{\nu_e}(x) \right] q_\pi \left(\frac{E_\nu}{x} \right) \frac{dx}{x} \quad [\text{GeV}^{-1} \text{cm}^{-3} \text{s}^{-1}]. \quad (6.1)$$

The factor $x \equiv E_\nu/E_\pi$ is the neutrino-to-pion energy ratio and $\mathcal{F}_i(x)$, with $i \in \{\nu_\mu^{(1)}, \nu_\mu^{(2)}, \nu_e\}$, are the probability distribution functions (PDFs) describing the probability of a neutrino carrying away a certain fraction of the pion energy in the decay. The functions $\mathcal{F}_{\nu_\mu^{(1)}}(x)$ and $\mathcal{F}_{\nu_\mu^{(2)}}(x)$ describe muon neutrinos produced by $\pi \rightarrow \mu\nu_\mu$ and $\mu \rightarrow \nu_\mu\nu_e e$, respectively. The function $\mathcal{F}_{\nu_e}(x)$ describes the production of electron neutrinos¹ through the latter process. Figure 6.1 shows the PDFs as a function of x . The sudden truncation at $x = 0.427$ for the muon neutrino produced in the pion-to-muon decay follows directly from deriving the maximum neutrino energy in the lab frame $E_{\nu, \max}$. Performing a Lorentz boost from the pion rest frame to the lab frame and assuming that $E_\pi \gg m_\pi$ allows to derive $E_{\nu, \max} \approx \lambda E_\pi$ with $\lambda = 1 - m_\mu^2/m_\pi^2 = 0.427$. For the muon decay one finds, if $m_e \ll m_\mu$ is assumed, that the maximum muon energy in the lab frame is $E_{\mu, \max} \approx E_\pi$. The spectra of all secondaries which are produced at the decay of muons will therefore continue up to the energy E_π , as observable in Figure 6.1. Lastly it is noted that the factor 2 in Equation 6.1 is included to take into account the contributions of both π^+ and π^- decays.

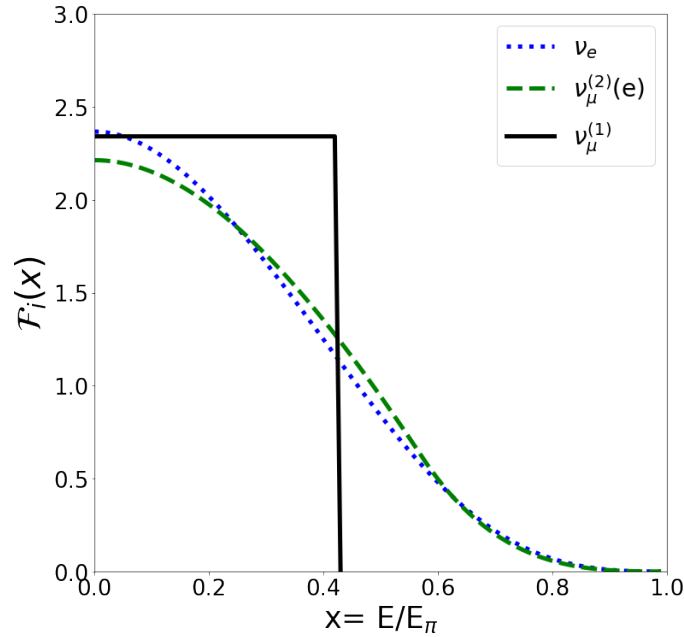


Figure 6.1: Energy distributions of the neutrinos produced in the decays of monoenergetic ultrarelativistic charged pions in the lab frame. All $\mathcal{F}_i(x)$ are normalized to 1, i.e. $\int_0^1 \mathcal{F}_i(x) dx = 1$. These PDFs were reproduced with the expressions given in [76]. It should be noted that [76] has an erratum containing the correct expression for one of the functions.

The pion production rate $q_\pi(E)$ in Equation 6.1 is also given in [76] as,

$$q_\pi(E_\pi) = \frac{n_{ism} c}{K_\pi} \sigma_{pp}(\alpha) n_p(\alpha) \quad \text{with} \quad \alpha = m_p c^2 + \frac{E_\pi}{K_\pi} \quad [\text{GeV}^{-1} \text{cm}^{-3} \text{s}^{-1}], \quad (6.2)$$

where $n_p(E)dE = 4\pi p^2 f(p) dp$ is the energy distribution function of injected protons with $f_p(p)$ the

¹It is noted that in [76] an erratum is given for this function because of an error in the expression. This error was found and solved by us before finding the erratum.

proton momentum distribution function discussed in Chapter 5. The parameter n_{ism} is the ISM density of the considered compact starburst region and $\sigma_{pp}(E)$ is the cross section of the inelastic pp -interaction for which the expression is given in Equation 5.9. Finally, K_π is the fraction of kinetic energy transferred from the parent proton to the produced pion for which $K_\pi \simeq 0.17$ is adopted [76]. It is noted that the pion production rate does not require new starburst-specific parameters apart from those needed to compute f_p (Section 5.4).

6.1.1 Neutrino-production rate computations

The f_p -code developed in Section 5.4 was extended to incorporate the analytic expression of Equation 6.1 and Equation 6.2. This allows to compute the neutrino-production rate in any nuclear starburst region upon input of the starburst-specific parameters,

$$q_\nu = q_\nu(R_{SBR}, n_{ism}, \mathcal{R}_{SN}, \alpha_{SN}, p_{max}, v_{gwind}). \quad (6.3)$$

The output of this neutrino-production code, referred to as q_ν -code from now on, is shown in Figure 6.2 for M82, NGC 253, and ARP 220 with all the required parameters given in Table 4.1 and Table 5.1.

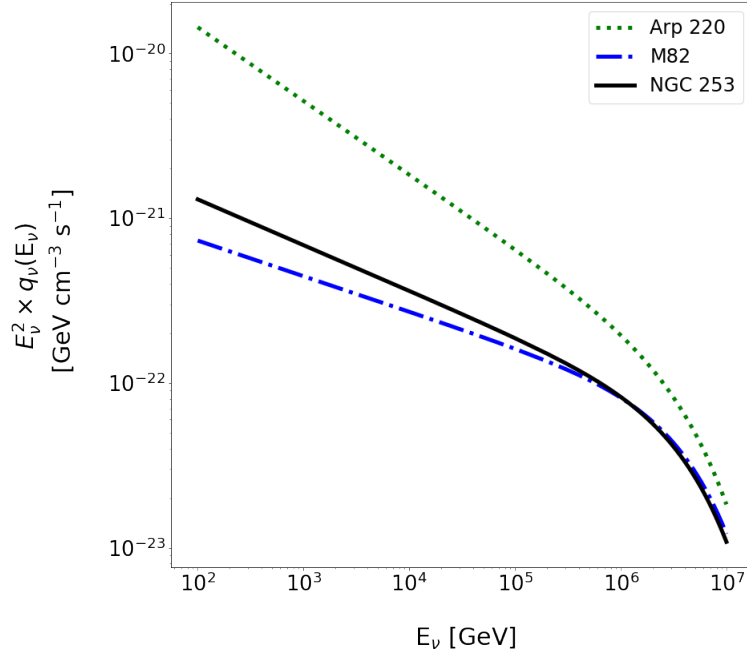


Figure 6.2: Scaled neutrino production rate for M82, NGC 253, and Arp 220 as function of neutrino energy based on the values in Table 4.1, Table 5.1, and the probability density functions in Figure 6.1.

The study of the proton momentum distribution functions in Figure 5.8 showed that for $\gtrsim 1$ TeV/c the $f_p(p)$ values of Arp 220 are consistently below those of M82 and NGC 253. This was argued to be the result of the larger ISM density in Arp 220 (Table 5.1), which results in a larger conversion rate of protons to high-energy neutrinos and therefore smaller steady state $f_p(p)$ values. This interpretation is now confirmed by Figure 6.2 where the neutrino production rate of Arp

220 is observed to be larger over the whole neutrino energy range.

One interesting scenario is found by considering a nuclear starburst region in which the ISM density is steadily increased. It is expected that the corresponding neutrino production rate will stabilize from a certain ISM density onwards. This is argued in what follows.

If the value of the ISM density is large enough, with the exact value depending on the other structural parameters of the nuclear region, it follows that $f_p = Q_p \tau_{life} \approx Q_p \tau_{loss}$ (See Equation 5.16). It is noted that this implies that the calorimeter requirement is satisfied (Equation 5.14). The implication for the neutrino-production rate (Equation 6.1) is then

$$\begin{aligned}
 q_\nu &\propto n_{ism} \sigma_{pp} Q_p \tau_{life} \\
 &\approx n_{ism} \sigma_{pp} Q_p \tau_{loss} \\
 &\propto \sigma_{pp} n_{ism} Q_p \frac{1}{n_{ism} \sigma_{pp}} = Q_p(R_{SBR}, \alpha_{SN}, p_{max}, \mathcal{R}_{SN}).
 \end{aligned} \tag{6.4}$$

In that case the neutrino production rate can only significantly increase if the proton injection rate increases, and no longer depends on the ISM density. In order to discuss this in a more quantitative way for a particular source we introduce in this work the quantity \mathcal{V} as,

$$\begin{aligned}
 \mathcal{V} &= \mathcal{V}(E_\nu, R_{SBR}, n_{ism}, \mathcal{R}_{SN}, \alpha_{SN}, p_{max}, v_{gwind}) \\
 &\equiv \frac{q_\nu(E_\nu, R_{SBR}, n_{ism}, \mathcal{R}_{SN}, \alpha_{SN}, p_{max}, v_{gwind})}{q_{\nu, n_{ism} \rightarrow \infty}(E_\nu, R_{SBR}, n_{ism} \rightarrow \infty, \mathcal{R}_{SN}, \alpha_{SN}, p_{max}, v_{gwind})}.
 \end{aligned} \tag{6.5}$$

This is the neutrino production rate of a source divided by the same neutrino production rate but with the ISM density taken to infinity in order to mimick a perfect calorimeter (under the somewhat artificial assumption that the proton injection rate is unaffected). In Figure 6.3 this quantity is shown for the starburst-specific parameters of Arp 220 given in Tables 4.1 and 5.1 but for various ISM densities. It is concluded that by gradually increasing the ISM density the neutrino production rate converges to a constant value, as expected. The ISM density of Arp 220 used in the calculations so far is also indicated by the dash-double-dotted black line. Moreover, it can be concluded from Figure 6.3 that if the ISM density of the simplified geometry of Arp 220 is underestimated, it will not have a significant impact on the neutrino-production rate.

It is noted that Equation 6.4 only holds if the calorimeter requirement (Equation 5.14) is satisfied. The parameters that mainly characterize the neutrino-production rate at the source are \mathcal{R}_{SN} , α_{SN} , and p_{max} (see Equation 4.29) in the case of calorimetric conditions. This highlights the need for electromagnetic expertise and observational data of the GOALS collaboration to accurately constrain \mathcal{R}_{SN} and even more so the spectral index α_{SN} , as will be clear from the discussion in Section 6.5. In addition, from the discussion given in Section 5.3 it is expected that U/LIRGs will typically satisfy the conditions of Equation 6.4 while for non-U/LIRG starburst nuclei this will depend on the source under investigation.

In Figure 6.4 the $\mathcal{V}(E_\nu)$ parameter is shown as function of energy for M82, NGC 253, and Arp 220 for the values in Table 4.1 and Table 5.1. It is concluded that for these values NGC 253 and Arp 220 approach full calorimetric scenarios while M82, especially at the lowest energies, does not.

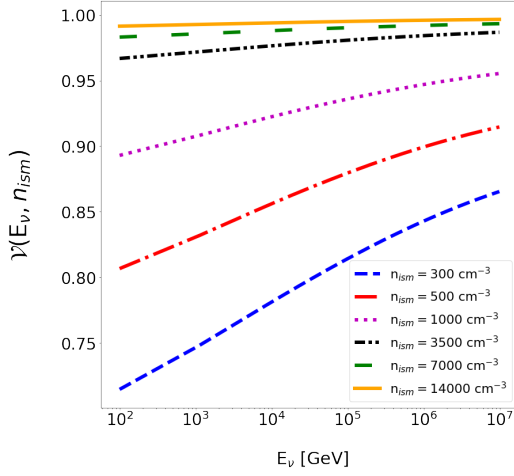


Figure 6.3: $\mathcal{V}(E_\nu, n_{ism})$ for densities between 300 cm^{-3} and 14000 cm^{-3} as function of neutrino energy E_ν for Arp 220. The parameters are given in Table 4.1 and Table 5.1.

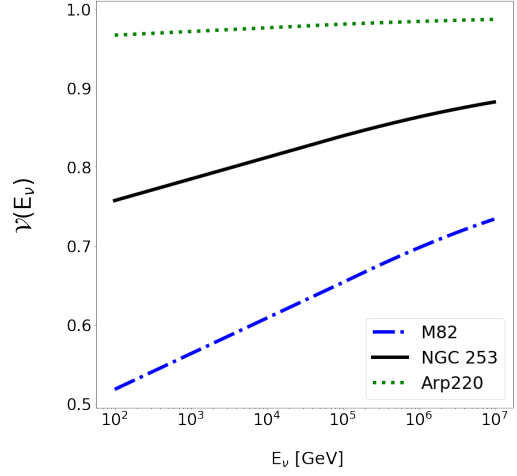


Figure 6.4: $\mathcal{V}(E_\nu)$ as function of neutrino energy E_ν for Arp 220, NGC 253, and M82 with the parameters given in Table 4.1 and Table 5.1.

6.2 Neutrino flux

The analytic expression of the neutrino-production rate in Equation 6.1 allows to write down an expression for the neutrino flux for a source at a given distance. Integrating the neutrino-production rate over the volume of the starburst region, which is assumed to be spherical, yields the dimensions of a neutrino luminosity. Therefore, in order to determine a neutrino flux measured at Earth, this luminosity should be divided by $4\pi D_L^2$, with D_L the luminosity distance to the source. Since it was assumed that the supernovae are homogeneously distributed in the starburst volume V_{SBR} , it follows that total expected neutrino flux at Earth is,

$$F_\nu(E, z) \equiv F_{\nu+\bar{\nu}}(E, z) = \frac{V_{SBR}}{4\pi D_L^2} \cdot q_\nu(E(1+z)) \quad [\text{GeV}^{-1} \text{ cm}^{-2} \text{ s}^{-1}], \quad (6.6)$$

which in the most general case is redshift dependent. However, the GOALS sample is located within the close Universe with the most distant source at $z = 0.0981$ (Chapter 3) and therefore the redshift effects can safely be neglected for our purposes.

Inelastic pp -interactions result in a neutrino flavor ratio at the source given by $(\nu_e : \nu_\mu : \nu_\tau) = (1 : 2 : 0)$. However, during the propagation over extragalactic distances neutrino oscillations will lead to an approximately equal distribution among the three neutrino flavors [84]. Therefore at Earth $(\nu_e : \nu_\mu : \nu_\tau) \approx (1 : 1 : 1)$. As a result the total neutrino flux in Equation 6.6 should be divided by a factor three in order to arrive at a single-flavor neutrino flux, such that

$$F_{\nu_j}(E_\nu, z) = \frac{V_{SBR}}{4\pi D_L^2} \cdot \frac{q_\nu(E(1+z))}{3} \quad \text{with } j \in \{e, \mu, \tau\}. \quad (6.7)$$

The muon neutrino flux $F_{\nu_\mu}(E)$ is of particular interest because of the good directional resolution of the related muon tracks in the IceCube detector (Section 2.2).

6.3 The power-law index

In Section 5.4 the analytic expression of the proton momentum distribution function allowed to identify the starburst-specific parameters required to fix this quantity in our model. All these parameters except the power-law injection index have been discussed (n_{ism} in Section 3.3.2, \mathcal{R}_{SN} in Section 4.5.2, p_{max} in Section 4.5.3, v_{gwind} in Section 5.2.2). However, now that the relation between the pion-production rate and the proton momentum distribution function has been discussed (Section 6.1) it is also possible to have a proper look at how α_{SN} can be inferred.

So far the focus in this work was on high-energy neutrino production from charged-pion decay with the charged pions produced in inelastic pp -interactions. Apart from charged pions these interactions also produce neutral pions which subsequently decay to gamma rays (Equation 2.5). Via observational gamma-ray data of starburst-driven galaxies it is in principle possible to derive α_{SN} . This claim is argued in what follows. A detailed discussion on gamma-ray production in U/LIRGs is however beyond the scope of this work and therefore the required expressions needed in this section are given without derivation but can be consulted in [76].

The gamma-ray injection rate can be expressed as,

$$q_\gamma(E_\gamma) = 2 \int_{E_{min}}^{\infty} \frac{q_\pi(E_\pi)}{\sqrt{E_\pi^2 - m_\pi^2 c^4}} dE_\pi, \quad (6.8)$$

which is related to the gamma-ray flux via,

$$F_\gamma(E_\gamma) = \frac{q_\gamma(E_\gamma)}{4\pi D_L^2} e^{-\tau_{\gamma\gamma}(E_\gamma, z)}. \quad (6.9)$$

The factor $\tau_{\gamma\gamma}$ is the optical depth taking into account pair production due to the interaction of gamma rays from the starburst with thermal-background photons during propagation in intergalactic space [61]. This allows to conclude that

$$F_\gamma \propto q_\gamma \propto q_\pi \underbrace{\propto}_{\text{Eq. 6.2}} p^2 Q_p \propto p^{-\alpha_{SN}+2}. \quad (6.10)$$

It must be noted that this will only be the case if $\tau_{\gamma\gamma}$ is not strongly energy dependent in the considered energy range. We therefore find that for a starburst region α_{SN} can be inferred by fitting gamma-ray production models to gamma-ray observations of the studied region. Due to the fact that gamma rays and neutrinos are produced simultaneously in inelastic pp -interactions, it follows that both q_ν and q_γ depend on the same proton injection rate Q_p and therefore the same spectral index α_{SN} . In conclusion, it is in principle possible to infer α_{SN} for neutrino-flux calculations from gamma-ray observations. Nevertheless, only a few sources in the GOALS samples have gamma-ray observations and therefore it is not possible to systematically determine this power-law index for the complete sample of GOALS objects. The effect of possible variations in the power-law index on the neutrino flux is discussed in more detail in Section 6.5.

6.4 Neutrino-flux computations

In order to calculate the single-flavor neutrino flux $F_{\nu_j}(E)$ as a function of energy, the integral in Equation 6.1 must be solved numerically. This integral requires as input the probability distribution functions $\mathcal{F}_i(x)$ shown in Figure 6.1 and the pion-production rate $q_\pi(E)$ of Equation 6.2. Fixing the pion-production rate requires the calculation of the proton momentum distribution function $f_p(p)$,

as given in Section 5.4. Given the neutrino-production rate, the single-flavor neutrino flux F_{ν_j} is found by taking into account the total volume of the considered starburst region V_{SBR} , the luminosity distance D_L to the galaxy, and the neutrino-oscillation factor $1/3$ (Equation 6.7). Therefore it can be concluded that the parameters needed to fix the single-flavor neutrino flux are,

$$F_{\nu_j} = F_{\nu_j}(R_{SBR}, n_{ism}, \mathcal{R}_{SN}, \alpha_{SN}, p_{max}, v_{gwind}, D_L) \quad j \in \{e, \mu, \tau\}. \quad (6.11)$$

The q_ν -code discussed in Section 6.1.1 is further extended to incorporate the expression in Equation 6.7. As such, the single-flavor neutrino flux can be computed for any nuclear starburst region in the GOALS sample upon input of the parameters in Equation 6.11. This code is referred to as the F_ν -code from now on. The ability to compute the starburst-driven neutrino flux from any nuclear starburst region upon input of 7 parameters, which all have been discussed in detail for U/LIRGs in terms of electromagnetic observables², is the main contribution of this work. This code is available on GitHub and will be maintained during future work [13]. The output of the F_ν -code for the muon neutrino flux of M82, NGC 253, and Arp 220, for which the required parameters are given in Table 6.1, is shown in Figure 6.5. It is noted that in the remainder of this work all fluxes will be scaled with E^2 and that $E_{\nu_\mu}^2 F_{\nu_\mu} \equiv E_{\nu_\mu + \bar{\nu}_\mu}^2 F_{\nu_\mu + \bar{\nu}_\mu}$.

Parameters	M82	NGC 253	ARP 220
\mathcal{R}_{SN} [yr ⁻¹]	0.050	0.027	2.25
$N_{C,SN}$ [(GeV/c) ⁻³ s ⁻⁴]	2.55×10^{42}	1.60×10^{42}	1.77×10^{44}
R_{SBR} [pc]	220	150	250
α_{SN}	4.25	4.30	4.45
p_{max} [PeV/c]	100	100	100
v_{gwind}	600	300	500
n_{ism} [cm ⁻³]	175	250	3500
D_L [Mpc]	3.9	3.8	77
$\sin(\delta)$	0.94	-0.43	0.40

Table 6.1: Parameters required to determine the muon-neutrino flux shown in Figure 6.5 for M82, NGC 253, and Arp 220. The values for \mathcal{R}_{SN} , R_{SBR} , α_{SN} , p_{max} , v_{gwind} , n_{ism} , and D_L are obtained from [61]. The sine of the declination $\sin(\delta)$ is given as well for the three galaxies which is required to compare with the IceCube sensitivity shown in Figure 2.6. The declination (δ) values are obtained from the NASA/IPAC Extragalactic Database [51]. The values for the normalisation constant are obtained from computations done following the derivation in Section 4.6.

Apart from the muon-neutrino fluxes, the IceCube E^{-2} point-source sensitivities at the declinations of M82, NGC 253, and Arp 220, taken from Figure 2.6, are shown as well in Figure 6.5. The energy

²The maximum attainable momentum is a special case in terms of electromagnetic observables but has been discussed in the context of U/LIRG starburst nuclei in Section 4.5.3.

range of these sensitivities corresponds to the 90 % central energy range that contributes to the sensitivity, acquired from [28]. However, the fact that the energy ranges for M82 and Arp 220 do not extend to PeV energies does not mean that IceCube is not sensitive for PeV neutrinos from these sources. The 90 % central energy ranges merely indicate where most of the signal is expected from simulations, given a source at the declination of M82 and Arp 220 with an E^{-2} neutrino spectrum. Lastly it is noted that the the neutrino spectra computed with our model for the three galaxies, indicated in Table 6.1, are slightly softer than the E^{-2} spectrum used to infer the point-source sensitivities.

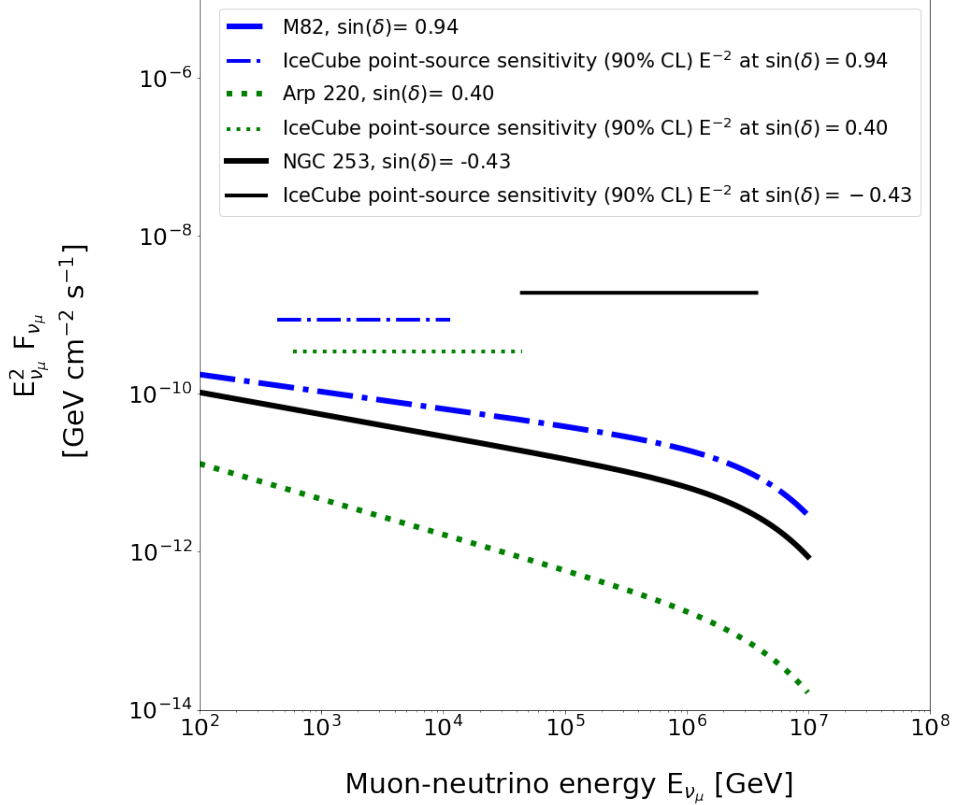


Figure 6.5: Muon-neutrino flux for M82, NGC 253, and Arp 220 using the model constructed in this work. The IceCube point-source sensitivities at 90% CL for an E^{-2} neutrino spectrum are shown as well, corresponding with the declinations of the three sources. These sensitivities are taken from Figure 2.6 and the corresponding energy ranges are acquired from [28] as explained in the text.

First, it can be concluded from Figure 6.5 that the the point-source sensitivity for NGC 253 is the poorest, which is expected since it is located in the Southern hemisphere while the other two sources are located in the Northern hemisphere (see Section 2.4). The fact that all the predicted neutrino fluxes are below the corresponding sensitivities is a valuable sanity check of our model since none of these galaxies have shown up in previous IceCube point-source analyses (Section 2.4). Second it is noted that the muon-neutrino flux for Arp 220 is consistently lower despite having a larger or comparable neutrino-production rate compared to NGC 253 and M82, as shown in Figure 6.2. This is due to the fact that Arp 220 is approximately 73 Mpc further away than M82 and NGC

253 (see Table 6.1), which results in a larger suppression of the neutrino flux.

6.4.1 Maximum attainable momentum

It was argued in Section 4.5.3 that for starburst-driven shock acceleration in U/LIRGs it is challenging to reach CR energies E_p which are able to explain the highest energies of the astrophysical neutrino flux, i.e. $E_p \simeq 50\text{-}100$ PeV. Until now the maximum attainable momentum in the exponential cutoff (see Equation 4.20) has been fixed to 100 PeV in all computations. Figure 6.6 shows the muon neutrino flux for NGC 253 and Arp 220 with various values of p_{max} down to 10 PeV. The results for M82 are not shown for the sake of readability of the plot and in any case would not add any new insights other than what is discussed in the following. First it can be concluded that even for $p_{max} = 10$ PeV, which is expected to be reached more naturally than 100 PeV for typical U/LIRG starburst conditions, the $E_{\nu_\mu}^2 F_{\nu_\mu}(E_{\nu_\mu})$ results do not significantly differ from the other p_{max} values up to $E_\nu \sim 200$ TeV. This indicates that the cumulative contribution of the starburst-driven neutrino production in the GOALS sample is more likely to contribute to the lower energy range of the observed IceCube flux.

It is noted that the high-energy tail of $E_{\nu_\mu}^2 F_{\nu_\mu}(E_{\nu_\mu})$ in Figure 6.6 should be interpreted carefully. Although the exponential cutoff $\exp(-p/p_{max})$ in the proton injection rate Q_p (Equation 4.20) is a reasonable assumption, it is not driven by observations. Next generation neutrino observatories will help to test the validity of this exponential cutoff.

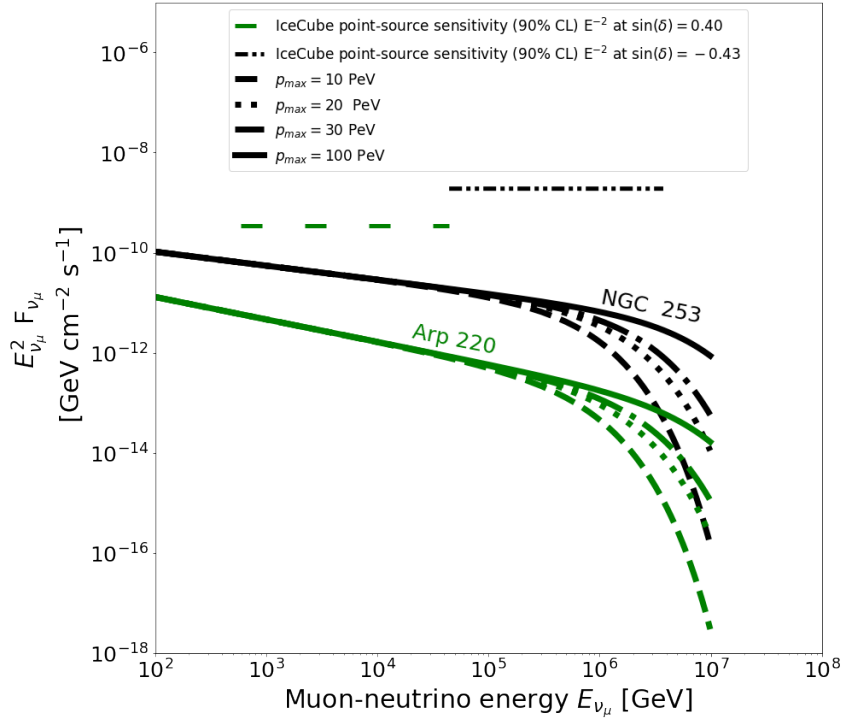


Figure 6.6: Muon-neutrino flux for NGC 253 and Arp 220 for different p_{max} values down to 10 PeV. The IceCube point-source sensitivities at 90% CL for an E^{-2} neutrino spectrum are given as well, corresponding with the declinations of NGC 253 and Arp 220 .

6.4.2 Varying galactic superwind speed, supernova rate, and ISM density

In Section 5.2.2 the multi-phase galactic-scale outflow was discussed. For the cold phases in this galactic superwind a speed of the order of ~ 100 km/s is observed and for the hot phases a few 1000 km/s is inferred, mainly from simulations. However, it is not clear which phase is relevant for the advection of CRs. Therefore we discussed the effect of both phases on the secondary-particle production in (non-)U/LIRG starburst nuclei by means of the equilibrium wind speed (Section 5.3.3). We concluded for non-U/LIRG starburst nuclei that especially the hot phases could significantly reduce the production of secondary particles. For typical U/LIRG conditions on the other hand it was concluded that even the highest galactic superwind speeds will not affect the secondary-particle production significantly.

The v_{gwind} values indicated in Table 6.1 are consistent with the cold phases of the galactic-scale outflow. Therefore we now study the effect of a v_{gwind} value consistent with the hot phases of the superwind. In Figure 6.7 flux results are shown for M82, NGC 253, and Arp 220 all with $v_{gwind} = 2000$ km/s while keeping all other parameters of Table 6.1 fixed. Figure 6.7 also shows the results of Figure 6.5 for comparison.

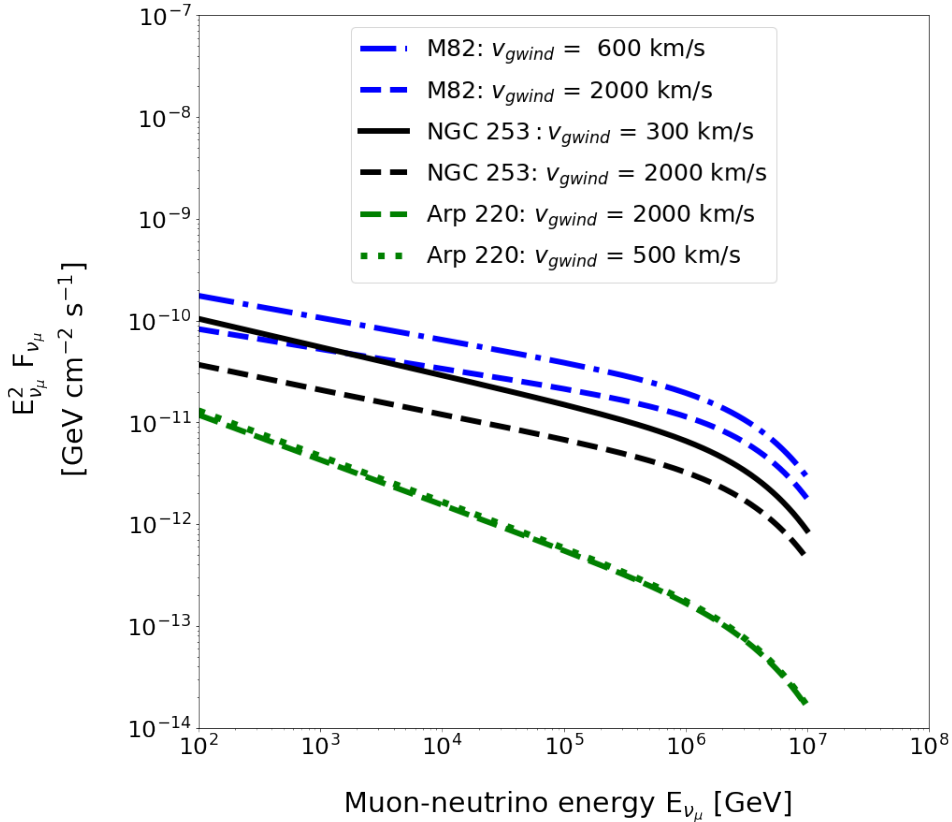


Figure 6.7: Muon-neutrino fluxes for M82, NGC 253, and Arp 220, each with a galactic superwind speed of $v_{gwind} = 2000$ km/s and the other required parameters to fix F_{ν_μ} as indicated in Table 6.1. The flux results of Figure 6.5, using the velocities specified in Table 6.1, are shown as well for comparison. It is noted that the flux results of Arp 220 for both wind speeds practically coincide.

This allows to conclude that the effect of an increased galactic superwind speed is indeed the most significant for non-U/LIRGs while for ULIRGs the effect is likely negligible.

In Figure 6.8 the effect of changes in the SN rate on the muon-neutrino flux is shown by highlighting the region between half and twice the SN rate of each of the sources given in Table 6.1. All other parameters remain fixed. In addition the flux results of Figure 6.5 are shown for comparison.

We conclude from Figure 6.8 that taking twice (half) the value of the SN rate results in a neutrino flux that is also doubled (halved). This moderate effect has the strongest implications for the ULIRGs in the GOALS sample which are typically located at higher distances, and hence suffer from a larger distance-squared suppression in the neutrino flux (Equation 6.7). For example, Arp 220 is the closest ULIRG at $D_L = 77$ Mpc ($z = 0.01813$) [51], while the second-closest ULIRG, WKK 2031, is already located at $D_L = 139$ Mpc ($z = 0.03076$) [51]. In addition, the predicted flux of Arp 220 lies below the predictions for M82 and NGC 253 by about an order of magnitude, even using twice the SN rate. Since the SN rate of Arp 220 is likely indicative for the SN rate in ULIRGs, and because of their larger distance to Earth, ULIRGs are unlikely to be observed as single point sources by IceCube with its current sensitivity. We note that this interpretation only applies to the starburst-driven neutrino flux, and does not take into account a possible contribution from an AGN.

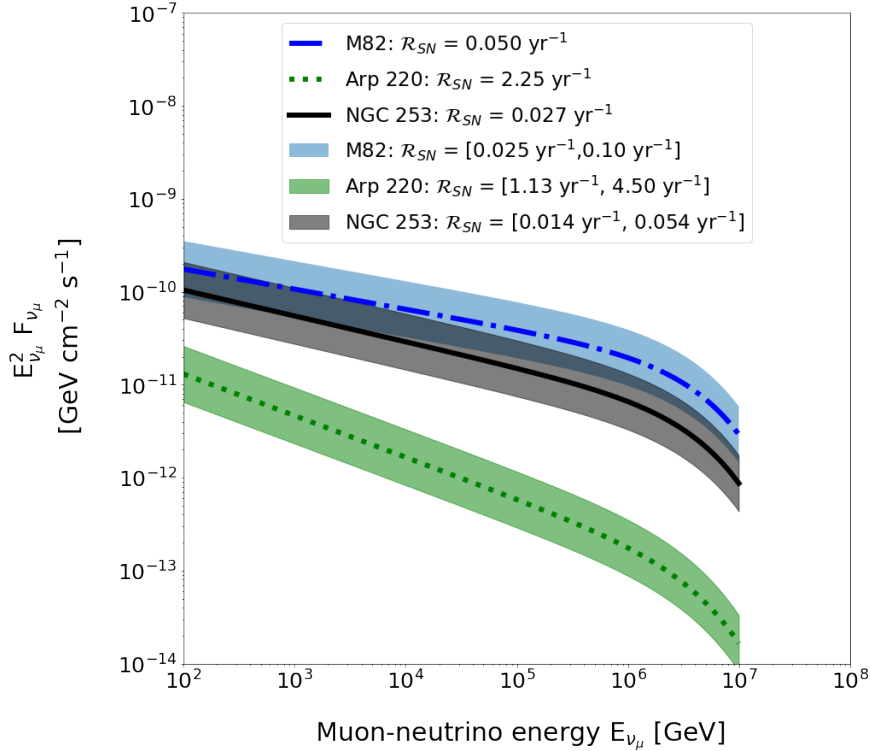


Figure 6.8: Muon-neutrino fluxes for M82, NGC 253, and Arp 220. The bands shown for M82, NGC 253, and Arp 220 range from half to twice the \mathcal{R}_{SN} value in Table 6.1 with all other parameter values in the table kept constant. The flux results of Figure 6.5 are also shown for comparison.

In Figure 6.9 the dashed lines show the muon-neutrino flux for M82, NGC 253, and Arp 220

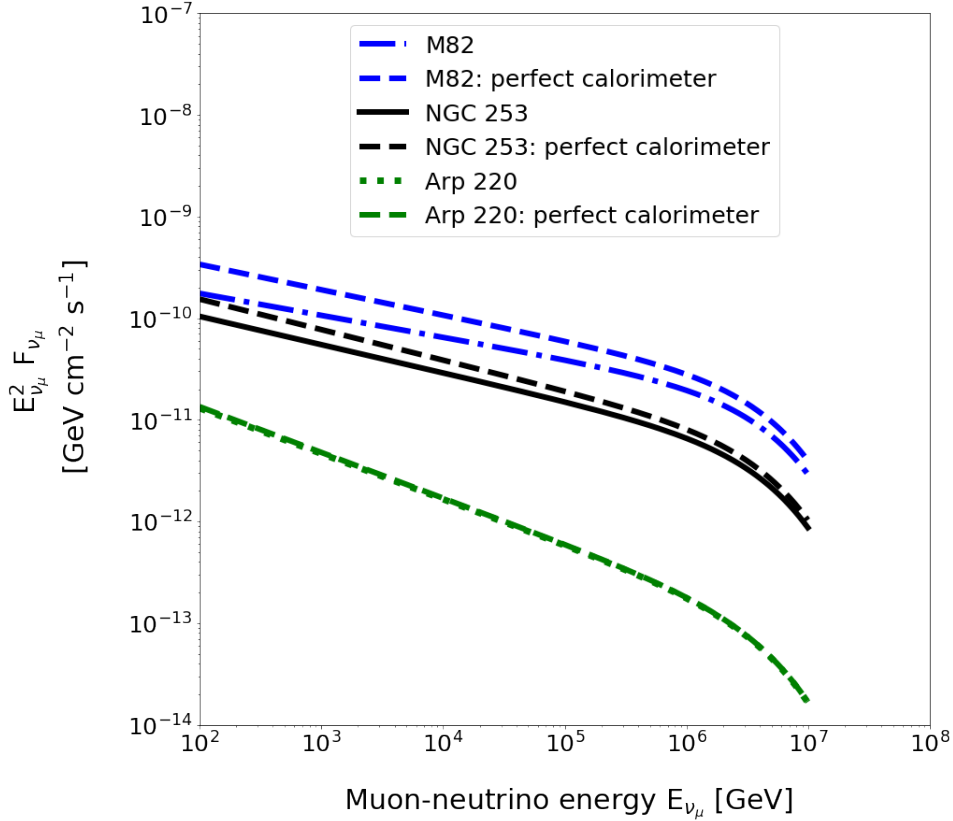


Figure 6.9: Muon-neutrino flux for M82, NGC 253, and Arp 220 as perfect calorimeters obtained by using the values in Table 6.1 but with $n_{ism} \rightarrow \infty$. The results in Figure 6.5 are shown for comparison. It is noted that for Arp 220 the flux results from Figure 6.5 and the perfect calorimeter flux results practically overlap.

based on the values given in Table 6.1, except for the ISM density which has been taken to infinity. This is done in order to make perfect calorimeters of the sources (see Section 5.3). In addition the results from Figure 6.5 are shown for comparison. It is concluded that M82 shows the most significant increase, as is expected from the $\mathcal{V}(E_\nu)$ analysis in Figure 6.4. Moreover, for Arp 220 the increase in muon-neutrino flux is barely noticeable as is also expected from the same $\mathcal{V}(E_\nu)$ analysis in Figure 6.4.

It is noted that the effect on the neutrino flux due to varying the spectral index was not studied yet. A detailed discussion on this is postponed to next section when discussing the neutrino flux predictions of Arp 299-A.

6.5 Neutrino-flux computations of Arp 299

Having developed our model and set up our simulation code it is now possible to predict the starburst-driven (single-flavor) neutrino flux for any given GOALS object, as discussed previously. In this section the neutrino-production framework is applied to a particular GOALS object, Arp

299, in order to obtain the first prediction of the starburst-driven neutrino flux of this source.

In Section 3.3.3 we focused on the wide variety of LIRG morphologies, which range from single galaxies to minor/major merging systems that are observed over different epochs of the merging process. It was concluded that in an interacting system there can be a significant separation between the nuclear regions of the galaxies taking part in the merger and correspondingly a significantly different stellar and/or AGN activity. This lead us to conclude that a well-resolved nuclear structure is crucial to constrain the neutrino production in LIRGs. We searched the GOALS sample for a LIRG with such a well-resolved nuclear structure and came across the LIRG Arp 299 (Section 3.3.5). Although Arp 299 has various active regions, only the conditions of nuclear region Arp 299-A (Figure 3.7) are of interest in this work. This due to the fact that the largest starburst activity coincides with Arp 299-A, which is also the most compact region. In the nuclear region on the other side of the galaxy (region B1, Figure 3.7) significant AGN activity is detected which is obscured by Compton-thick column densities. A Compton-thick AGN could be a second gamma-ray obscured source of neutrinos, as was discussed in Chapter 1. Such an AGN contribution falls beyond the scope of this work, but will be investigated in follow-up studies. The rest of the galaxy also shows signs of starburst activity, although the average ISM density of the galaxy is considerably lower than in a starburst nucleus, such that diffusion effects might be significant.

As such the F_ν -code will be applied to the LIRG Arp 299-A. In the next paragraphs the required parameters for the muon-neutrino flux, indicated in Equation 6.11, are briefly discussed for Arp 299-A and the corresponding values are given in Table 6.2.

Supernova rate and radius starburst region Arp 299-A is characterized as a highly dust-enshrouded region to a degree that even near-IR wavelengths suffer of attenuation effects. Therefore the only way to identify the SN activity in this region is by means of high-resolution radio observations. The best observational constraints of the SN activity in the the central $R_{SBR} \approx 150$ pc [56] of Arp 299-A were revealed by a ~ 2.5 year monitoring campaign at 5.0 GHz. This resulted in a lower limit of $\mathcal{R}_{SN} \gtrsim 0.8 \text{ yr}^{-1}$ on the core-collapse SN rate.

Galactic superwind speed LOFAR observations at 150 MHz have revealed a two-sided, wide filamentary structure emanating from the A-nucleus of Arp 299 [59]. The outflow is detected at these radio wavelengths since it transports synchrotron-emitting electrons and almost the whole of its structure is unaffected by absorption. It was estimated in [59] that the outflow moves at $\sim 370\text{-}890 \text{ km s}^{-1}$, under the assumption that the outflow is driven by a supernova rate of $\mathcal{R}_{SN} \gtrsim 0.8 \text{ yr}^{-1}$ in the central ≈ 150 pc.

ISM density Although most of the regions in Arp 299 show typical starburst properties (Figure 3.7), only the A nucleus exhibits the characteristics of a LIRG with an ISM density of $n_{ism} = 1\text{-}5 \times 10^3 \text{ cm}^{-3}$ [82].

Power-law index Since no spectral models have been fitted to multiwavelength observations of Arp 299-A, there exist no constraints for the power-law index α_{SN} . Therefore two values will be considered for Arp 299-A in this work, i.e. $\alpha_{SN} = 4.20$ and $\alpha_{SN} = 4.45$. The former could be interpreted as an M82-like α_{SN} while the latter is more an Arp 220-like α_{SN} (Table 4.1).

From Table 6.2 we observe that the ISM density n_{ism} and the galactic superwind velocity v_{gwind} are only loosely constrained. Therefore it is instructive to first analyse the \mathcal{V} parameter introduced

Parameters	Arp 299-A
\mathcal{R}_{SN} [yr ⁻¹]	$\gtrsim 0.80$
$N_{C,SN}$ [(GeV/c) ⁻³ s ⁻¹]	$(4.08-6.30) \times 10^{43}$
R_{SBR} [pc]	150
α_{SN}	4.20-4.45
p_{max} [PeV/c]	100
v_{gwind}	370-890
n_{ism} [cm ⁻³]	1000-5000
D_L [Mpc]	44.80
$\sin(\delta)$	0.85

Table 6.2: Parameters required to determine the muon-neutrino flux shown in Figure 6.11. The values for \mathcal{R}_{SN} , R_{SBR} , v_{gwind} , n_{ism} , and D_L are obtained from the literature, as discussed in the text. The values for the normalisation constant $N_{C,SN}$ corresponding to $\alpha_{SN} = 4.20$ and $\alpha_{SN} = 4.45$ are obtained from computations done in this work following the derivation in Section 4.5.1. The declination (δ) values are obtained from the NASA/IPAC Extragalactic Database [51].

in Equation 6.5. The results for $\mathcal{V}(E_\nu, n_{ism}, v_{gwind})$ as a function of neutrino energy are shown in Figure 6.10 for Arp 299-A. These results were obtained from the q_ν -code (Section 6.1.1). The largest neutrino-production rate corresponds to the slowest wind and the largest ISM density, while for the smallest neutrino-production rate it is the other way around. This is within expectations. In any case, Arp 299-A appears to be a good calorimeter for all parameter combinations, as is expected from the discussion in Section 5.3.

However, there is a notable difference between the case with $v_{gwind} = 370$ km/s and $n_{ism} = 5000$ cm⁻³, referred to as case 1 from now on, and the case with $v_{gwind} = 890$ km/s and $n_{ism} = 1000$ cm⁻³, referred to as case 2 from now on. Therefore the neutrino flux will be determined for both case 1 and case 2. As the SN rate given in Table 6.2 is a lower limit, the muon-neutrino flux will also be investigated for a case 1 scenario but with twice the SN rate, i.e. $\mathcal{R}_{SN} = 1.60$ yr⁻¹. This scenario is referred to as case 3 from now on.

Last it is concluded from Figure 6.10 that in case the ISM density is severely underestimated and would be larger than 5000 cm⁻³, the neutrino-production rate would not differ significantly from the rate computed for $n_{ism} = 5000$ cm⁻³ in combination with any of the two galactic superwind speeds.

The results for the muon-neutrino flux of Arp 299-A corresponding to the three cases and the two investigated spectral indices, acquired from the F_ν -code upon input of the values in Table 6.2, are shown in Figure 6.11. In addition the IceCube point-source sensitivity for a source at the declination of Arp 299-A is shown for an E^{-2} spectrum. This point-source sensitivity was obtained

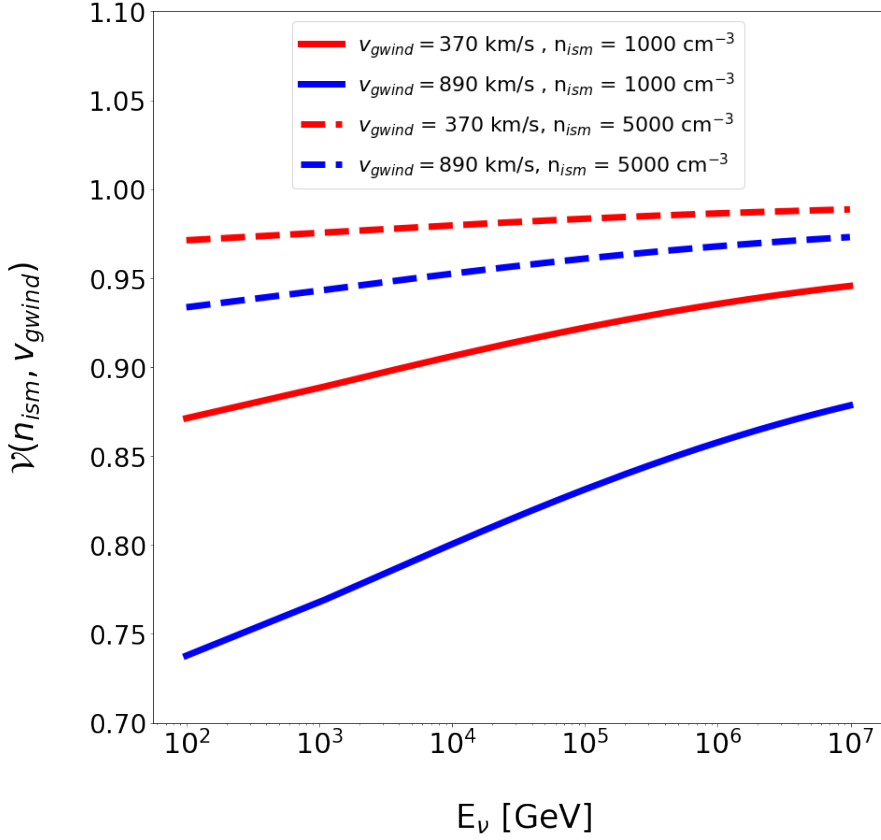


Figure 6.10: $\mathcal{V}(E_\nu, n_{ism}, v_{gwind})$ as function of neutrino energy E_ν for Arp 299-A. We show this for several combinations of the galactic superwind speed v_{gwind} and ISM density n_{ism} , as discussed in the text. This plot was obtained using computations of the q_ν -code discussed in Section 6.1.1.

from Figure 2.6.

First it is concluded that changes in the spectral index α_{SN} have a significant impact on the flux results. This can be concluded by selecting any of the three cases in Figure 6.11 and compare the flux results for the two spectral indices considered. The effect of the spectral index is also highlighted by comparing case 1 with $\alpha_{SN} = 4.20$ and case 3 (which is case 1 but with twice the value of \mathcal{R}_{SN}) with $\alpha_{SN} = 4.45$. This shows that even for $\mathcal{R}_{SN} = 1.60 \text{ yr}^{-1}$ the flux values still end up well below the results for $\mathcal{R}_{SN} = 0.80 \text{ yr}^{-1}$ with a harder spectral index $\alpha_{SN} = 4.20$. The isolated effect of a larger SN rate can be studied by comparing the results of case 1 and case 3 for a fixed α_{SN} value. We conclude that changes in the SN rate will affect the flux results less significantly compared to variations of the spectral index.

The fact that for a fixed spectral index α_{SN} the flux result of case 1 are slightly larger than the results of case 2 follows directly from Figure 6.10.

Last it is noted from Figure 6.11 that for all choices of parameters the predicted fluxes are below the IceCube point-source sensitivity for a source at the declination of Arp 299. This is expected since this LIRG has not shown up in previous IceCube point-source searches (Section 2.4).

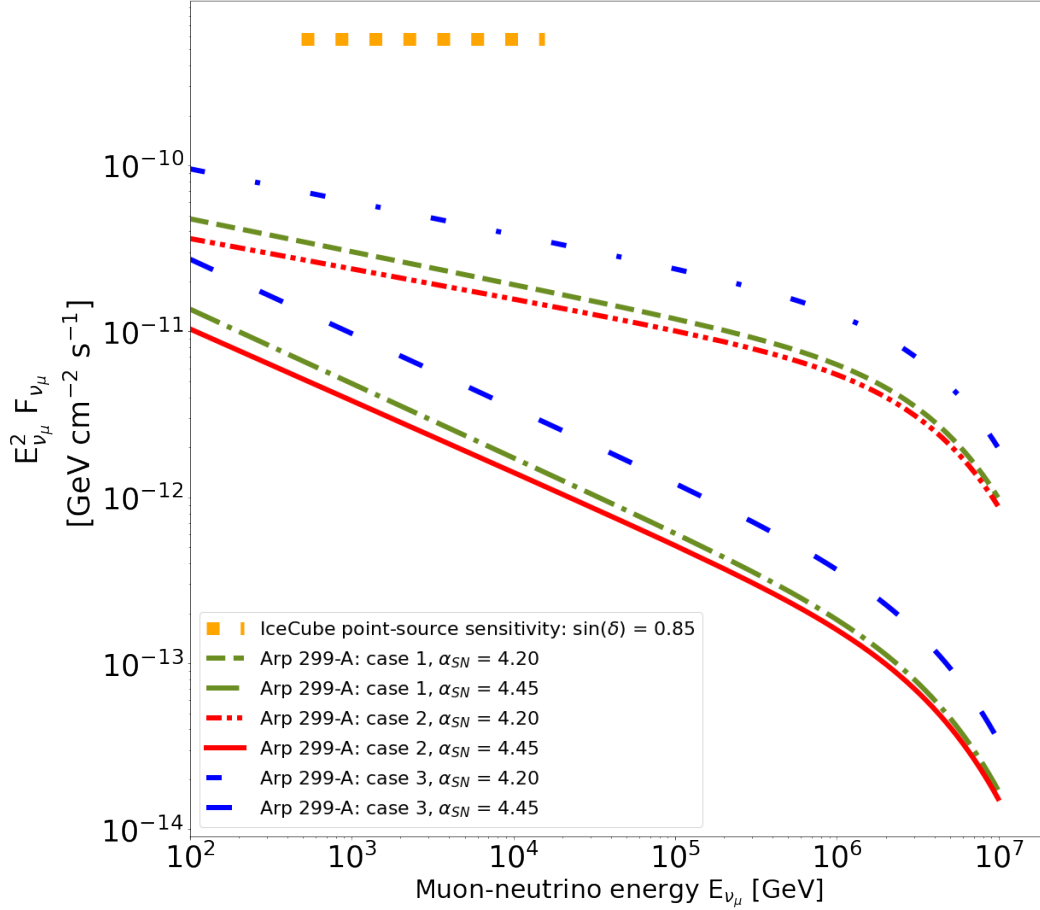


Figure 6.11: Predictions of a muon-neutrino flux of Arp 299-A using our model, which are compared to the E^{-2} IceCube sensitivity for a point source at the declination of Arp 299 (gold dotted). The results are shown for case 1: $v_{gwind} = 370$ km/s and $n_{ism} = 5000$ cm^{-3} and case 2: $v_{gwind} = 890$ km/s and $n_{ism} = 1000$ cm^{-3} . Both case 1 and case 2 are shown for $\alpha_{SN} = 4.20$ and $\alpha_{SN} = 4.45$. Case 3, which is case 1 but with the SN rate doubled, is shown as well for both α_{SN} values.

Chapter 7

Conclusion and outlook

Conclusion

The IceCube Neutrino Observatory at the South Pole is a 1 km³ neutrino detector searching for high-energy neutrinos of astrophysical origin. In 2013 the IceCube Collaboration confirmed for the first time the existence of a diffuse high-energy neutrino flux. Over the years several independent IceCube analyses have measured and characterized this diffuse flux. Nevertheless, at the time of writing the origin of this neutrino flux remains largely unknown. However, diffuse observations of astrophysical neutrinos and gamma rays reveal that there is a deficit in the amount of observed gamma-rays by Fermi-LAT given the amount of observed neutrinos by IceCube. This tension could be resolved if the sources of neutrinos are gamma-ray dim, obscured by large amounts of dust and gas. In these so-called hidden sources neutrinos are efficiently produced while gamma rays can be attenuated.

In this thesis we studied the neutrino production in (ultra)-luminous infrared galaxies. Such galaxies are characterized by IR luminosities exceeding $10^{11} L_{\odot}$, indicating the presence of both large amounts of obscuring matter and an enormous energy budget. More precisely we focused on U/LIRGs in the Great Observatories All-Sky LIRG Survey (GOALS), which provides extensive data over the whole electromagnetic spectrum for ~ 200 nearby U/LIRGs. A high-energy neutrino production framework was constructed for starburst-driven U/LIRGs in which neutrinos are produced via inelastic pp -interactions. A summary of this open-source framework is given in Figure 7.1, and below we present the conclusions and outlook of our study.

In Chapter 4 an analytic expression was derived for the proton injection rate Q_p resulting from core-collapse supernovae in nuclear starburst regions. We concluded that the required parameters to compute the proton injection rate are the radius of the starburst region R_{SBR} , the spectral power-law index α_{SN} , the supernova rate \mathcal{R}_{SN} , and the maximum achievable momentum p_{max} of the studied accelerator class. In particular, we studied how these parameters are related to the electromagnetic observables of (non)-U/LIRG starbursts.

A numerical code was implemented which allows to compute the proton injection rate based on the starburst-specific parameters mentioned above. This code is referred to as the Q_p -code. It has been shown that the Q_p -code is able to reproduce the results of [62].

In Chapter 5 we related the proton injection rate Q_p to the steady-state proton momentum distribution function f_p from first principles in the context of nuclear starburst regions. We concluded

that for a compact starburst region in which supernovae are homogeneously distributed, and which do not show signs of temporal variability in their electromagnetic output, the proton momentum distribution function is equal to the product of the proton injection rate and the total lifetime τ_{life} of the cosmic ray within the considered region, i.e. $f_p = \tau_{life} Q_p$. We identified that this lifetime depends on diffusion in magnetic fields, advection via galactic-scale outflows, and inelastic pp -interactions.

We showed through a timescale comparison that diffusion effects have a minor effect on the transport of protons in non-U/LIRG nuclear starburst regions. In addition, we argued that diffusion effects are suppressed even more in compact starburst regions of U/LIRGs as these are more turbulent versions of the non-U/LIRG variants with a significantly larger ISM density n_{ism} . Based on this we concluded that omitting diffusion effects in the computation of τ_{life} does not affect the neutrino-flux computations done in this work.

In order to quantify the effect of cosmic-ray advection via the galactic superwind in both non-U/LIRG and U/LIRG starburst nuclei, we introduced the concept of the equilibrium wind speed. This is the galactic superwind speed required to achieve equal timescales over which inelastic pp -scatterings and advection occur in the nuclear starburst region. We concluded that for non-U/LIRG starburst nuclei, especially the hot phases in the galactic superwind, moving at a ~ 1000 km/s, are of the order of the average equilibrium wind speed. If hot phases are responsible for the advection of cosmic rays, then a significant amount of these cosmic rays could be removed from the nuclear starburst region before being converted to high-energy neutrinos. For typical U/LIRG conditions on the other hand, we found that even the highest galactic superwind speeds v_{gwind} are well below the average equilibrium wind. Based on this we concluded that the galactic-scale outflow will not significantly affect the secondary-particle production in U/LIRGs.

The analytic expressions of the discussed timescales were translated to a numerical code, which was combined with the Q_p -code in order to compute the proton momentum distribution function f_p . This so-called f_p -code requires the ISM density n_{ism} and the galactic superwind speed v_{gwind} in addition to the starburst-specific parameters used as input for the Q_p -code.

In Chapter 6 the proton momentum distribution function was related to the pion-production rate $q_\pi(E)$ which on its turn was related to the neutrino-production rate $q_\nu(E)$ via probability distribution functions describing the decay of charged pions. These expressions were used to extend the f_p -code in order to compute the neutrino-production rate. This so-called q_ν -code was used to interpret the behaviour of the neutrino-production rate in both non-U/LIRG and U/LIRG environments.

The q_ν -code was further extended by taking into account the volume of the starburst region and the distance to the host galaxy. This finalized the modeling effort of this work and resulted in a code which is able to compute the starburst-driven neutrino flux for any nuclear starburst region in the GOALS sample upon input of the distance to the host galaxy and the starburst-specific parameters mentioned above. The ability to predict such a neutrino flux from a nuclear starburst region upon input of 7 parameters, all argued in terms of electromagnetic observables, is the main contribution of this work and is referred to as the F_ν -code. This code is available on GitHub and will be maintained for future studies [13].

The muon-neutrino flux was computed for M82 and NGC 253, both non-U/LIRG starburst galaxies, as well as for the ULIRG Arp 220 using the model constructed in this work. These fluxes were found to be below the IceCube point-source sensitivities at the corresponding declinations for an E^{-2} neutrino spectrum. This is expected as none of these galaxies have shown up in previous IceCube analyses. However, M82 was found to be relatively close to its corresponding sensitivity and is therefore a potentially interesting target for future dedicated point-source studies.

We also tested the effect of varying isolated model parameters in the flux predictions of M82, NGC 253, and Arp 220. First the effect of different p_{max} values was studied. In order to explain the highest PeV neutrino energies observed by IceCube, U/LIRG starburst regions should be able to accelerate protons to 50-100 PeV. Although not impossible, the average p_{max} will most likely be lower in starburst nuclei. By studying the effect of different p_{max} values between 10 and 100 PeV on the flux results of Arp 220, we concluded that the cumulative contribution of the starburst-driven neutrino emission from GOALS objects would most likely only contribute to the diffuse IceCube neutrino flux below ~ 200 TeV.

The effect on the flux results by halving and doubling the value of the supernova rate was studied as well. It was concluded that this only yields a moderate decrease/increase in neutrino flux. Based on the fact that ULIRGs in the GOALS sample are expected to have a comparable supernova rate to Arp 220, the closest ULIRG, but are located at higher distances compared to most LIRGs in the sample, we argued that none of the GOALS ULIRGs are expected to be observed as point sources by IceCube.

By comparing flux results for galactic superwind speeds consistent with hot phases (~ 1000 km/s) and cold phases (~ 100 km/s) in the wind, respectively, a notable flux decrease was observed for M82 and NGC 253, which are both non-U/LIRG starburst galaxies. For the ULIRG Arp 220 on the other hand no notable difference was observed. This is consistent with our findings from the equilibrium-wind discussion above.

Last the effect of assuming perfect calorimeter conditions for the three galaxies was studied. In this work the quantity $\mathcal{V} \in [0, 1]$ was introduced which is the fraction of the neutrino-production rate over the same neutrino-production rate but with the ISM density taken to infinity. Therefore \mathcal{V} quantifies to which degree perfect calorimetric conditions are obtained, with $\mathcal{V} = 1$ a perfect calorimeter. The behaviour of \mathcal{V} as function of energy was studied for M82, NGC 253, and Arp 220 which showed that NGC 253 and Arp 220 approach full calorimetric scenarios while M82, especially at the lowest energies, does not. This was also confirmed by comparing the flux results of M82, NGC 253, and Arp 220 to the flux results of these sources as perfect calorimeters.

In the last part of this work we made the very first prediction of a starburst-driven neutrino flux for the GOALS LIRG Arp 299. The knowledge acquired in this work allowed to select the appropriate electromagnetic data for the starburst-specific parameters required to compute the neutrino flux. However, since no spectral models have been fitted to multiwavelength observations of Arp 299-A, there exist no constraints for the power-law index α_{SN} . Therefore we opted for an M82-like α_{SN} and an Arp 220-like α_{SN} . Moreover, we concluded that the galactic superwind speed v_{gwind} and ISM density n_{ism} of Arp 299-A are only loosely constrained. As such a \mathcal{V} -analysis was performed to study the effect of different combinations of these parameters on the neutrino production, where we identified three interesting combinations.

These parameter combinations were used as input in the F_ν -code to compute this neutrino flux for Arp 299-A. Comparing the flux results of different α_{SN} values showed that the neutrino flux is sensitive to changes of this parameter. Moreover it was concluded that all the parameter combinations resulted in a flux below the IceCube point-source sensitivity of a source at the declination of Arp 299-A.

Outlook

Having developed the framework discussed in this work, the next step is to make a neutrino-flux prediction for every source in the GOALS sample. Furthermore, we will make a prediction of the stacked contribution of all GOALS objects to the diffuse neutrino flux, where we will investigate different weighting schemes for a foreseen IceCube stacking analysis. Both the individual-source and stacked predictions will be tested by performing a dedicated IceCube analysis on the sources in the GOALS catalogue. Moreover, this will be the first analysis searching for neutrinos from LIRGs, such that we will be able to provide the first measurements or constraints from neutrino emission from this source class.

In a next step we will investigate the contribution of obscured AGN activity to the neutrino production in GOALS sources. A first target will be Arp 299, which is a merging system containing two active nuclear regions. For the nuclear region Arp 299-A we made the first prediction of a starburst-driven neutrino flux in this work. However, in the context of AGN-driven neutrino production, the nuclear region on the other side of the system, Arp 299-B, is of interest as it contains an AGN which is obscured by Compton-thick column densities. Such Compton-thick AGN are interesting obscured-source candidates of high-energy neutrinos. Finally, our existing framework will be extended in order to account for a possible obscured-AGN contribution to the neutrino flux of U/LIRGs, particularly in the context of GOALS sources. Consequently, we will also be able to test these predictions with the IceCube analysis mentioned above.

F_ν -code

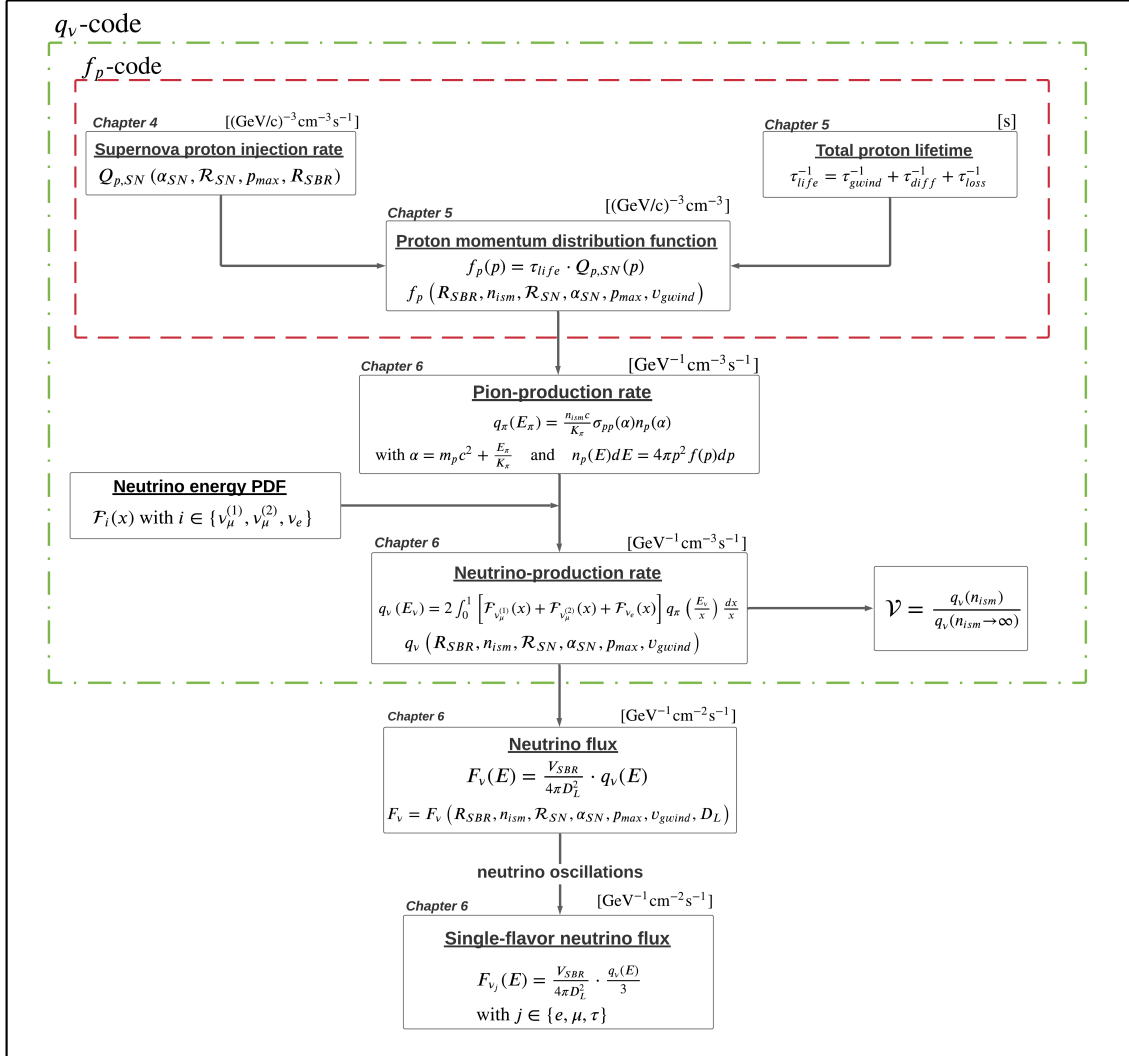


Figure 7.1: Scheme showing the relation between the parameters required to determine the neutrino flux within the framework developed in this work.

Appendix A

Average energy gain in first order Fermi acceleration

Given the setup in Figure 4.4, a relativistic charged particle with energy E_1 is considered in the reference frame of the upstream plasma. Performing the appropriate Lorentz transformation, the energy in the downstream region E'_1 can be found

$$E'_1 = \gamma(E_1 - p_x v) = \gamma E_1 (1 - \beta \cos \theta_1), \quad (\text{A.1})$$

with $\beta = V_p/c$. The shocks of interest in this work are mainly those induced by SN ejecta, with $V_p \sim 10000$ km/s, and therefore $\beta \ll 1$. Moreover, due to the charged particle being relativistic, it follows that $E = pc$ with $p_x = p \cdot \cos \theta_1$.

The particle in the downstream plasma will again scatter on the magnetic instabilities there, randomising the velocity vector and eventually recrossing the shock back to the upstream region. It is noted that not all particles will re-cross the shock but for now the focus is on those who do. The energy of the particle right after the last scattering before re-crossing the shock back to the upstream plasma is E'_2 and makes an angle θ'_2 with the normal to the shock. Due to the fact that the magnetic field fluctuations are frozen into the plasma and magnetic fields cannot do work, it follows that $E'_2 = E'_1$. Performing a Lorentz transformation back to the original upstream rest frame

$$E_2 = \gamma E'_2 (1 + \beta \cos \theta'_2), \quad (\text{A.2})$$

which allows to determine the fractional energy gain after one cycle

$$\begin{aligned} \frac{\Delta E}{E} &= \frac{E_2 - E_1}{E_1} \\ &= \frac{\gamma E'_2 (1 + \beta \cos \theta'_2) - \frac{E'_1}{\gamma(1 - \beta \cos \theta_1)}}{\frac{E'_1}{\gamma(1 - \beta \cos \theta_1)}} \\ &= \gamma^2 (1 + \beta \cos \theta'_2)(1 - \beta \cos \theta_1) - 1 \\ &= \frac{1}{1 - \beta^2} \left((1 + \beta \cos \theta'_2)(1 - \beta \cos \theta_1) \right) - 1 \\ &= \frac{\beta^2 + \beta \cos \theta'_2 - \beta \cos \theta_1 - \beta^2 \cos \theta_1 \cos \theta'_2}{1 - \beta^2}. \end{aligned} \quad (\text{A.3})$$

The probability $p(\theta)$ particles following an isotropic distribution cross the shock within the angles θ to $\theta + d\theta$ is proportional to $\sin(\theta)d\theta$. Moreover, the rate at which they approach the shock front is proportional to the x-component of their velocities, i.e. $c \cos(\theta)$ and thus the probability of the particle crossing the shock is proportional to $\sin(\theta)\cos(\theta)d\theta$. Appropriately normalising results in $p(\theta) = 2\sin(\theta)\cos(\theta)d\theta$. From this it follows that $\langle \cos(\theta_2) \rangle = 2/3$ for the particles moving from downstream to upstream and $\langle \cos(\theta_1) \rangle = -2/3$ from upstream to downstream. Applying these averages in Equation A.3 allows to determine the average fractional energy gain

$$\left\langle \frac{\Delta E}{E} \right\rangle = \frac{\beta^2 + \frac{2}{3}\beta + \frac{2}{3}\beta - \frac{4}{9}\beta^2}{1 - \beta^2} \approx \frac{4}{3}\beta, \quad (\text{A.4})$$

where in the last step the non-relativistic shock approximation was invoked. In conclusion the average energy gain after one cycle, meaning shocking the front back and forth, is

$$\left\langle \frac{\Delta E}{E} \right\rangle_{cycle} = \frac{4}{3} \frac{V_p}{c} = \frac{V}{c} \quad (\text{one cycle}). \quad (\text{A.5})$$

The name first order Fermi acceleration refers to the fact that the increase in energy goes as $\Delta E/E \propto V/c$, in contrast to second order Fermi acceleration, where $\Delta E/E \propto (V/c)^2$.

Appendix B

Supernova rate in U/LIRGs: the initial mass function approach

The supernova rate is a crucial parameter to compute the neutrino flux from a starburst-driven galaxy such as U/LIRGs. As the error on the SN rate will propagate to the neutrino flux, this SN rate is required to be as constrained as possible. Therefore the best option is to use SN rates inferred from dedicated SN-activity campaigns. Unfortunately, the minority of the sources in the GOALS sample have such dedicated observations. For these sources the literature provides an alternative to estimate the SN rate based on the initial mass function and star-formation rate in the starburst region. Typically the literature quotes the relation between the supernova rate, the initial mass function, and star-formation rate without derivation. In this appendix we derive this relation from basics and interpret it in context of U/LIRGs.

The IMF $\zeta(m)$ is the function describing the mass distribution for a population of stars at formation time. This means that $\zeta(m)dm$ is the number of masses in the range m and $m + dm$ within a pre-defined volume of space. It is very challenging to predict the IMF theoretically. However, the IMF determined from observations is remarkably universal in a wide range of environments and is well-described by a canonical power-law $\zeta(m) \propto m^{-\alpha}$. The IMF of stars more massive than the Sun was first quantified by Edwin Salpeter in 1955 [85]. His work favoured an exponent of $\alpha = 2.35$ and is referred to as the Salpeter IMF,

$$\zeta_{Salpeter}(m) \propto m^{-2.35}. \quad (\text{B.1})$$

Pavel Kroupa (2001) kept $\alpha = 2.3$ above $0.5 M_{\odot}$, but introduced $\alpha = 1.3$ between 0.08 - $0.05 M_{\odot}$ and $\alpha = 0.3$ below $0.08 M_{\odot}$ [86],

$$\zeta_{Kroupa}(m) \propto m^{-\alpha} : \begin{cases} \alpha = 0.3 & \text{for } m/M_{\odot} < 0.08 \\ \alpha = 1.3 & \text{for } 0.08 < m/M_{\odot} < 0.05 \\ \alpha = 2.3 & \text{for } m/M_{\odot} > 0.5. \end{cases} \quad (\text{B.2})$$

Although that the Salpeter- and Kroupa-IMF are frequently used IMFs, others are used as well in the literature.

If m_{min} and m_{max} are respectively the mass of the lightest and most massive star at formation time, then the total mass corresponding to the initial distribution described by $\zeta(m)$ can be expressed as

$$M_{total} = \int_{m_{min}}^{m_{max}} m\zeta(m)dm \quad [M_{\odot}]. \quad (\text{B.3})$$

The number of stars in that same initial distribution which will eventually lead to a core-collapse SN (N_{CCSN}) event can also be determined via the IMF as ¹,

$$N_{CCSN} = \int_{m_l}^{m_u} \zeta(m)dm, \quad (\text{B.4})$$

where m_l and m_u are the minimal ($\gtrsim 8M_{\odot}$, Section 4.1.2) and maximal mass (typically $m_u = m_{max}$) required to trigger a core-collapse SN. Therefore the fraction

$$\Upsilon \equiv \frac{N_{CCSN}}{M_{total}} \quad [M_{\odot}^{-1}], \quad (\text{B.5})$$

reflects the total number of stars at formation time which will eventually end up as core-collapse SN per total initial mass. Multiplying Υ with the inferred star-formation rate (Ψ_{SFR} [M_{\odot}/yr]) of the considered starburst region then corresponds to the number of stars at formation time that will eventually end up as core-collapse SN events.

Assuming that the stellar population present is short-lived w.r.t the starburst time scale, that the corresponding star-formation rate has been constant, and that the starburst episode has been going on for longer than the lifetime of the longest-lived massive star, it is (approximately) justified to use

$$\mathcal{R}_{SN} = \Upsilon \cdot \Psi_{SFR} \quad [\text{yr}^{-1}], \quad (\text{B.6})$$

as an estimate of the SN rate today. However, it must be noted that in case of LIRGs the assumption of a constant star-formation rate should be treated carefully, and the age of the starburst can also be comparable to the lifetimes of the massive stars exploding as core-collapse SN. Therefore, in order to have a more accurate estimate when using the IMF approach, one should consider the star-formation history of the studied source.

The approach outlined above is only an estimate for the rate of core-collapse type SN. However, one might argue that there is also a possible contribution from thermonuclear type SN. Nevertheless, as argued in Section 4.1.2, the enhancement of the SN rate in starburst regions is dominantly due to core-collapse SN because of the significantly longer lifetimes of low-mass stars.

Star-formation rate in U/LIRGs From Equation B.6 it is concluded that once an appropriate IMF is chosen, only Ψ_{SFR} must be determined from electromagnetic observations to find \mathcal{R}_{SN} . Newly formed stars actively emit ionizing UV photons and therefore the integrated UV spectrum in a galaxy is dominated by young stars. This indicates that the UV luminosity is a sensitive probe for recent SF. However, in compact starburst regions of U/LIRGs the large amounts of dust and gas lead to severe attenuation of UV photons, which rules them out as good tracer for recent star formation. Nevertheless, these attenuating interactions lead to heating of gas and dust which subsequently results in thermal emission. Therefore the IR luminosity is a more appropriate tracer for

¹ N_{CCSN} is not to be confused with the normalisation constant of the injection rate.

star formation in U/LIRGs. In [87] the relation between IR luminosity $L_{IR} \equiv L_{[8-1000\mu m]}$ and the recent star-formation rate is given as

$$\left(\frac{\text{SFR}_{IR}}{M_{\odot}\text{yr}^{-1}}\right) = 3.88 \times 10^{-44} \left(\frac{L_{IR}}{\text{erg s}^{-1}}\right). \quad (\text{B.7})$$

However, a non-negligible fraction of the far-IR continuum could be due to heating of an older stellar population. Therefore one could opt to relate the current star-formation rate to warmer dust emission. As such [87] also includes a relation between the monochromatic 24 μm emission and the star-formation rate.

In Section 3.2 it was already discussed that the radio continuum of U/LIRGs is composed of non-thermal synchrotron emission from electron movement in magnetic fields and thermal free-free emission from H II regions, both related to massive star formation. Therefore [87] also provides an expression to determine the recent star-formation rate from the total radio continuum at a given frequency as

$$\left(\frac{\text{SFR}_{\nu}}{M_{\odot}\text{yr}^{-1}}\right) = 10^{-27} \left[2.18 \left(\frac{T_e}{10^4\text{K}}\right)^{0.45} \left(\frac{\nu}{\text{GHz}}\right)^{-0.1} + 15.1 \left(\frac{\nu}{\text{GHz}}\right)^{\alpha_{NT}} \right]^{-1} \left(\frac{L_{\nu}}{\text{ergs}^{-1}}\right), \quad (\text{B.8})$$

where T_e is the electron temperature and α_{NT} the non-thermal spectral index. In conclusion, if an IMF is selected and the appropriate IR or radio luminosity has been acquired, one can estimate \mathcal{R}_{SN} .

Bibliography

- [1] A. Aab et al. “The Pierre Auger Cosmic Ray Observatory”. In: *Nucl. Instrum. Meth. A* 798 (2015). DOI: 10.1016/j.nima.2015.06.058. arXiv: 1502.01323 [astro-ph.IM].
- [2] B. S. Acharya et al. *Science with the Cherenkov Telescope Array*. WSP, Nov. 2018. ISBN: 978-981-327-008-4. DOI: 10.1142/10986. arXiv: 1709.07997 [astro-ph.IM].
- [3] J. Aleksić et al. “The major upgrade of the MAGIC telescopes, Part II: A performance study using observations of the Crab Nebula”. In: *Astroparticle Physics* 72 (Jan. 2016), pp. 76–94. DOI: 10.1016/j.astropartphys.2015.02.005. arXiv: 1409.5594 [astro-ph.IM].
- [4] M. D. Naurois. “The H.E.S.S. experiment : current status and future prospects”. In: *PoS ICRC 2019* (2020), p. 656. DOI: 10.22323/1.358.0656.
- [5] S. Bravo. *Neutrinos and gamma rays, a partnership to explore the extreme universe*. 2016. URL: <https://icecube.wisc.edu/news/research/2016/10/neutrinos-and-gamma-rays-partnership-to-explore-extreme-universe/>.
- [6] M. G. Aartsen et al. “Evidence for High-Energy Extraterrestrial Neutrinos at the IceCube Detector”. In: *Science* 342 (2013), p. 1242856. DOI: 10.1126/science.1242856. arXiv: 1311.5238 [astro-ph.HE].
- [7] L. Mohrmann. “Characterizing cosmic neutrino sources”. PhD thesis. Humboldt-Universität zu Berlin, Mathematisch-Naturwissenschaftliche Fakultät, 2015. DOI: <http://dx.doi.org/10.18452/17377>.
- [8] M. G. Aartsen et al. “The contribution of Fermi-2LAC blazars to the diffuse TeV-PeV neutrino flux”. In: *ApJ* 835.1 (2017), p. 45. DOI: 10.3847/1538-4357/835/1/45. arXiv: 1611.03874 [astro-ph.HE].
- [9] K. Bechtol et al. “Evidence against star-forming galaxies as the dominant source of IceCube neutrinos”. In: *ApJ* 836.1 (2017), p. 47. DOI: 10.3847/1538-4357/836/1/47. arXiv: 1511.00688 [astro-ph.HE].
- [10] G. Maggi et al. “Obscured flat spectrum radio active galactic nuclei as sources of high-energy neutrinos”. In: *Phys. Rev. D* 94.10 (2016), p. 103007. DOI: 10.1103/PhysRevD.94.103007. arXiv: 1608.00028 [astro-ph.HE].
- [11] G. Maggi, K. D. de Vries, and N. van Eijndhoven. “Investigation of Obscured Flat Spectrum Radio AGN with the IceCube Neutrino Observatory”. In: *PoS ICRC2017* (2018), p. 1000. DOI: 10.22323/1.301.1000.
- [12] Matthias Vereecken and Krijn D. de Vries. “Obscured pp -channel neutrino sources”. arXiv: 2004.03435 [astro-ph.HE]. Apr. 2020.
- [13] Y. Merckx. *ThesisCode*. <https://github.com/YarnoMerckx/ThesisCode.git>. 2021.

BIBLIOGRAPHY

- [14] A. A. Watson. “High-energy cosmic rays and the Greisen–Zatsepin–Kuz’min effect”. In: *Rept. Prog. Phys.* 77 (2014), p. 036901. DOI: 10.1088/0034-4885/77/3/036901. arXiv: 1310.0325 [astro-ph.HE].
- [15] J. Alvarez-Muñiz et al. “The Giant Radio Array for Neutrino Detection (GRAND): Science and Design”. In: *Sci. China Phys. Mech. Astron.* 63.1 (2020), p. 219501. DOI: 10.1007/s11433-018-9385-7. arXiv: 1810.09994 [astro-ph.HE].
- [16] Ara Collaboration et al. “Design and initial performance of the Askaryan Radio Array prototype EeV neutrino detector at the South Pole”. In: *Astroparticle Physics* 35.7 (Feb. 2012), pp. 457–477. DOI: 10.1016/j.astropartphys.2011.11.010. arXiv: 1105.2854 [astro-ph.IM].
- [17] Raymond Davis Jr., Don S. Harmer, and Kenneth C. Hoffman. “Search for neutrinos from the sun”. In: *Phys. Rev. Lett.* 20 (1968), pp. 1205–1209. DOI: 10.1103/PhysRevLett.20.1205.
- [18] K. Hirata et al. “Observation of a neutrino burst from the supernova SN1987A”. In: *Phys. Rev. Lett.* 58 (14 Apr. 1987), pp. 1490–1493. DOI: 10.1103/PhysRevLett.58.1490. URL: <https://link.aps.org/doi/10.1103/PhysRevLett.58.1490>.
- [19] R. M. Bionta et al. “Observation of a neutrino burst in coincidence with supernova 1987A in the Large Magellanic Cloud”. In: *Phys. Rev. Lett.* 58 (14 Apr. 1987), pp. 1494–1496. DOI: 10.1103/PhysRevLett.58.1494. URL: <https://link.aps.org/doi/10.1103/PhysRevLett.58.1494>.
- [20] U. F. Katz and Ch. Spiering. “High-Energy Neutrino Astrophysics: Status and Perspectives”. In: *Prog. Part. Nucl. Phys.* 67 (2012), pp. 651–704. DOI: 10.1016/j.ppnp.2011.12.001. arXiv: 1111.0507 [astro-ph.HE].
- [21] R. Abbasi et al. “IceTop: The surface component of IceCube. The IceCube Collaboration”. In: *Nuclear Instruments and Methods in Physics Research A* 700 (Feb. 2013), pp. 188–220. DOI: 10.1016/j.nima.2012.10.067. arXiv: 1207.6326 [astro-ph.IM].
- [22] M. G. Aartsen et al. “The IceCube Neutrino Observatory - Contributions to ICRC 2017 Part II: Properties of the Atmospheric and Astrophysical Neutrino Flux”. In: (Oct. 2017). arXiv: 1710.01191 [astro-ph.HE].
- [23] M. G. Aartsen et al. “All-sky Search for Time-integrated Neutrino Emission from Astrophysical Sources with 7 yr of IceCube Data”. In: *ApJ* 835.2 (2017), p. 151. DOI: 10.3847/1538-4357/835/2/151. arXiv: 1609.04981 [astro-ph.HE].
- [24] M. Tanabashi et al. “Review of Particle Physics”. In: *Phys. Rev. D* 98.3 (2018), p. 030001. DOI: 10.1103/PhysRevD.98.030001.
- [25] R. Abbasi et al. “The IceCube high-energy starting event sample: Description and flux characterization with 7.5 years of data”. In: (Nov. 2020). arXiv: 2011.03545 [astro-ph.HE].
- [26] J. Stettner. “Measurement of the Diffuse Astrophysical Muon-Neutrino Spectrum with Ten Years of IceCube Data”. In: *PoS ICRC2019* (2020), p. 1017. DOI: 10.22323/1.358.1017. arXiv: 1908.09551 [astro-ph.HE].
- [27] C. Kopper. *Analysis of the High-Energy Starting Events in IceCube*. 2013. URL: https://indico.cern.ch/event/221841/contributions/1525814/attachments/362223/504242/Kopper_-_TeVPA_HESE_technical.pdf.
- [28] M. G. Aartsen et al. “Time-Integrated Neutrino Source Searches with 10 Years of IceCube Data”. In: *Phys. Rev. Lett.* 124.5 (2020), p. 051103. DOI: 10.1103/PhysRevLett.124.051103. arXiv: 1910.08488 [astro-ph.HE].

BIBLIOGRAPHY

- [29] R. Abbasi et al. “IceCube Data for Neutrino Point-Source Searches Years 2008-2018”. In: (Jan. 2021). DOI: 10.21234/CPKQ-K003. arXiv: 2101.09836 [astro-ph.HE].
- [30] S. Ansoldi et al. “The blazar TXS 0506+056 associated with a high-energy neutrino: insights into extragalactic jets and cosmic ray acceleration”. In: *ApJ Lett.* 863 (2018), p. L10. DOI: 10.3847/2041-8213/aad083. arXiv: 1807.04300 [astro-ph.HE].
- [31] M. G. Aartsen et al. “Multimessenger observations of a flaring blazar coincident with high-energy neutrino IceCube-170922A”. In: *Science* 361.6398 (2018), eaat1378. DOI: 10.1126/science.aat1378. arXiv: 1807.08816 [astro-ph.HE].
- [32] T. C. Licquia and J. A. Newman. “Improved Estimates of the Milky Way’s Stellar Mass and Star Formation Rate from Hierarchical Bayesian Meta-Analysis”. In: *ApJ* 806.1, 96 (June 2015), p. 96. DOI: 10.1088/0004-637X/806/1/96. arXiv: 1407.1078 [astro-ph.GA].
- [33] S. Sakai and B. F. Madore. “Detection of the Red Giant Branch Stars in M82 Using the Hubble Space Telescope”. In: *ApJ* 526.2 (Dec. 1999), pp. 599–606. DOI: 10.1086/308032. URL: <https://doi.org/10.1086/308032>.
- [34] R. Rekola et al. “Distance to NGC 253 based on the planetary nebula luminosity function”. In: *Mon. Not. Roy. Astron. Soc.* 361.1 (July 2005), pp. 330–336. ISSN: 0035-8711. DOI: 10.1111/j.1365-2966.2005.09166.x. eprint: <https://academic.oup.com/mnras/article-pdf/361/1/330/18658607/361-1-330.pdf>. URL: <https://doi.org/10.1111/j.1365-2966.2005.09166.x>.
- [35] T. J. Davidge. “Shaken, Not Stirred: The Disrupted Disk of the Starburst Galaxy NGC 253”. In: *ApJ* 725.1 (Dec. 2010), pp. 1342–1365. DOI: 10.1088/0004-637X/725/1/1342. arXiv: 1011.3006 [astro-ph.CO].
- [36] J. Kelly. *Hubble Views Starbursting Galaxy SBS 1415+437*. June 2015. URL: <https://scitechdaily.com/hubble-views-starbursting-galaxy-sbs-1415437/>
- [37] information@eso.org. *A cosmic couple*. 2015. URL: <https://esahubble.org/images/potw1533a/>.
- [38] P. Correa, K. D. de Vries, and N. van Eijndhoven. “Investigation of Ultra-Luminous Infrared Galaxies as Obscured High-Energy Neutrino Source Candidates”. In: *PoS ICRC2019* (2020), p. 860. DOI: 10.22323/1.358.0860. arXiv: 1908.05137 [astro-ph.HE].
- [39] K. Iwasawa et al. “C-GOALS: Chandra observations of a complete sample of luminous infrared galaxies from the IRAS Revised Bright Galaxy Survey”. In: *A&A* 529, A106 (May 2011), A106. DOI: 10.1051/0004-6361/201015264. arXiv: 1103.2755 [astro-ph.CO].
- [40] A. O. Petric et al. “Mid-Infrared Spectral Diagnostics of Luminous Infrared Galaxies”. In: *ApJ* 730.1, 28 (Mar. 2011), p. 28. DOI: 10.1088/0004-637X/730/1/28. arXiv: 1012.1891 [astro-ph.GA].
- [41] C. Ricci et al. “Growing supermassive black holes in the late stages of galaxy mergers are heavily obscured”. In: *Mon. Not. Roy. Astron. Soc.* 468.2 (June 2017), pp. 1273–1299. DOI: 10.1093/mnras/stx173. arXiv: 1701.04825 [astro-ph.HE].
- [42] L. Armus et al. “GOALS: The Great Observatories All-Sky LIRG Survey”. In: *Astropart. Phys* 121.880 (June 2009), p. 559. DOI: 10.1086/600092. arXiv: 0904.4498 [astro-ph.CO].
- [43] GOALS EAST. *LIRGs and GOALS*. 2019. URL: <https://sites.google.com/site/goalseast/>.

BIBLIOGRAPHY

- [44] L. Barcos-Muñoz et al. “A 33 GHz Survey of Local Major Mergers: Estimating the Sizes of the Energetically Dominant Regions from High-resolution Measurements of the Radio Continuum”. In: *ApJ* 843.2, 117 (July 2017), p. 117. DOI: 10.3847/1538-4357/aa789a. arXiv: 1705.10801 [astro-ph.GA].
- [45] T. Diaz-Santos et al. “The Spatial Extent of (U)LIRGs in the Mid-infrared. I. The Continuum Emission”. In: *ApJ* 723.2 (Nov. 2010), pp. 993–1005. DOI: 10.1088/0004-637X/723/2/993. arXiv: 1009.0038 [astro-ph.CO].
- [46] A. D. Bolatto, M. Wolfire, and Adam K. Leroy. “The CO-to-H₂ Conversion Factor”. In: *Annu. Rev. Astron. Astrophys.* 51.1 (Aug. 2013), pp. 207–268. DOI: 10.1146/annurev-astro-082812-140944. arXiv: 1301.3498 [astro-ph.GA].
- [47] R. Herrero-Illana et al. “Molecular gas and dust properties of galaxies from the Great Observatories All-sky LIRG Survey”. In: *A&A* 628, A71 (Aug. 2019), A71. DOI: 10.1051/0004-6361/201834088. arXiv: 1907.03854 [astro-ph.GA].
- [48] Padelis P. Papadopoulos. “HCN versus HCO⁺ as dense molecular gas mass tracer in Luminous Infrared Galaxies”. In: *ApJ* 656 (2007), pp. 792–797. DOI: 10.1086/510186. arXiv: astro-ph/0610477.
- [49] N. Scoville et al. “ISM Masses and the Star formation Law at Z = 1 to 6: ALMA Observations of Dust Continuum in 145 Galaxies in the COSMOS Survey Field”. In: *Asytophys. J.* 820.2, 83 (Apr. 2016), p. 83. DOI: 10.3847/0004-637X/820/2/83. arXiv: 1511.05149 [astro-ph.GA].
- [50] K. L. Larson et al. “Morphology and Molecular Gas Fractions of Local Luminous Infrared Galaxies as a Function of Infrared Luminosity and Merger Stage”. In: *ApJ* 825.2 (2016), p. 128. DOI: 10.3847/0004-637X/825/2/128. arXiv: 1605.05417 [astro-ph.GA].
- [51] G. Helou et al. “The NASA/IPAC Extragalactic Database”. In: *Databases & On-line Data in Astronomy*. Ed. by Miguel A. Albrecht and Daniel Egret. Dordrecht: Springer Netherlands, 1991, pp. 89–106. ISBN: 978-94-011-3250-3. DOI: 10.1007/978-94-011-3250-3_10. URL: https://doi.org/10.1007/978-94-011-3250-3_10.
- [52] E. Varenus et al. “Subarcsecond international LOFAR radio images of Arp 220 at 150 MHz. A kpc-scale star forming disk surrounding nuclei with shocked outflows”. In: *A&A* 593, A86 (Sept. 2016), A86. DOI: 10.1051/0004-6361/201628702. arXiv: 1607.02761 [astro-ph.GA].
- [53] C. J. Lonsdale et al. “VLBI Images of 49 Radio Supernovae in Arp 220”. In: *The Astrophysical Journal* 647.1 (Aug. 2006), pp. 185–193. DOI: 10.1086/505193. URL: <https://doi.org/10.1086/505193>.
- [54] K. Rozwadowska, F. Vissani, and E. Cappellaro. “On the rate of core collapse supernovae in the milky way”. In: *New Astron.* 83 (2021), p. 101498. DOI: 10.1016/j.newast.2020.101498. arXiv: 2009.03438 [astro-ph.HE].
- [55] Nick Scoville et al. “ALMA Resolves the Nuclear Disks of Arp 220”. In: *The Astrophysical Journal* 836.1 (Feb. 2017), p. 66. DOI: 10.3847/1538-4357/836/1/66. URL: <https://doi.org/10.3847/1538-4357/836/1/66>.
- [56] M. Bondi et al. “The nuclear starburst in Arp 299-A: from the 5.0 GHz VLBI radio light-curves to its core-collapse supernova rate”. In: *A&A* 539, A134 (Mar. 2012), A134. DOI: 10.1051/0004-6361/201118446. arXiv: 1201.3220 [astro-ph.CO].

BIBLIOGRAPHY

- [57] M. Pérez-Torres et al. “Star formation and nuclear activity in luminous infrared galaxies: an infrared through radio review”. In: *A&AR* 29.1, 2 (Dec. 2021), p. 2. DOI: 10.1007/s00159-020-00128-x. arXiv: 2010.05072 [astro-ph.GA].
- [58] Chandra X-ray Observatory. *Arp 299: Galactic Goulash*. 2017. URL: <https://chandra.harvard.edu/photo/2017/arp299/>.
- [59] N. Ramirez-Olivencia et al. “Sub-arcsecond imaging of Arp 299-A at 150 MHz with LOFAR: Evidence for a starburst-driven outflow”. In: *A&A* 610, L18 (Mar. 2018), p. L18. DOI: 10.1051/0004-6361/201732543. arXiv: 1802.03226 [astro-ph.GA].
- [60] R. Stein et al. “A tidal disruption event coincident with a high-energy neutrino”. In: *Nature Astronomy* (2021). DOI: 10.1038/s41550-020-01295-8.
- [61] E. Peretti et al. “Cosmic ray transport and radiative processes in nuclei of starburst galaxies”. In: *Mon. Not. Roy. Astron. Soc.* 487.1 (2019), pp. 168–180. DOI: 10.1093/mnras/stz1161. arXiv: 1812.01996 [astro-ph.HE].
- [62] J-H. Ha, D. Ryu, and H. Kang. “Modeling of Cosmic-Ray Production and Transport and Estimation of Gamma-Ray and Neutrino Emissions in Starburst Galaxies”. In: *ApJ* 907.1 (2021), p. 26. DOI: 10.3847/1538-4357/abd247. arXiv: 2008.06650 [astro-ph.HE].
- [63] A. Ambrosone et al. “Starburst galaxies strike back: a multi-messenger analysis with Fermi-LAT and IceCube data”. In: *Mon. Not. Roy. Astron. Soc.* 503.3 (2021), p. 4032. DOI: 10.1093/mnras/stab659. arXiv: 2011.02483 [astro-ph.HE].
- [64] D. Maoz. *Astrophysics in a Nutshell: Second Edition (In a Nutshell, 16)*. 2nd ed. Princeton University Press, 2016.
- [65] H. A. Bethe and J. R. Wilson. “Revival of a stalled supernova shock by neutrino heating”. In: *ApJ* 295 (Aug. 1985), pp. 14–23. DOI: 10.1086/163343.
- [66] Malcolm S. Longair. *High Energy Astrophysics*. 2011.
- [67] European Space Agency. *Stellar jets HH 47, HH 34 and HH 2*. 2011. URL: <https://esahubble.org/images/heic1113a/>.
- [68] L. Brayeur. “Search for High-Energy Neutrinos Associated with Long Gamma Ray Bursts using the IceCube Detector”. PhD thesis. Vrije Universiteit Brussel, 2015. URL: <https://iihe.ac.be/sites/default/files/thesis-lionel-brayeur-icecube-phd-2015pdf/thesis-lionel-brayeur-icecube-phd-2015.pdf>.
- [69] P. Blasi and E. Amato. “Diffusive propagation of cosmic rays from supernova remnants in the Galaxy. I: spectrum and chemical composition”. In: *JCAP* 2012.1, 010 (Jan. 2012), p. 010. DOI: 10.1088/1475-7516/2012/01/010. arXiv: 1105.4521 [astro-ph.HE].
- [70] Jeongbhin Seo, Hyesung Kang, and Dongsu Ryu. “The Contribution of Stellar Winds to Cosmic Ray Production”. In: *J. Korean Astron. Soc.* 51.2 (2018), pp. 37–48. DOI: 10.5303/JKAS.2018.51.2.37. arXiv: 1804.07486 [astro-ph.HE].
- [71] M. Lemoine, K. Kotera, and J. Pétri. “On ultra-high energy cosmic ray acceleration at the termination shock of young pulsar winds”. In: *JCAP* 07 (2015), p. 016. DOI: 10.1088/1475-7516/2015/07/016. arXiv: 1409.0159 [astro-ph.HE].
- [72] D. Caprioli. “Cosmic-ray Acceleration and Propagation”. In: *PoS ICRC2015* (2016), p. 008. DOI: 10.22323/1.236.0008. arXiv: 1510.07042 [astro-ph.HE].
- [73] T. A. Thompson et al. “Magnetic fields in starburst galaxies and the origin of the fir-radio correlation”. In: *ApJ* 645 (2006), pp. 186–198. DOI: 10.1086/504035. arXiv: astro-ph/0601626.

BIBLIOGRAPHY

- [74] Hao-Ning He et al. “Diffuse PeV neutrino emission from ultraluminous infrared galaxies”. In: *Phys. Rev. D* 87.6 (2013), p. 063011. DOI: 10.1103/PhysRevD.87.063011. arXiv: 1303.1253 [astro-ph.HE].
- [75] Mitchell C. Begelman, Bronislaw Rudak, and Marek Sikora. “Consequences of Relativistic Proton Injection in Active Galactic Nuclei”. In: *ApJ* 362 (Oct. 1990), p. 38. DOI: 10.1086/169241.
- [76] S. R. Kelner, F. A. Aharonian, and V. V. Bugayov. “Energy spectra of gamma-rays, electrons and neutrinos produced at proton-proton interactions in the very high energy regime”. In: *Phys. Rev. D* 74 (2006). [Erratum: *Phys.Rev.D* 79, 039901 (2009)], p. 034018. DOI: 10.1103/PhysRevD.74.034018. arXiv: astro-ph/0606058.
- [77] R. S. Fletcher et al. “sibyll: An event generator for simulation of high energy cosmic ray cascades”. In: *Phys. Rev. D* 50 (9 Nov. 1994), pp. 5710–5731. DOI: 10.1103/PhysRevD.50.5710. URL: <https://link.aps.org/doi/10.1103/PhysRevD.50.5710>.
- [78] E. Peretti et al. “Particle acceleration and multi-messenger emission from starburst-driven galactic winds”. arXiv: 2104.10978 [astro-ph.HE]. Apr. 2021.
- [79] D. Zhang. “A Review of the Theory of Galactic Winds Driven by Stellar Feedback”. In: *Galaxies* 6.4 (Nov. 2018), p. 114. DOI: 10.3390/galaxies6040114. arXiv: 1811.00558 [astro-ph.GA].
- [80] information@eso.org. *The magnificent starburst galaxy Messier 82*. 2006. URL: %5Curl%7Bhttps://esahubble.org/images/heic0604a/%7D.
- [81] Daan Frenkel and Berend Smit. *Understanding Molecular Simulation: From Algorithms to Applications*. 1st. USA: Academic Press, Inc., 1996. ISBN: 0122673700.
- [82] M. J. F. Rosenberg et al. “Molecular gas heating in Arp 299”. In: *A&A* 568, A90 (Aug. 2014), A90. DOI: 10.1051/0004-6361/201423707. arXiv: 1407.2055 [astro-ph.GA].
- [83] Loreto Barcos-Muñoz et al. “Fast, Collimated Outflow in the Western Nucleus of Arp 220”. In: *ApJ* 853.2, L28 (Feb. 2018), p. L28. DOI: 10.3847/2041-8213/aaa28d. arXiv: 1712.06381 [astro-ph.GA].
- [84] H. Athar, M. Jezabek, and O. Yasuda. “Effects of neutrino mixing on high-energy cosmic neutrino flux”. In: *Phys. Rev. D* 62 (2000), p. 103007. DOI: 10.1103/PhysRevD.62.103007. arXiv: hep-ph/0005104.
- [85] Edwin E. Salpeter. “The Luminosity Function and Stellar Evolution.” In: *ApJ* 121 (Jan. 1955), p. 161. DOI: 10.1086/145971.
- [86] Pavel Kroupa. “On the variation of the initial mass function”. In: *Mon. Not. Roy. Astron. Soc.* 322 (2001), p. 231. DOI: 10.1046/j.1365-8711.2001.04022.x. arXiv: astro-ph/0009005.
- [87] E. J. Murphy et al. “Calibrating Extinction-free Star Formation Rate Diagnostics with 33 GHz Free-free Emission in NGC 6946”. In: *ApJ* 737.2, 67 (Aug. 2011), p. 67. DOI: 10.1088/0004-637X/737/2/67. arXiv: 1105.4877 [astro-ph.CO].